

CHRISTOPH HEIL

# Electronic Properties and Susceptibilities of Iron-Based Superconductors

## DOCTORAL THESIS

For obtaining the academic degree of  
Doktor der technischen Wissenschaften

Doctoral Programm of Technical Sciences  
Technical Physics



Graz University of Technology

Supervisor:

Univ.-Prof. Dipl.-Phys. Dr.rer.nat. Wolfgang von der Linden

Co-Supervisor:

Ass.Prof. Dr. Lilia Boeri

Institute of Theoretical and Computational Physics

Graz, October 2014



*“If you don’t know anything about computers, just remember that they are machines  
that do exactly what you tell them but often surprise you in the result.”*

—Richard Dawkins



# Abstract

The scope of this thesis was to investigate the electronic properties of the recently discovered iron-based superconductors. This new kind of high-temperature superconductors exhibits a rich low energy band structure and superconductivity is observed in close proximity to a magnetically ordered phase. It was our aim to study the electronic behavior and electronic susceptibilities to shed light on the evolution of the critical superconducting temperatures with doping or pressure.

We developed a new implementation of the tetrahedron method that allows us to calculate bare susceptibilities from *first-principles* without approximations in an efficient way and utilized this program to obtain bare susceptibilities for a large number of different iron-based superconductors. Of all the calculations we performed, we will present two prototypical examples in this manuscript. The first is LaFeAsO, where superconductivity can be achieved by electron doping. We determined the bare susceptibilities with different concentrations of doping and compared our results with the experimentally observed behavior of the critical superconducting temperature. The second case is that of FeSe, where the superconducting temperature increases drastically when pressure is applied. Here again, we computed susceptibilities for different hydrostatic and non-hydrostatic pressure and confronted our results with measurements on  $T_c$ . While the trends in the critical temperature could not be unambiguously linked to the susceptibilities, we could demonstrate that susceptibilities, even in the non-interacting case, are quantities with relevant physical information in the whole Brillouin zone and for any continuative theory that considers interactions, the precise knowledge of these bare quantities is therefore essential.

We also present calculations on the newly synthesized iron-based superconductor  $\text{LiFeO}_2\text{Fe}_2\text{Se}_2$ . This compound features two non-equivalent iron atoms and has a much richer low-energy band structure than the usual iron-based superconductor. To investigate the electronic and magnetic properties of this compound, we employed not only methods based on density functional theory, but also included correlations in the framework of dynamical mean field theory. We demonstrated that this compound displays two different realizations of correlation effects due to Hund's coupling, caused by the different valences of the two non-equivalent iron atoms and that due to the inclusion of correlations, the usual iron-based superconductor Fermi surface is restored.

We are confident that important developments in the understanding of the physics of iron-based superconductors have been accomplished in the course of this PhD project. Additionally, we introduced a state-of-the-art full potential *ab initio* method to accurately and efficiently calculate bare susceptibilities, which are important quantities for many different physical properties.



# Kurzfassung

Das Ziel dieses Doktoratsprojektes lag in der Erforschung der elektronischen Eigenschaften der erst kürzlich entdeckten, eisenbasierten Supraleitern. Diese neuartige Klasse von Supraleitern besitzt eine komplexe, niederenergetische Bandstruktur und die Supraleitung findet in direkter Nähe zu einer magnetisch geordneten Phase statt. Theorien, die von schwacher Wechselwirkung ausgehen, bringen die Spinsuszeptibilität mit dem Paarungsmechanismus der Supraleitung in Verbindung. Wir haben es uns zur Aufgabe gemacht herauszufinden, ob das Verhalten der kritischen Supraleitungstemperatur als Funktion der Dotierung oder der Druckausübung bereits in der nicht-wechselwirkenden Suszeptibilität sichtbar ist.

Dazu haben wir eine neue Variante der Tetraedermethode entwickelt, die es uns erlaubt, nicht-wechselwirkende Suszeptibilitäten ausgehend von *ab initio* Rechnungen akkurat zu bestimmen. Derartige Rechnungen wurden für eine Vielzahl verschiedener eisenbasierter Supraleiter durchgeführt, von denen zwei prototypische Beispiele in diesem Manuskript präsentiert werden. Zum einen zeigen und diskutieren wir nicht-wechselwirkende Suszeptibilitäten für LaFeAsO mit verschiedenen Dotierungskonzentrationen und zum anderen für FeSe unter verschiedenen Drücken, und stellen unsere Ergebnisse denen von Experimenten gegenüber. Obwohl das Verhalten der kritischen Temperatur nicht eindeutig in den nicht-wechselwirkenden Suszeptibilitäten erkennbar ist, konnten wir zeigen, dass die Suszeptibilitäten selbst im nicht-wechselwirkenden Fall in der ganzen Brillouin-Zone wichtige Beiträge besitzen. Für jede weiterführende Theorie ist ihre genaue Kenntnis daher von großer Bedeutung.

In den späteren Kapiteln präsentieren wir eine umfassende Untersuchung der elektronischen Eigenschaften des Supraleiters  $\text{LiFeO}_2\text{Fe}_2\text{Se}_2$ . Im Zuge dieser Arbeit verwendeten wir eine Vielzahl von Methoden, die nicht nur auf die Dichtefunktionalstheorie beschränkt sind, sondern auch die Dynamische Molekularfeld-Theorie miteinbeziehen. Abgesehen davon, dass dieses Material ein sehr interessantes niederenergetisches Verhalten im Rahmen der Dichtefunktionalstheorie zeigt, konnten wir zeigen, dass es einen seltenen Fall darstellt, indem verschiedene Effekte der Hund'schen Kopplung auf einmal auftreten. Dies ist begründet in der Tatsache, dass dieser Supraleiter zwei nicht-äquivalente Eisenatome beinhaltet, die unterschiedliche Valenzen aufweisen.

Wir sind davon überzeugt, dass mit dieser Arbeit ein wichtiger Beitrag zum besseren Verständnis der Supraleitung in eisenbasierten Materialien geliefert wurde. Darüber hinaus stellen wir ein sehr leistungsfähiges Programm zur Berechnung nicht-wechselwirkender Suszeptibilitäten vor, die wichtige Größen in Bezug auf viele physikalische Eigenschaften sind.



# Contents

<b>Abstract</b>	<b>iii</b>
<b>Kurzfassung</b>	<b>v</b>
<b>1. Introduction</b>	<b>1</b>
<b>I. Background</b>	<b>9</b>
<b>2. Theoretical Background</b>	<b>11</b>
2.1. The Response Functions $\chi_{\pm}$ and $\chi_c$	13
2.2. The <i>Bare</i> Susceptibility $\chi^0$	15
2.3. The Static <i>Bare</i> Susceptibility	20
2.3.1. Inter- and Intraband Contributions and the Limit $ \mathbf{q}  \rightarrow 0$	21
2.4. Going Beyond the Bare Susceptibility	22
2.4.1. Random Phase Approximation	22
2.4.2. Local Field Effects	24
2.4.3. Including Interactions in the Case of Iron-Based Superconductors	25
<b>3. Numerical Implementation</b>	<b>29</b>
3.1. Introduction	29
3.2. Different Conventions for $\chi^0$	30
3.3. Implementation of the Tetrahedron Method	31
3.3.1. Comparison of the MVC code and our new implementation	35
3.3.2. Calculation of the dynamic susceptibility	38
<b>II. Results</b>	<b>41</b>
<b>4. Accurate bare susceptibilities from full-potential ab initio calculations</b>	<b>43</b>
4.1. Introduction	43
4.2. Method	45
4.3. Static Bare Susceptibility	48
4.4. Dynamic Bare Susceptibility	56
4.5. Conclusions	58
<b>5. LaFeAsO and the Effects of Doping</b>	<b>61</b>
5.1. Introduction	61

5.2. Static Bare Susceptibility . . . . .	66
5.3. Dynamic Bare Susceptibility . . . . .	71
5.4. Conclusions . . . . .	73
<b>6. Static susceptibility and Fermi surface nesting in FeSe under pressure from first-principle calculations</b>	<b>75</b>
6.1. Introduction . . . . .	75
6.2. Method . . . . .	76
6.3. Results . . . . .	77
6.4. Discussions and Conclusions . . . . .	81
<b>7. Effect of the iron valence in the two types of layers in <math>\text{LiFeO}_2\text{Fe}_2\text{Se}_2</math></b>	<b>85</b>
7.1. Introduction . . . . .	85
7.2. Computational Details . . . . .	86
7.3. Electronic Structure . . . . .	88
7.4. Correlated electronic structure . . . . .	95
7.5. Conclusions . . . . .	99
<b>8. Conclusion</b>	<b>101</b>
<b>A. Integration Formulas</b>	<b>105</b>
<b>Acknowledgements</b>	<b>109</b>
<b>List of Publications and Preprints</b>	<b>127</b>
<b>List of Abbreviations and Symbols</b>	<b>129</b>

# Chapter 1.

## Introduction

In the course of this thesis we investigated electronic properties of iron-pnictides and iron-chalcogenides [1,2] to shed light on the underlying physics of their unconventional superconductivity.

This new class of high-temperature (high- $T_c$ ) superconductors has caught a lot of attention in the scientific community. The research interest is founded in the fact that magnetism and superconductivity (SC) have long been thought of as being mutually exclusive, while in iron-based superconductors (FeSCs) an iron atom is present in the active layer. Additionally, in contrast to cuprates, a direct doping of the active layer can be achieved. Since the discovery of the first FeSC in 2006 [3], a plethora of new compounds have been synthesized and studied extensively. For many materials among the FeSCs, a single-stripe antiferromagnetic (AFM) order was found experimentally to be the ground state for the parent compounds [4–6]. When the compounds are doped or pressure is applied, this AFM ordered phase vanishes to the benefit of a superconducting one [7]. A schematical depiction of a prototypical FeSC phase diagram<sup>1</sup> is presented in Fig. 1.1. At high temperatures, the materials are in a paramagnetic phase (indicated by PM) and upon cooling develop a long range AFM order or superconductivity, depending on the doping concentration. In most of these materials, also a structural transition from the tetragonal phase to phases of lower symmetry takes place. We will in this work, however, not discuss the implications of the structural transitions and refer the reader to Refs. [9–15] and references therein.

The occurrence of the superconducting phase was attributed to the very special low-energy electronic structure of FeSCs. Theoretical studies showed that the Fermi surface of almost all of these compounds has at least two electron and two hole cylinders of quasi two-dimensional shape. The two hole cylinders are centered at the Brillouin zone (BZ) center, while the electron pockets located at the corners of the BZ (see for example Ref. [16] or Sec. 6 of this work). Due to the very similar radii, the pockets can be aligned with the nesting vector  $\mathbf{q}_N = (\frac{\pi}{a}, \frac{\pi}{a})$ , and give rise to a single-stripe antiferromagnetic ordering in an itinerant model of magnetism [17–19]. Although *density functional theory* (DFT) methods can most of the time reproduce the observed Fermi surfaces, they fail with predicting the magnitude of the magnetic moments [20, 21]. This is due to the fact that DFT calculations are mean-field by nature and therefore do not account for renormalization effects due to spin fluctuations, which usually suppress long-range magnetic orders [22]. This results in theoretically calculated magnetic moments that are

---

<sup>1</sup>reproduced from Ref. [8] with kind permission of the publisher

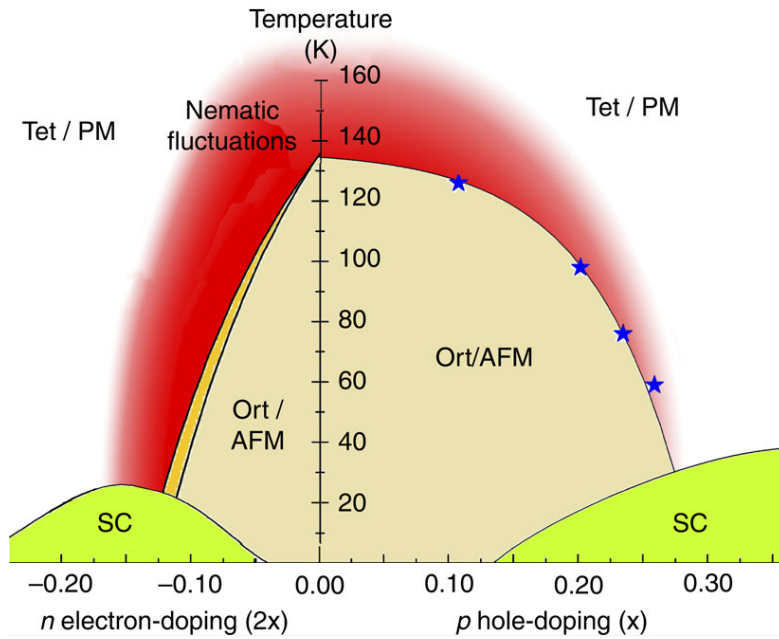


Figure 1.1.: Schematic drawing of the phase diagram of a typical pnictide high- $T_c$  superconductor, reprinted with permission from Macmillan Publishers Ltd: Nature Communications 4, 1914, Blomberg *et al.*, copyright 2013. Tet/PM stands for the tetragonal, paramagnetic phase, Ort/AFM for the orthorhombic antiferromagnetic phase and SC for the superconducting one.

considerably larger than the experimentally measured ones [23–25]. Moreover, magnetic order has been predicted for materials that exhibit no magnetism in experiments [20]. This issue is improved by including the effects of interaction and correlations, as can be done for example within the *dynamical mean-field theory* (DMFT) [26–28].

With respect to the origin of SC, it was pointed out very early that phonons cannot yield the major pairing contributions [29, 30], a fact that has been reinforced by experiments on the isotope effect [31]. It was also soon realized that the physics of the superconducting phase is more involved than in the case of cuprates due to the multi-band nature of the electronic excitations [32]. Because of the close proximity of AFM and SC, Mazing *et al.* [33] suggested a sign-changing s-wave superconducting state ( $s_{\pm}$ ), where the spin fluctuations that arise around the Fermi surface nesting vector are held responsible for the superconducting pairing. In this scenario, which is based on the idea by Berk and Schrieffer [34] that spin correlations can lead to superconducting pairing, a peak in the spin susceptibility is characteristic for the occurring attractive interactions between the electrons. Even though the spin interaction is repulsive, a superconducting pairing can take place when the order parameter of SC changes its sign along the Fermi surface. This sign change and the respective spin propagator for the superconducting

---

pairing can be related to an enhancement of the imaginary part of the transverse spin susceptibility, which also implies an instability of the system towards a magnetic order [25, 35–38]. This view has been strengthened by INS experiments, which observed that the spin fluctuations and the holes of the Fermi surface vanish together upon electron doping, suggesting that the electronic band structure is indeed closely connected to the magnetic fluctuations in these materials [39–42].

To elucidate the mechanisms behind magnetic order and superconductivity in FeSCs, a detailed knowledge of the spin susceptibility is therefore needed. With respect to itinerant magnetism, calculations have been undertaken to shed light on the Fermi surface nesting in these compounds and the consequences for emerging long-range magnetic orders. To detect Fermi surface nesting, early studies focused on bare susceptibilities in the *constant matrix element approximation* (CMA), where all matrix elements are set to unity [7, 33, 43, 44]. They showed that there is indeed considerable nesting of the Fermi surfaces and that the Fermi surface vector corresponds in most cases to the long-range magnetic order observed in experiments. It was also noted that the increasing  $T_c$  with doping or pressure is related to a decrease of the Fermi surface nesting and that the bare susceptibility reacts strongly to changes in the electron band structure.

Regarding the superconducting phase, computations that also took into account the matrix elements of the bare susceptibilities have been reported as well. In these studies, a strong response of the susceptibility was found as well, substantiating the  $s_{\pm}$  pairing scenario. It was also argued that by the inclusion of interactions, the main features observed in the non-interacting quantities will survive or even be enhanced [17, 33]. In order to describe the underlying physics better, interactions have to be included and many different techniques have been used to investigate the origin of SC in FeSCs by calculating full susceptibilities. These include, among others, methods based on the *random phase approximation* [45–48], *renormalization group* [18, 49] and *fluctuation exchange* [50, 51]. Of particular note is the work by Essenberg and collaborators [52, 53], who developed a completely *ab initio* theory to treat SC in FeSCs. All these calculations are in agreement with a pairing that is induced by spin fluctuations, although the order parameter does not always have to exhibit  $s_{\pm}$  symmetry.

In  $\text{KFe}_2\text{As}_2$  for example [54], which is a compound with only hole pockets, a d-wave symmetry was found to be the more favourable scenario for SC [55, 56]. A similar case is  $\text{A}_x\text{Fe}_{2-x}\text{Se}_2$ , whose Fermi surface consists of only electron pockets [57]. Moreover, it was observed that an  $s_{\pm}$ -wave gap can evolve into a d-wave gap and vice versa by doping or application of pressure [46]. Kuroki *et al.* [58] showed, that one of the most important parameters in this respect is the pnictogen height above the Fe plane. By changing this pnictogen height, it was possible to switch between nodeless (high- $T_c$ ) and nodal (low- $T_c$ ) pairing. In addition, superconducting pairing with  $s_{++}$  symmetry induced by orbital fluctuations [59–61] was proposed as well, which however is not applicable to FeSCs where a sign-change in the order parameter has been observed.<sup>2</sup>

With respect to the dynamical properties of FeSCs, neutron scattering experiments

---

<sup>2</sup>These are just a few examples of a currently very active field of research and we refer the reader to Refs. [32, 62, 63] and references therein for a more detailed review.

have supplied important information on the interplay of magnetism and superconductivity. It was found that AFM and superconductivity compete against each other in the shared parts of the phase diagram [25] and similar to other unconventional superconductors a collective magnon mode has been observed that appears below the critical temperature [64–70]. The energy of this magnon mode is related to the superconducting energy gap [71, 72] and if the  $s_{\pm}$  pairing scenario holds true, the imaginary part of the dynamic susceptibility has to exhibit a sharp peak at the ordering wave vector below the critical superconducting temperature. Such an enhanced response has indeed been found in INS experiments for several compounds [41, 65, 73, 74] and theoretical studies on dynamic susceptibilities have been performed as well. Most of these studies, however, are again based on low-energy model systems [19, 75–78] and truly first-principles calculations are very scarce [52, 53] and seldom go beyond the bare susceptibility [79, 80].

At the heart of all the aforementioned calculations of full susceptibilities and pairing propagators lie the non-interacting, bare susceptibilities. As the superconducting pairing mechanisms depend delicately on the electronic and magnetic behavior of the compounds, very accurate methods to compute bare susceptibilities are needed. Work along these directions was performed by several groups [52, 79] and it was an objective of this PhD project to develop an efficient method [80, 81] to calculate both static and dynamic bare susceptibilities from first-principles. We chose to employ a tetrahedron method along the lines of MacDonald *et al.* [82] and Rath and Freeman [83] as the basis of our program and invested much effort in improving the numerical representation of the physically relevant parts of the first Brillouin zone (1BZ). With this algorithm at our disposal, the second task was to obtain bare susceptibilities for a wide variety of different materials in the family of FeSC. We investigated the dependence of  $\chi^0$  on doping and pressure, and compared the observed behavior to the experimentally measured evolution of  $T_c$ .

Of course to quantitatively determine the dependence of  $T_c$  on doping or pressure would require the calculation of full interacting susceptibilities, but even the investigation of bare susceptibilities can reveal interesting properties of the superconducting material. We found, for example, that  $\chi^0$  is not a simple function with a few strong responses at special points, but indeed carries a lot of information in almost all parts of the 1BZ. With this knowledge, we have also assessed the effects of common approximations employed to calculate susceptibilities. We came to the conclusion that even small approximations can have a drastic effect on  $\chi^0$  and that the precise knowledge of  $\chi^0$  is therefore essential for any continuative method beyond non-interacting electrons.

Another issue of current research on FeSCs revolves around the importance of correlations in these compounds. Because the active layers of FeSCs have six electrons occupying the  $3d$  Fe orbitals, they belong to the Hund’s metals [27, 28, 84] regime. In this parameter regime, itinerant electrons and local moments are equally important and the Hund’s coupling plays a crucial role in determining the materials’ electronic and magnetic properties [85, 86]. This in turn means that neither fully itinerant methods nor completely localized ones will be able to capture the underlying physics. To overcome this problem, studies based on the DFT have been performed, where local correlation effects are included within the framework of the DMFT. By this inclusion of correlations,

---

the computed values for the magnetic moments and the resonance energies are successfully brought closer to the experimentally observed values [26,27,87]. Additionally, these investigations find a strong orbital-dependent mass enhancement, i.e., the  $t_{2g}$  orbitals have a much larger effective mass compared to the  $e_g$  orbitals. The different response of the orbitals to correlations, which is a current field of active research, puts the FeSCs in the vicinity of an orbital-selective Mott transition [28, 88–90].

Along the same lines we will present a detailed DFT+DMFT study on  $\text{LiFeO}_2\text{Fe}_2\text{Se}_2$  in the last chapter of this work and discuss the effects of correlations on the two non-equivalent Fe atoms in this compound.  $\text{LiFeO}_2\text{Fe}_2\text{Se}_2$  has only recently been synthesized and presents a fascinating new member of the family of FeSCs. It differs from all other FeSCs known so far as it comprises two types of Fe atoms in different valence states, which has profound consequences for its electronic properties. In a first step we determined the low-energy band structure and found that it is much richer compared to conventional FeSCs. Additionally, the Fermi surface is considerably different to the one of prototypical FeSCs, and by employing bare susceptibility calculations we could show that charge transfer takes place between the different layers. The stability and magnetic moments in different spin-ordered configurations have been studied with (spin-polarized) DFT and DFT+U approaches and while the magnetic moments of the two Fe atoms are large compared to other FeSCs, we found that spin fluctuations are still possible due to a plethora of metastable magnetic configurations with energies close to the ground state energy. The non-equivalence of the two iron atoms has even more pronounced effects when correlations are included in the framework of DMFT. We found that this material constitutes a remarkable case of a real compound where two different realizations of correlation effects based on the Hund’s coupling are present. In addition, correlations remove almost all contributions from the Fe in the  $\text{LiFeO}_2$  layer from the Fermi surface, thus recovering the usual FeSC low-energy band structure.

We think that the results presented in this thesis will help to understand the underlying physics of FeSCs. Especially with respect to the fact that the bare susceptibility is a quantity that cannot be obtained within rough approximations, our newly developed implementation of the tetrahedron method provides a tested foundation to calculate  $\chi^0$  accurately and efficiently. As electronic susceptibilities are at the heart of many important physical quantities, such as the specific heat, electrical and thermal resistivity, dielectric response, electron screening and optical reflectivity and conductivity, our method might prove useful in many different kinds of fields [91–93].

The future objectives are also clearly laid out, i.e., building a method upon the bare susceptibility that allows to include interactions and correlations in order to move the theoretically obtained  $\chi$  closer to the experimental one. As mentioned before, our last study on  $\text{LiFeO}_2\text{Fe}_2\text{Se}_2$  and others on different materials [27, 28, 87, 94] proved that correlations have profound effects on the low-energy behavior of FeSCs and in order to assess the physical properties correctly, comprehensive investigations with many different state-of-the-art methods will have to be performed in future.

This thesis is organized in two big parts; the first containing the background needed to understand the executed calculations and the second comprising the obtained results and discussions thereof. In detail, the structure is as follows.

After this introductory section, we recapitulate in Sec. 2 the theory behind the electronic susceptibility calculations we used in the later chapters of this work. For these derivations we use the Green's functions approach, usually employed to discuss the polarization function and effective potential of an electronic system. As this theory allows for a very intuitive graphical interpretation of all formulas, we adopt it to derive expressions for *bare* susceptibilities, which are mathematically equivalent to polarization functions within the simplest *single bubble* approximation. We have tried to keep this summary of the theoretical concepts as compact as possible by referring to popular textbooks for the basic derivations, while still providing discussions on all important aspects of the theory.

This section is followed by Sec. 3, where we describe in detail our numerical implementation of the tetrahedron method. We explain in short the numerically simple method by MacDonald *et al.* [82], on which our newly developed program is based on. After an elaborate illustration of our algorithms, we compare our method with the former one, highlighting the areas where important improvements have been made.

The subsequent Sec. 4 includes work that has been published in Ref. [80]. The aim of this project, which was carried out with the help of Heinrich Sormann, Lilia Boeri, Markus Aichhorn and Wolfgang von der Linden, was to present our newly developed implementation of the tetrahedron method and discuss the effects of the most common approximations in this framework.

The next two sections comprise two selected examples of materials for which we performed bare susceptibility calculations. In Sec. 5 we examine one of the most popular iron-based superconductors, i.e. LaFeAsO. There, we investigate the doping dependence of the electronic structure of this prototypical FeSC. We will also compare the behavior of the bare susceptibility with the evolution of  $T_c$  upon doping and arrive at the conclusion that continuative methods that consider interactions as well have to be applied in order to understand the recently observed *double-dome* feature of the superconducting phase. The next Sec. 6 originates from a project made available under Ref. [81]. In collaboration with Markus Aichhorn, Heinrich Sormann, Ewald Schachinger and Wolfgang von der Linden, the author of this work studied the pressure dependence of the most simple iron-based superconductor FeSe. We present results of the static bare susceptibility for FeSe for various hydrostatic and non-hydrostatic pressures and compare our results with the measured dependence of  $T_c$  when pressure is applied.

After the last three chapters, which cover the dependence of  $\chi^0$  for different classes of FeSCs, we present a more comprehensive investigation of the recently synthesized FeSC  $\text{LiFeO}_2\text{Fe}_2\text{Se}_2$  in Sec. 7, published in Ref. [95]. In this study, acquired with the help of Lilia Boeri, Heinrich Sormann, Wolfgang von der Linden and Markus Aichhorn, we investigated the effect on the electronic and magnetic structure of the iron valence in the two layers this superconductor is comprised of. To provide a conclusive physical picture of this compound, we not only calculate electronic quantities at the level of DFT, but also include correlations in the framework of DMFT.

---

For sections 4, 6 and 7 we adopted the same texts and figures as used for the corresponding publications, i.e. Refs. [80,81] and [95], respectively. By keeping the coherence of these sections, we enable the reader to study these chapters individually without the need to go through the introductory chapters first. The author of this work affirms to have contributed in all stages of the projects, which include an extensive literature search, analytical considerations, the development, implementation and testing of the numerical methods, evaluation of the results, and writing of the manuscripts.



**Part I.**

**Background**



## Chapter 2.

### Theoretical Background

The so-called *dynamical structure factor*  $S(\mathbf{q}, \omega)$ , measured in inelastic neutron scattering (INS) experiments, plays an important role for theoretical investigations as it allows for a direct comparison of theory and experiment. To be more precise,  $S(\mathbf{q}, \omega)$  is directly proportional to the imaginary part of the susceptibility function  $\chi(\mathbf{q}, \omega)$ . The neutrons represent a magnetic perturbation to the system that varies in space and time and the quantity that is measured in INS experiments is the inelastic scattering cross section [96]. In the first-order Born approximation, the differential cross section  $\frac{d^2\sigma}{d\Omega d\omega}$  for the inelastic scattering of slow neutrons for a metal in the paramagnetic phase is given by [97, 98]

$$\frac{d^2\sigma}{d\Omega d\omega} = \frac{1}{2\pi\hbar} \left( \frac{g_N r_0}{\mu_B} \right)^2 \frac{k'}{k} S_{+-}(\mathbf{q}, \omega), \quad (2.1)$$

where  $k$  and  $k'$  are the absolute values of the wave vectors of the incident and final neutron state, respectively. The gyromagnetic ratio  $g_N$  for neutrons is 1.91,  $r_0$  is the classical electron radius and  $\mu_B$  is the Bohr magneton.

In this respect,  $S_{+-}(\mathbf{q}, \omega)$  is the magnetic dynamical structure factor of the system and describes the probability for a process in which the system changes its energy by  $\hbar\omega$  and the momentum by  $\hbar\mathbf{q}$  due to the scattering of a neutron. The subscript  $+-$  indicates that a spin flip of the electron occurs simultaneously. In mathematical terms, this can be expressed as

$$S_{+-}(\mathbf{q}, \omega) = \int d^3x \int d^3x' e^{-i\mathbf{q}\cdot(\mathbf{x}-\mathbf{x}')} \int_{-\infty}^{+\infty} dt e^{i\omega t} \langle \hat{m}_+(\mathbf{x}, t) \hat{m}_-(\mathbf{x}', 0) \rangle, \quad (2.2)$$

with  $\hat{m}_\pm(\mathbf{x}, t) = \hat{m}_x(\mathbf{x}, t) \pm i\hat{m}_y(\mathbf{x}, t)$ . These  $\hat{m}_i$  are the magnetic moment density operators and in the case of the magnetic field pointing in  $z$ -direction, the  $x$  and  $y$  components are given by

$$\begin{aligned} \hat{m}_x &= -\mu_B \left( \hat{c}_\downarrow^\dagger \hat{c}_\uparrow + \hat{c}_\uparrow^\dagger \hat{c}_\downarrow \right) \\ \hat{m}_y &= -i\mu_B \left( \hat{c}_\downarrow^\dagger \hat{c}_\uparrow - \hat{c}_\uparrow^\dagger \hat{c}_\downarrow \right). \end{aligned} \quad (2.3)$$

Here we have introduced the field operator  $\hat{c}_\uparrow^\dagger(\mathbf{x}, t)$  creating an electron with up-spin at position  $\mathbf{x}$  and time  $t$ . The structure factor obeys two important constraints. First, the energy gain and loss during the scattering are related by the principle of detailed balance

$$S_{+-}(\mathbf{q}, -\omega) = e^{-\frac{\hbar\omega}{k_B T}} S_{+-}(\mathbf{q}, \omega), \quad (2.4)$$

which connects processes where the neutron loses energy with processes where the neutron gains energy.<sup>1</sup> Second, as the interaction is very weak, we can assume the system to respond linearly to the perturbation. This allows us to use the fluctuation-dissipation theorem (see for example Ref. [99]), which states that the evolution of a system due to an externally induced perturbation is similar to that of a spontaneous fluctuation. This is expressed by the following equation

$$\begin{aligned} S_{+-}(\mathbf{q}, \omega) &= -2\hbar \int d^3x \int d^3x' e^{-i\mathbf{q}\cdot(\mathbf{x}-\mathbf{x}')} \text{Im}\chi_\pm(\mathbf{x}, \mathbf{x}', \omega) \\ &= -2\hbar\Omega \text{Im}\chi_\pm(\mathbf{q}, \omega) \end{aligned} \quad (2.5)$$

and offers a perfect testing ground for our theoretical calculations, as it connects the structure factor with the imaginary part of the *spin* susceptibility, indicated by the subscript  $\pm$ .<sup>2</sup> An analogous relation exists between the dynamical *charge* structure factor  $S_c(\mathbf{q}, \omega)$  and the *charge* susceptibility  $\chi_c(\mathbf{q}, \omega)$

$$S_c(\mathbf{q}, \omega) = -2\hbar\Omega \text{Im}\chi_c(\mathbf{q}, \omega) \quad (2.6)$$

In addition, the *static* spin susceptibility, i.e.,  $\chi_\pm(\mathbf{q}, \omega = 0)$ , describes the response of the spin system to a static magnetic field that varies spatially. In other words, the  $\mathbf{q}$  vector for which the static susceptibility becomes very large (or even diverges) marks the point of an instability of the system towards long-range magnetic order. For this reason,  $\chi_\pm(\mathbf{q})$  has become a favorite quantity to investigate the antiferromagnetic ground states of currently very often studied systems such as the FeSCs.

In this chapter we want to recapitulate the theory behind the electronic susceptibility as it is used in the course of this work. There are in fact two different approaches to derive  $\chi$ , the first one making use of the analogy to a charge density system and employs the Green's functions technique, while the second one utilizes first-order perturbation theory to evaluate the response to an external magnetic field. In the following, we want to stay in the Green's function formalism, as it is standard in most textbooks and also provides a very descriptive graphical representation in the form of Feynman diagrams. As this technique is usually employed to describe the effects of electronic interactions based on the Coulomb potential, we will first introduce the charge susceptibility function describing the reaction of the density of an electron gas to an external electric potential.

The following summary follows Ref. [92], although similar derivations can be found in many textbooks on many-body theory, as for example Refs. [91] and [93].

---

<sup>1</sup>As always,  $\hbar$  is the reduced Planck's constant and  $k_B T$  is the product of the Boltzmann's constant and the thermodynamical temperature.

<sup>2</sup>Here,  $\Omega$  is the normalization volume.

## 2.1. The Response Functions $\chi_{\pm}$ and $\chi_c$

The magnetic spin susceptibility  $\chi_{\pm}$  connects in linear relation the space- and time-dependent perturbing magnetic potential  $\mathbf{B}_{ext}(\mathbf{r}, t)$  with the corresponding induced electron spin density  $\mathbf{m}$

$$\delta\mathbf{m}(\mathbf{r}, t) = \int d^3r' \int_{-\infty}^t dt' \chi_{\pm}(\mathbf{r}, \mathbf{r}', t - t') \delta\mathbf{B}(\mathbf{r}', t'). \quad (2.7)$$

A similar relation can be found to connect the electron charge density  $\delta\rho$  with an external perturbing field  $V_{ext}$  by the means of the charge susceptibility  $\chi_c$ .

$$\delta\rho(\mathbf{r}, t) = \int d^3r' \int_{-\infty}^t dt' \chi_c(\mathbf{r}, \mathbf{r}', t - t') V_{ext}(\mathbf{r}', t'). \quad (2.8)$$

Tightly connected to the concept of susceptibility functions is the occurrence of a dynamical effective interaction potential  $W$ . This effective interaction takes into account that the electron density will react to the external potential and respond with screening effects, thus changing the value of the potential. All perturbations considered, the effective interaction potential will in general be a function of both space and time. If the electronic system is homogenous in time, however, one can use a Fourier transformation to frequency space and obtain a short notation for the dynamical effective interaction potential  $W(\mathbf{r}, \mathbf{r}', \omega)$

$$W(\mathbf{r}_1, \mathbf{r}_2, \omega) = v(\mathbf{r}_1 - \mathbf{r}_2) + \int \int d^3x d^3x' W(\mathbf{r}_1, \mathbf{x}, \omega) \chi_c(\mathbf{x}, \mathbf{x}', \omega) v(\mathbf{x}' - \mathbf{r}_2) \quad (2.9)$$

where we abbreviated the bare Coulomb potential  $v(\mathbf{r}_1 - \mathbf{r}_2)$  by

$$v(\mathbf{r}_1 - \mathbf{r}_2) = \frac{e^2}{|\mathbf{r}_1 - \mathbf{r}_2|}.$$

A further simplification can be made if the system we are investigating is also homogenous in space, i.e., only the difference in the coordinates  $\delta\mathbf{r} = \mathbf{r}_1 - \mathbf{r}_2$  matters. In this case it is convenient to change from real space into wave vector space via a second Fourier transformation. After this, Eq. (2.9) can be very compactly written in the form

$$W(\mathbf{q}, \omega) = v(\mathbf{q}) + W(\mathbf{q}, \omega) \chi_c^{ir}(\mathbf{q}, \omega) v(\mathbf{q}), \quad (2.10)$$

where  $\chi_c^{ir}$  is the *irreducible* susceptibility function. This function includes all polarization parts which cannot be broken in two by “cutting” only one interaction line.<sup>3</sup> Because of the singularity of the Coulomb potential at  $|\mathbf{r}_1 - \mathbf{r}_2| = 0$ , one has to take care when performing the Fourier transform. To treat it properly, the Coulomb potential can be

<sup>3</sup>For a more detailed description we refer the reader to Refs. [100] and [101].

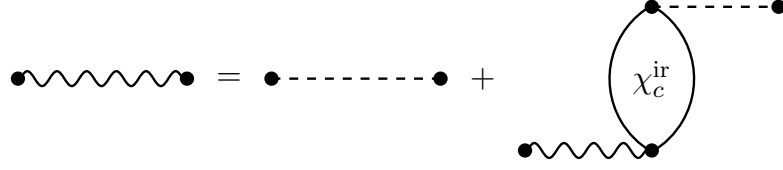


Figure 2.1.: Graphical representation of Eq. (2.10) to calculate the effective interaction potential  $W$  (wavy line). The dotted lines represent bare Coulomb interactions and the irreducible charge susceptibility is indicated by  $\chi_c^{\text{ir}}$ .

considered as the limit of the Yukawa potential. This way, one can avoid the singularity and by setting the zero point of the potential to be at  $|\mathbf{q}| = 0$ , one arrives at the well-defined expression

$$v(\mathbf{q}) = \frac{4\pi e^2}{|\mathbf{q}|^2} \quad \text{with } v(0) = 0.$$

As mentioned in the introduction of this chapter, one of the advantages to use the Green's function approach is its very descriptive graphical representation via Feynman diagrams (see Ref. [100]). This is demonstrated in Fig. 2.1, which illustrates schematically Eq. (2.10). The wavy line represents the full interaction  $W$ , while the dashed one stands for the bare Coulomb potential  $v(\mathbf{q})$ . The solid lines represent non-interacting Green's functions.

For all calculations we want to perform on real materials, the spatial homogeneity is unfortunately no longer present. This complicates the Fourier transformation from real to reciprocal space considerably. We are in good approximation, however, still working with a crystal, i.e. within a perfectly periodic lattice. For a general function that depends on two coordinates  $\mathbf{r}_1$  and  $\mathbf{r}_2$  the transformation in a periodic lattice reads

$$f(\mathbf{r}_1, \mathbf{r}_2) = \frac{1}{\Omega} \sum_{\mathbf{q}} e^{i\mathbf{q} \cdot (\mathbf{r}_1 - \mathbf{r}_2)} \sum_{\mathbf{K}_1} \sum_{\mathbf{K}_2} e^{i\mathbf{K}_1 \cdot \mathbf{r}_1} e^{-i\mathbf{K}_2 \cdot \mathbf{r}_2} f_{\mathbf{K}_1, \mathbf{K}_2}(\mathbf{q}). \quad (2.11)$$

Here,  $\mathbf{q}$  is a vector confined to the first Brillouin zone (1BZ) with volume  $\Omega$  and  $\mathbf{K}_i$  is a reciprocal lattice vector. All quantities of Eq. (2.9) are functions of the same type as  $f$  and we can write for the components with reciprocal lattice vectors  $\mathbf{K}_1$  and  $\mathbf{K}_2$

$$W_{\mathbf{K}_1, \mathbf{K}_2}(\mathbf{q}, \omega) = v_{\mathbf{K}_1, \mathbf{K}_2}(\mathbf{q}) + \sum_{\mathbf{K}, \mathbf{K}'} W_{\mathbf{K}_1, \mathbf{K}'}(\mathbf{q}, \omega) \chi_{\mathbf{K}', \mathbf{K}}^{\text{ir}}(\mathbf{q}, \omega) v_{\mathbf{K}, \mathbf{K}_2}(\mathbf{q}) \quad (2.12)$$

All quantities in the above equation are matrices in the space of reciprocal lattice vectors and with tildes representing matrices,<sup>4</sup> Eq. (2.12) takes the form

$$\tilde{W}(\mathbf{q}, \omega) = \tilde{v}(\mathbf{q}) + \tilde{W}(\mathbf{q}, \omega) \tilde{\chi}_c^{\text{ir}}(\mathbf{q}, \omega) \tilde{v}(\mathbf{q}), \quad (2.13)$$

<sup>4</sup>The subscript  $c$  to indicate that we are talking about the charge susceptibility has been dropped for the moment to create space for the reciprocal lattice vectors.

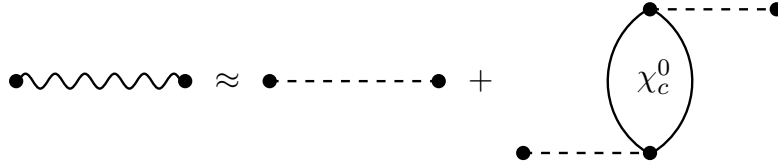


Figure 2.2.: Graphical representation of Eq. (2.14) to approximately calculate the effective interaction potential  $W$  (wavy line). The dotted lines represent bare Coulomb potentials and the solid lines non-interacting Green's functions.

which resembles the scalar Eq. (2.10) for the interaction potential, derived for systems homogenous in space, very closely. We want to note at this point that due to the simple structure of the bare Coulomb interaction in real space,  $\tilde{v}(\mathbf{q})$  in Eq. (2.13) is a diagonal matrix in reciprocal space of the form

$$v_{\mathbf{K}_1, \mathbf{K}_2}(\mathbf{q}) = v(\mathbf{q} + \mathbf{K}_1) \delta_{\mathbf{K}_1, \mathbf{K}_2} .$$

## 2.2. The Bare Susceptibility $\chi^0$

The charge susceptibility  $\chi_c$  is the sum of all possible polarization insertions. Since the exact evaluation of all these contributions cannot be done, we need to make some approximations for  $\chi_c$  and restrict the sum to those diagrams which we find vital to describe the physics of our materials. A very common choice is to restrict oneself to one single particle-hole scattering processe, as expressed by Eq. (2.14) and graphically depicted in Fig. 2.2.

$$W(\mathbf{q}, \omega) \approx v(\mathbf{q}) + v(\mathbf{q}) \chi_c^0(\mathbf{q}, \omega) v(\mathbf{q}) . \quad (2.14)$$

Additionally, we provide a graphical description of the *bare bubble insertion*  $\chi_c^0$  in Fig. 2.3. The solid lines, again, stand for non-interacting (*bare*) Green's functions, one going from the vertex at  $\mathbf{r}'$  to  $\mathbf{r}$  with an energy  $\omega'$  and the other from  $\mathbf{r}$  to  $\mathbf{r}'$  with the energy  $\omega' - \omega$ .<sup>5</sup> Figuratively speaking, this describes a process where a particle-hole pair is created at  $\mathbf{r}'$ , with the particle having an energy of  $\hbar\omega'$  and the hole  $\hbar(\omega' - \omega)$ , which is then destroyed at  $\mathbf{r}$ . According to the rules of Feynman's graph theory,  $\chi_c^0$  is therefore written as follows

$$\chi_c^0(\mathbf{r}, \mathbf{r}', \omega) = -\frac{i}{\pi\hbar} \int_{-\infty}^{+\infty} d\omega' G^0(\mathbf{r}, \mathbf{r}', \omega') G^0(\mathbf{r}', \mathbf{r}, \omega' - \omega) \quad (2.15)$$

$$= \frac{1}{2\mu_B^2} \chi_{\pm}^0(\mathbf{r}, \mathbf{r}', \omega) \quad (2.16)$$

In the framework of our theoretical considerations the charge susceptibility  $\chi_c^0$  and the spin susceptibility  $\chi_{\pm}^0$  are mathematically identical and we will therefore drop the superscript for the following chapters of this work.

<sup>5</sup>With the superscript 0 we want to make clear that we are dealing with non-interacting *bare* quantities.

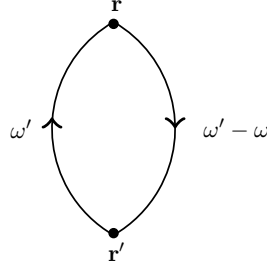


Figure 2.3.: Single particle-hole polarization insertion  $\chi_c^0$ , which is identical to  $\chi_{\pm}^0$ .

Since we are still working within a perfectly periodic lattice, it is reasonable to express the electron propagators in a basis of Bloch waves. The non-interacting *bare* Green's function in such a basis reads

$$G^0(\mathbf{r}, \mathbf{r}', \omega) = \sum_{\mathbf{k}} \sum_{n, n'}^{\text{1BZ}} \psi_{n, \mathbf{k}}(\mathbf{r}) \psi_{n', \mathbf{k}}^*(\mathbf{r}') G_{n, n'}^0(\mathbf{k}, \omega),$$

where  $\mathbf{k}$  is again a vector constrained to the 1BZ and  $n, n'$  are electron band indices.  $\psi_{n, \mathbf{k}}(\mathbf{r})$  are Bloch-type wave functions of the electrons in the crystal. To evaluate Eq. (2.15), we need to obtain the non-interacting Green's functions, which are diagonal in band space

$$G_{n, n'}^0(\mathbf{k}, \omega) = F_{n, \mathbf{k}}(\omega) \delta_{n, n'},$$

with

$$F_{n, \mathbf{k}}(\omega) = \frac{\Theta(\epsilon_F - \epsilon_{n, \mathbf{k}}^0)}{\omega - \omega_{n, \mathbf{k}}^0 - i\eta} + \frac{\Theta(\epsilon_{n, \mathbf{k}}^0 - \epsilon_F)}{\omega - \omega_{n, \mathbf{k}}^0 + i\eta}. \quad (2.17)$$

In Eq. (2.17) we used  $\epsilon_{n, \mathbf{k}}^0 = \hbar\omega_{n, \mathbf{k}}^0$  as abbreviation for the Bloch energy corresponding to the eigenfunction  $\psi_{n, \mathbf{k}}$ . Plugging these expression for the Green's functions into Eq. (2.15) for the susceptibility function,<sup>6</sup> we get

$$\chi^T(\mathbf{r}, \mathbf{r}', \omega) = \frac{2}{\pi} \sum_{\mathbf{k}_1, \mathbf{k}_2}^{\text{1BZ}} \sum_{n, m} \psi_{n, \mathbf{k}_1}(\mathbf{r}) \psi_{n, \mathbf{k}_1}^*(\mathbf{r}') \psi_{m, \mathbf{k}_2}(\mathbf{r}') \psi_{m, \mathbf{k}_2}^*(\mathbf{r}) \int_{-\infty}^{+\infty} \frac{d\omega'}{2\pi i} F_{n, \mathbf{k}_1}(\omega') F_{m, \mathbf{k}_2}(\omega' - \omega) \quad (2.18)$$

In above equation, a new superscript  $T$  has been introduced, which indicates that we are using time-ordered Green's functions. These have the advantage that one can make use of the Feynman's diagrammatic method. On the other hand, however, they do not obey causality, a necessary property for physical response functions. We will therefore derive our theory with time-ordered quantities and then, before doing the actual numerical evaluation, transform them into retarded functions.

<sup>6</sup>As in the following we have to discuss the properties of time-ordered and retarded functions, indicated by the superscripts  $T$  and  $R$ , we are omitting the superscript 0 for the moment.

We want to write  $\chi^0$  in wave vector space and therefore need to Fourier transform Eq. (2.18). The inverse Fourier transform of our general function from Eq. (2.11) is written as

$$f_{\mathbf{K}_1, \mathbf{K}_2}(\mathbf{q}) = \frac{1}{\Omega} \int_{\Omega} \int_{\Omega} d^3r d^3r' e^{-i(\mathbf{q}+\mathbf{K}_1)\cdot\mathbf{r}} e^{i(\mathbf{q}+\mathbf{K}_2)\cdot\mathbf{r}'} f(\mathbf{r}, \mathbf{r}') , \quad (2.19)$$

where the integrals are performed over the volume of the 1BZ. Applying this to our susceptibility function gives us

$$\begin{aligned} \chi_{\mathbf{K}_1, \mathbf{K}_2}^T(\mathbf{q}, \omega) &= \frac{2}{\hbar\Omega} \sum_{n,m} \sum_{\mathbf{k}_1, \mathbf{k}_2}^{\text{1BZ}} \int_{-\infty}^{+\infty} \frac{d\omega'}{2\pi i} F_{n, \mathbf{k}_1}(\omega') F_{m, \mathbf{k}_2}(\omega' - \omega) \cdot \\ &\cdot \int_{\Omega} d^3r e^{-i(\mathbf{q}+\mathbf{K}_1)\cdot\mathbf{r}} \psi_{n, \mathbf{k}_1}(\mathbf{r}) \psi_{m, \mathbf{k}_2}^*(\mathbf{r}) \int_{\Omega} d^3r' e^{i(\mathbf{q}+\mathbf{K}_2)\cdot\mathbf{r}'} \psi_{n, \mathbf{k}_1}^*(\mathbf{r}') \psi_{m, \mathbf{k}_2}(\mathbf{r}') \end{aligned} \quad (2.20)$$

In a perfectly periodic crystal, the integrals in the above equation have to be invariant with respect to a translation of their center of integration by a primitive lattice vector  $\mathbf{R}$ , i.e.

$$\int_{\Omega} d^3r e^{-i(\mathbf{q}+\mathbf{K}_1)\cdot\mathbf{r}} \psi_{n, \mathbf{k}_1}(\mathbf{r}) \psi_{m, \mathbf{k}_2}^*(\mathbf{r}) \stackrel{!}{=} \int_{\Omega} d^3r e^{-i(\mathbf{q}+\mathbf{K}_1)\cdot(\mathbf{r}+\mathbf{R})} \psi_{n, \mathbf{k}_1}(\mathbf{r} + \mathbf{R}) \psi_{m, \mathbf{k}_2}^*(\mathbf{r} + \mathbf{R}) .$$

Since the eigenfunctions are all Bloch functions, i.e.  $\psi_{n, \mathbf{k}}(\mathbf{r}) = e^{i\mathbf{k}\cdot\mathbf{R}} \psi_{n, \mathbf{k}}(\mathbf{r} + \mathbf{R})$ , the relation above simplifies to

$$\int_{\Omega} d^3r e^{-i(\mathbf{q}+\mathbf{K}_1)\cdot\mathbf{r}} \psi_{n, \mathbf{k}_1}(\mathbf{r}) \psi_{m, \mathbf{k}_2}^*(\mathbf{r}) \stackrel{!}{=} e^{-i(\mathbf{k}_2 - \mathbf{k}_1 + \mathbf{q})\cdot\mathbf{R}} \int_{\Omega} d^3r e^{-i(\mathbf{q}+\mathbf{K}_1)\cdot\mathbf{r}} \psi_{n, \mathbf{k}_1}(\mathbf{r}) \psi_{m, \mathbf{k}_2}^*(\mathbf{r}) ,$$

which is fulfilled for

$$\mathbf{k}_1 \stackrel{!}{=} \mathbf{k}_2 + \mathbf{q} + \mathbf{G} .$$

Here we introduced the reciprocal lattice vector  $\mathbf{G}$  that guarantees that  $\mathbf{k}_2 + \mathbf{q}$  and consequently  $\mathbf{k}_1$  are vectors of the 1BZ. To improve the readability of our equations we want to use Dirac's notation to express integrals of the form

$$\int_{\Omega} d^3r e^{-i(\mathbf{q}+\mathbf{K}_1)\cdot\mathbf{r}} \psi_{n, \mathbf{k}_1}(\mathbf{r}) \psi_{m, \mathbf{k}_2}^*(\mathbf{r}) =: \langle m, \mathbf{k}_1 | e^{-i(\mathbf{q}+\mathbf{K}_1)\cdot\mathbf{r}} | n, \mathbf{k}_1 \rangle$$

We will also omit writing the vector  $\mathbf{G}$  explicitly in all equations. We leave it to the reader to insert  $\mathbf{G}$  to all combinations of  $\mathbf{q} + \mathbf{k}$  whenever this sum reaches out of 1BZ. With all this, Eq. (2.20) becomes

$$\begin{aligned} \chi_{\mathbf{K}_1, \mathbf{K}_2}^T(\mathbf{q}, \omega) &= \frac{2}{\hbar\Omega} \sum_{n,m} \sum_{\mathbf{k}}^{\text{1BZ}} \int_{-\infty}^{+\infty} \frac{d\omega'}{2\pi i} F_{n, \mathbf{k}+\mathbf{q}}(\omega') F_{m, \mathbf{k}}(\omega' - \omega) \cdot \\ &\cdot \langle m, \mathbf{k} | e^{-i(\mathbf{q}+\mathbf{K}_1)\cdot\mathbf{r}} | n, \mathbf{k} + \mathbf{q} \rangle \langle n, \mathbf{k} + \mathbf{q} | e^{i(\mathbf{q}+\mathbf{K}_2)\cdot\mathbf{r}} | m, \mathbf{k} \rangle \end{aligned} \quad (2.21)$$

To evaluate the integral over frequency, we write out in full the product of  $F_{n,\mathbf{k}+\mathbf{q}}(\omega') \cdot F_{m,\mathbf{k}}(\omega' - \omega)$ , as given in Eq. (2.17).

$$\int_{-\infty}^{+\infty} \frac{d\omega'}{2\pi i} F_{n,\mathbf{k}+\mathbf{q}}(\omega') F_{m,\mathbf{k}}(\omega' - \omega) = \int_{-\infty}^{+\infty} \frac{d\omega'}{2\pi i} \left( \frac{\Theta(\epsilon_F - \epsilon_{n,\mathbf{k}+\mathbf{q}}^0)}{\omega' - \omega_{n,\mathbf{k}+\mathbf{q}}^0 - i\eta} + \frac{\Theta(\epsilon_{n,\mathbf{k}+\mathbf{q}}^0 - \epsilon_F)}{\omega' - \omega_{n,\mathbf{k}+\mathbf{q}}^0 + i\eta} \right) \cdot \left( \frac{\Theta(\epsilon_F - \epsilon_{m,\mathbf{k}}^0)}{\omega' - \omega - \omega_{m,\mathbf{k}}^0 - i\eta} + \frac{\Theta(\epsilon_{m,\mathbf{k}}^0 - \epsilon_F)}{\omega' - \omega - \omega_{m,\mathbf{k}}^0 + i\eta} \right)$$

Making use of Cauchy's residue theorem one can perform the  $\omega'$  integral in the complex plane. Since terms with poles with higher order than one have a vanishing contribution, we only have to take into account terms with poles of order one. In connection with Jordan's lemma we can write [102]

$$\int_{-\infty}^{+\infty} \frac{d\omega'}{2\pi i} F_{n,\mathbf{k}+\mathbf{q}}(\omega') F_{m,\mathbf{k}}(\omega' - \omega) = \frac{\Theta(\epsilon_{n,\mathbf{k}+\mathbf{q}}^0 - \epsilon_F) \Theta(\epsilon_F - \epsilon_{m,\mathbf{k}}^0)}{\omega + \omega_{m,\mathbf{k}}^0 - \omega_{n,\mathbf{k}+\mathbf{q}}^0 + i\eta} - \frac{\Theta(\epsilon_F - \epsilon_{n,\mathbf{k}+\mathbf{q}}^0) \Theta(\epsilon_{m,\mathbf{k}}^0 - \epsilon_F)}{\omega + \omega_{m,\mathbf{k}}^0 - \omega_{n,\mathbf{k}+\mathbf{q}}^0 - i\eta} \quad (2.22)$$

Plugging the expression for the integral in Eq. (2.22) into Eq. (2.21), we finally arrive at the desired result for the time-ordered susceptibility function  $\chi^T$ .

$$\chi_{\mathbf{K}_1, \mathbf{K}_2}^T(\mathbf{q}, \omega) = \frac{2}{\hbar\Omega} \sum_{n,m} \sum_{\mathbf{k}}^{1\text{BZ}} \left( \frac{\Theta(\epsilon_{n,\mathbf{k}+\mathbf{q}}^0 - \epsilon_F) \Theta(\epsilon_F - \epsilon_{m,\mathbf{k}}^0)}{\omega + \omega_{m,\mathbf{k}}^0 - \omega_{n,\mathbf{k}+\mathbf{q}}^0 + i\eta} - \frac{\Theta(\epsilon_F - \epsilon_{n,\mathbf{k}+\mathbf{q}}^0) \Theta(\epsilon_{m,\mathbf{k}}^0 - \epsilon_F)}{\omega + \omega_{m,\mathbf{k}}^0 - \omega_{n,\mathbf{k}+\mathbf{q}}^0 - i\eta} \right) \cdot \langle m, \mathbf{k} | e^{-i(\mathbf{q}+\mathbf{K}_1)\cdot\mathbf{r}} | n, \mathbf{k} + \mathbf{q} \rangle \langle n, \mathbf{k} + \mathbf{q} | e^{i(\mathbf{q}+\mathbf{K}_2)\cdot\mathbf{r}} | m, \mathbf{k} \rangle. \quad (2.23)$$

As said before, physical response functions have to have the property of causality, which is violated by time-ordered quantities. We therefore have to transform Eq. (2.23) to write  $\chi$  as a retarded quantity. There is a close relation between time-ordered and retarded functions, which can be summarized the following way [92, 101]

$$\begin{aligned} \text{Re}(\chi^R(\mathbf{q}, -\omega)) &= \text{Re}(\chi^T(\mathbf{q}, \omega)) \\ \text{Im}(\chi^R(\mathbf{q}, -\omega)) &= \text{Im}(\chi^T(\mathbf{q}, \omega)) \cdot \text{sgn}(\omega) \end{aligned} \quad (2.24)$$

With these expressions, we can write the retarded susceptibility function  $\chi^R$  like

$$\chi_{\mathbf{K}_1, \mathbf{K}_2}^R(\mathbf{q}, \omega) = \frac{2}{\hbar\Omega} \sum_{n,m} \sum_{\mathbf{k}}^{1\text{BZ}} \left( \frac{\Theta(\epsilon_{n,\mathbf{k}+\mathbf{q}}^0 - \epsilon_F) \Theta(\epsilon_F - \epsilon_{m,\mathbf{k}}^0)}{\omega + \omega_{m,\mathbf{k}}^0 - \omega_{n,\mathbf{k}+\mathbf{q}}^0 + i\eta} - \frac{\Theta(\epsilon_F - \epsilon_{n,\mathbf{k}+\mathbf{q}}^0) \Theta(\epsilon_{m,\mathbf{k}}^0 - \epsilon_F)}{\omega + \omega_{m,\mathbf{k}}^0 - \omega_{n,\mathbf{k}+\mathbf{q}}^0 + i\eta} \right) \cdot \langle m, \mathbf{k} | e^{-i(\mathbf{q}+\mathbf{K}_1)\cdot\mathbf{r}} | n, \mathbf{k} + \mathbf{q} \rangle \langle n, \mathbf{k} + \mathbf{q} | e^{i(\mathbf{q}+\mathbf{K}_2)\cdot\mathbf{r}} | m, \mathbf{k} \rangle \quad (2.25)$$

As the denominator is the same in both terms, we simplify this expression by rewriting the  $\Theta$  distribution functions according to

$$\Theta(\epsilon_{n,\mathbf{k}+\mathbf{q}}^0 - \epsilon_F) \Theta(\epsilon_F - \epsilon_{m,\mathbf{k}}^0) - \Theta(\epsilon_F - \epsilon_{n,\mathbf{k}+\mathbf{q}}^0) \Theta(\epsilon_{m,\mathbf{k}}^0 - \epsilon_F) = \Theta(\epsilon_F - \epsilon_{m,\mathbf{k}}^0) - \Theta(\epsilon_F - \epsilon_{n,\mathbf{k}+\mathbf{q}}^0).$$

This gives us

$$\chi_{\mathbf{K}_1, \mathbf{K}_2}^R(\mathbf{q}, \omega) = \frac{2}{\hbar\Omega} \sum_{n,m} \sum_{\mathbf{k}}^{\text{1BZ}} \frac{\Theta(\epsilon_F - \epsilon_{m,\mathbf{k}}^0) - \Theta(\epsilon_F - \epsilon_{n,\mathbf{k}+\mathbf{q}}^0)}{\omega + \omega_{m,\mathbf{k}}^0 - \omega_{n,\mathbf{k}+\mathbf{q}}^0 + i\eta} \cdot \langle m, \mathbf{k} | e^{-i(\mathbf{q}+\mathbf{K}_1)\cdot\mathbf{r}} | n, \mathbf{k} + \mathbf{q} \rangle \langle n, \mathbf{k} + \mathbf{q} | e^{i(\mathbf{q}+\mathbf{K}_2)\cdot\mathbf{r}} | m, \mathbf{k} \rangle . \quad (2.26)$$

Equation (2.26) for  $\chi^R$  describes the answer of an electron gas in a crystal to a perturbation by a charged particle within the *bare bubble* approximation. From this point on we will only deal with retarded quantities, thus the superscript  $R$  is omitted for the sake of reintroducing 0 to differentiate between non-interacting quantities and fully interacting ones. Also, it describes the screening of the potential of the perturbation due to the electrons. In order to make a numerical evaluation feasible, we will neglect all non-diagonal elements of  $\chi_{\mathbf{K}_1, \mathbf{K}_2}$ . The effects of this approximation are most easily visible when we perform a Fourier transformation back to real space (see Eq. (2.11)) and set  $\mathbf{K}_1 = \mathbf{K}_2$ , i.e.

$$f(\mathbf{r} - \mathbf{r}') = \frac{1}{\Omega} \sum_{\mathbf{K}} \sum_{\mathbf{q}}^{\text{1BZ}} e^{i(\mathbf{q}+\mathbf{K})\cdot(\mathbf{r}-\mathbf{r}')} f_{\mathbf{K}}(\mathbf{q}) .$$

This relation makes clear that by only considering diagonal terms of  $\chi_{\mathbf{K}_1, \mathbf{K}_2}$ , we basically assume a homogenous system in real space and neglect all so-called *local field effects* of the susceptibility function. In this approximation,  $\chi^0$  reads<sup>7</sup>

$$\chi^0(\mathbf{q}, \omega) = \frac{2}{\hbar\Omega} \sum_{n,m} \sum_{\mathbf{k}}^{\text{1BZ}} \frac{\Theta(\epsilon_F - \epsilon_{m,\mathbf{k}}^0) - \Theta(\epsilon_F - \epsilon_{n,\mathbf{k}+\mathbf{q}}^0)}{\omega + \omega_{m,\mathbf{k}}^0 - \omega_{n,\mathbf{k}+\mathbf{q}}^0 + i\eta} \left| \langle m, \mathbf{k} | e^{-i(\mathbf{q}+\mathbf{K})\cdot\mathbf{r}} | n, \mathbf{k} + \mathbf{q} \rangle \right|^2 . \quad (2.27)$$

To be consistent with the notation used in Secs. 4, 6 and 7, we will use a continuous Fourier transformation in wave vector space and convert all frequencies to energies. We also use from now on the short notation  $\epsilon_{\mathbf{k}}^m = \epsilon_{m,\mathbf{k}}^0$ , giving us

$$\chi^0(\mathbf{q}, \omega) = \sum_{n,m} \frac{d\mathbf{k}}{4\pi^3} \int^{\text{1BZ}} \frac{\Theta(\epsilon_F - \epsilon_{\mathbf{k}}^m) - \Theta(\epsilon_F - \epsilon_{\mathbf{k}+\mathbf{q}}^n)}{\hbar\omega + \epsilon_{\mathbf{k}}^m - \epsilon_{\mathbf{k}+\mathbf{q}}^n + i\tilde{\eta}} \left| \langle m, \mathbf{k} | e^{-i(\mathbf{q}+\mathbf{K})\cdot\mathbf{r}} | n, \mathbf{k} + \mathbf{q} \rangle \right|^2 . \quad (2.28)$$

This quantity will be the core of all calculations performed in the following chapters of this work. Before we start with the actual numerical evaluation of  $\chi^0$ , we first want to mention and discuss some further properties of this physical quantity. By using the well-known relation [103]

$$\frac{1}{a \pm i\eta} = \text{P} \left( \frac{1}{a} \right) \mp i\pi\delta(a) , \quad (2.29)$$

<sup>7</sup>In order to facilitate readability we have omitted the subscript  $\mathbf{K}$ .

one can easily extract the real and imaginary part of  $\chi$  of Eq. (2.28), which read<sup>8</sup>

$$\text{Re}\chi^0(\mathbf{q}, \omega) = \sum_{n,m} \frac{d\mathbf{k}}{4\pi^3} \int^{1\text{BZ}} \frac{\Theta(\epsilon_F - \epsilon_{\mathbf{k}}^m) - \Theta(\epsilon_F - \epsilon_{\mathbf{k}+\mathbf{q}}^n)}{\hbar\omega + \epsilon_{\mathbf{k}}^m - \epsilon_{\mathbf{k}+\mathbf{q}}^n} \left| \langle m, \mathbf{k} | e^{-i(\mathbf{q}+\mathbf{K})\cdot\mathbf{r}} | n, \mathbf{k} + \mathbf{q} \rangle \right|^2$$

and

$$\begin{aligned} \text{Im}\chi^0(\mathbf{q}, \omega) = & - \sum_{n,m} \frac{d\mathbf{k}}{4\pi^2} \int^{1\text{BZ}} (\Theta(\epsilon_F - \epsilon_{\mathbf{k}}^m) - \Theta(\epsilon_F - \epsilon_{\mathbf{k}+\mathbf{q}}^n)) \left| \langle m, \mathbf{k} | e^{-i(\mathbf{q}+\mathbf{K})\cdot\mathbf{r}} | n, \mathbf{k} + \mathbf{q} \rangle \right|^2 \\ & \cdot \delta(\hbar\omega + \epsilon_{\mathbf{k}}^m - \epsilon_{\mathbf{k}+\mathbf{q}}^n) . \end{aligned} \quad (2.30)$$

The imaginary part for negative frequencies can be obtained by the relation

$$\text{Im}\chi^0(\mathbf{q}, -\omega) = -\text{Im}\chi^0(\mathbf{q}, \omega) . \quad (2.31)$$

As the susceptibility function given in Eq. (2.28) is now a retarded quantity and a proper physical response function, it obeys the Kramers-Kronig relation, which connects real and imaginary part of  $\chi^0$  in the following way

$$\text{Re}\chi^0(\mathbf{q}, \omega) = \frac{1}{\pi} \text{P} \left( \int_0^{\infty} d\omega' \text{Im}(\chi^0(\mathbf{q}, \omega')) \left( \frac{1}{\omega' - \omega} + \frac{1}{\omega' + \omega} \right) \right) . \quad (2.32)$$

### 2.3. The Static Bare Susceptibility

In the static limit, the susceptibility has a particular physical interpretation, as it directly measures the response of the system to a spatially varying, static magnetic field. The real part can simply be obtained by performing the limit  $\omega \rightarrow 0$  in Eq. (2.28) and then taking Cauchy's principle value again

$$\chi^0(\mathbf{q}) = \sum_{n,m} \frac{d\mathbf{k}}{4\pi^3} \int^{1\text{BZ}} \frac{\Theta(\epsilon_F - \epsilon_{\mathbf{k}}^m) - \Theta(\epsilon_F - \epsilon_{\mathbf{k}+\mathbf{q}}^n)}{\epsilon_{\mathbf{k}}^m - \epsilon_{\mathbf{k}+\mathbf{q}}^n} \left| \langle m, \mathbf{k} | e^{-i(\mathbf{q}+\mathbf{K})\cdot\mathbf{r}} | n, \mathbf{k} + \mathbf{q} \rangle \right|^2 . \quad (2.33)$$

As the imaginary part of  $\chi^0$  vanishes for  $\omega \rightarrow 0$ , the real part carries all information. It is this response to a static magnetic field that we will be investigating in chapters 4-7 of this work. The two Heaviside functions in Eq. (2.33) make sure that only transitions from occupied to unoccupied bands result in non-vanishing contributions to  $\chi^0$  and the matrix elements weigh the transitions based on their transition probabilities. An important part of determining the structure of the susceptibility is given by the denominator containing the energy differences between an electron of band  $m$  at wave vector  $\mathbf{k}$  and a hole in

<sup>8</sup>The expression P(...) in Eq. (2.29) is an abbreviation for taking Cauchy's principal value.

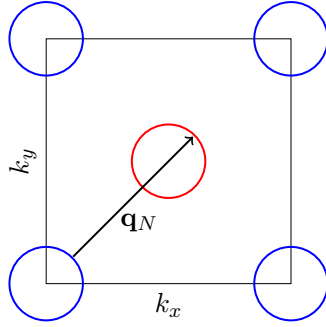


Figure 2.4.: Simplified picture of the Fermi surface of a two-band iron-based superconductor. The black square represents the 1BZ and we assume a hole pocket in the form of a cylinder in the center of the 1BZ (red). In the corners of the BZ we have electron pockets in the same shape as the hole one.

band  $n$  and wave vector  $\mathbf{k} + \mathbf{q}$ . Very similar or even equal energies will result in a big response of  $\chi^0$  at this wave vector  $\mathbf{q}$ , which indicates an instability towards a specific magnetic ordering of the electronic system. If the susceptibility has its maximum at  $\mathbf{q} = 0$ , for example, the system is most likely to develop a ferromagnetic order.

A keyword that is often dropped when susceptibilities are discussed in the context of magnetic orderings is *Fermi surface nesting*. This very popular concept, as discussed in the context of iron-based superconductors before, describes the nesting of two different Fermi surfaces with similar shape, when one is shifted by the nesting vector  $\mathbf{q}_N$ . In FeSCs the Fermi surface of most materials is composed of several sheets, whose shape is similar to each other and in an ideal case is also one- or two-dimensional. A simplified picture of such a Fermi surface is shown in Fig. 2.4, where we have hole sheets in the shape of cylinders in the center of the 1BZ (red) and electron sheets with the same shape in the corners (blue). By shifting the electron or hole pockets by the vector  $\mathbf{q}_N = (\pi, \pi)$  one can get the cylinders to overlap perfectly, called nesting. Such a surface nesting over large areas leads to a logarithmic divergence in  $\chi^0$ , indicating a huge response to a magnetic order with ordering vector  $\mathbf{q}_N$ .

### 2.3.1. Inter- and Intra-band Contributions and the Limit $|\mathbf{q}| \rightarrow 0$

In order to investigate the contributions to  $\chi^0$  more easily, it is convenient to split the transitions into intra- and interband contributions. Intraband processes occur within the same band, i.e.  $n = m$ , while interband ones happen between two different bands  $n \neq m$ . Due to the Heaviside functions in our formulas for  $\chi^0$ , which make sure that an electron is only excited from a (partly) filled band to a (partly) unoccupied band, intraband contributions can only appear in metals and not in semiconductors or insulators.

We now want to take a closer look at the limit  $|\mathbf{q}| \rightarrow 0$  of the static susceptibility function  $\chi^0(\mathbf{q})$ . We split the double sum over  $n$  and  $m$  into intra- and interband parts.

In the interband case, the matrix elements become

$$\lim_{|\mathbf{q}| \rightarrow 0} (\langle m, \mathbf{k} | e^{-i\mathbf{q}\cdot\mathbf{r}} | n, \mathbf{k} + \mathbf{q} \rangle) = \langle m, \mathbf{k} | n, \mathbf{k} \rangle = 0 .$$

In the case of intraband transitions the matrix elements become unity, but we encounter a problem with the energy denominator

$$\lim_{|\mathbf{q}| \rightarrow 0} \left( \frac{\Theta(\epsilon_F - \epsilon_{\mathbf{k}}^m) - \Theta(\epsilon_F - \epsilon_{\mathbf{k}+\mathbf{q}}^n)}{\epsilon_{\mathbf{k}}^m - \epsilon_{\mathbf{k}+\mathbf{q}}^n} \right) \rightarrow \frac{0}{0} .$$

One therefore has to be more careful in obtaining the limit and consider the behaviour of the whole integral. If  $\mathbf{q}$  is very small, a linear expansion for the energies is justified

$$\epsilon_{\mathbf{k}+\mathbf{q}}^m \approx \epsilon_{\mathbf{k}}^m + \nabla \epsilon_{\mathbf{k}}^m \cdot \mathbf{q} .$$

Additionally, the volume integral over  $d\mathbf{k}$  can be transformed into a surface integral over the Fermi surface and we have

$$\lim_{\mathbf{q} \rightarrow 0} \chi^0(\mathbf{q}) = -\frac{1}{2\pi^3} \sum_m \int_{\epsilon_{\mathbf{k}}^m = \epsilon_F} \frac{dS}{|\nabla \epsilon_{\mathbf{k}}^m|} . \quad (2.34)$$

The importance of Eq. (2.34) lies in the fact that this equation is, except for some prefactors, the same as the one for the *density of states* (DOS) at the Fermi energy  $N(\epsilon_F)$ , i.e.

$$\lim_{\mathbf{q} \rightarrow 0} \chi^0(\mathbf{q}) = -\frac{1}{\Omega_0} N(\epsilon_F) , \quad (2.35)$$

with  $\Omega_0$  being the volume of the 1BZ. The above expression is very useful for any numerical implementation of susceptibilities, as it offers a first and simple way to test the correctness and accuracy of the algorithms. In the course of this work we will refer to this test several times.

## 2.4. Going Beyond the Bare Susceptibility

### 2.4.1. Random Phase Approximation

The non-interacting *bare* susceptibility is the simplest expansion to the bare Coulomb potential. As was already discussed, it describes the reaction of the electron gas to the creation and annihilation of a non-interacting electron-hole pair, leading to the approximated effective potential of Eq. (2.14). The “natural” improvement to this approximation is to consider not only one, but an infinite sum of insertions to the bare Coulomb potential of the same type (see Fig. 2.5). In mathematical terms, Fig. 2.5 translates into

$$\begin{aligned} W(\mathbf{q}, \omega) &\approx v(\mathbf{q}) + v(\mathbf{q}) \chi^0(\mathbf{q}, \omega) v(\mathbf{q}) + v(\mathbf{q}) \chi^0(\mathbf{q}, \omega) v(\mathbf{q}) \chi^0(\mathbf{q}, \omega) v(\mathbf{q}) + \dots \\ &= v(\mathbf{q}) + v(\mathbf{q}) \{ \chi^0(\mathbf{q}, \omega) + \chi^0(\mathbf{q}, \omega) v(\mathbf{q}) \chi^0(\mathbf{q}, \omega) + \dots \} v(\mathbf{q}) \end{aligned} \quad (2.36)$$

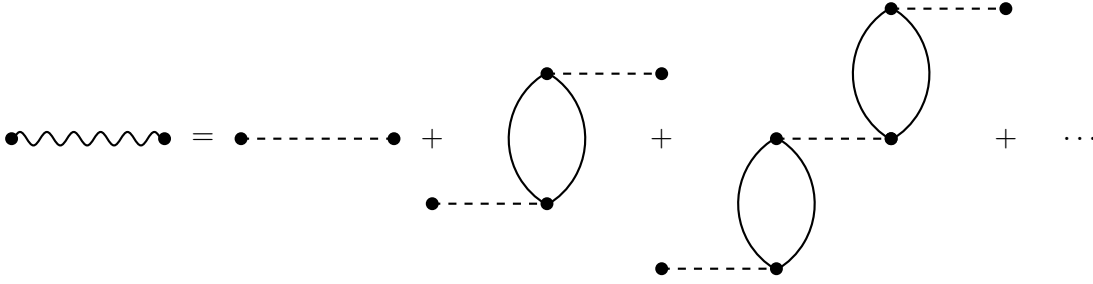


Figure 2.5.: Graphical representation of the terms considered in an RPA formulation of  $W$ .

In literature, this choice of diagrams is called *ring approximation* as well as *random phase approximation* (RPA). The term in curly brackets constitutes a more realistic approximation to the polarization function. To be more precise, the RPA includes long-range interactions between the otherwise noninteracting electron-hole excitations. The infinite sum is easily evaluated and can be written as the Dyson-like equation

$$\chi^{\text{RPA}} = \frac{\chi^0}{1 - v\chi^0}. \quad (2.37)$$

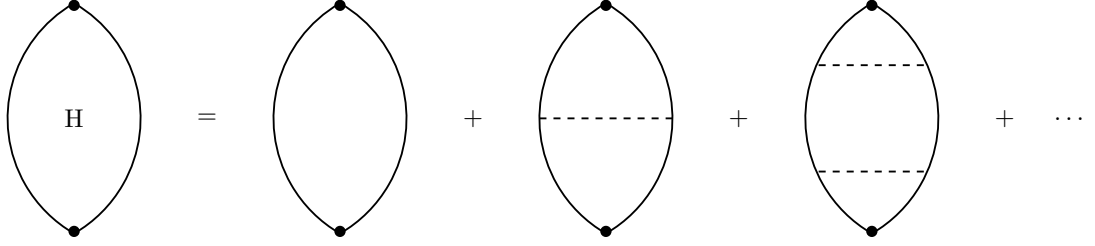
While  $\chi^0$  only allows to study single-particle excitations, the RPA enhancement permits to study *collective* excitations as well [103–105]. As can be seen from Eq. (2.8), the response of a charge system is of the same form as the perturbation, yet the amplitude of the reaction is determined by the polarization.<sup>9</sup> This means that if the perturbation is very weak, we can still get a big response from the system if the susceptibility is large. In the extreme case of a diverging  $\chi$  we would have modes of oscillations of the charge density in the system even for a vanishing perturbation.

For Eq. (2.37), there are two conceptually different excitations described by a diverging  $\chi^{\text{RPA}}$ . The singularities of  $\chi^0$  describe single-particle excitations of the system, while a vanishing denominator of  $\chi^{\text{RPA}}$  translates into collective excitations. The condition, when a collective excitation is present, can be easily split into two equations for the real and imaginary part of  $\Pi^0$

$$\begin{aligned} 1 - v(\mathbf{q})\text{Re}\chi^0(\mathbf{q}, \omega) &= 0 \\ \text{Im}\chi^0(\mathbf{q}, \omega) &= 0 \end{aligned} \quad (2.38)$$

The condition  $\text{Im}\chi^0 = 0$  is equivalent to imposing the same for the full  $\text{Im}\chi$  and has a direct physical meaning. The imaginary part of the susceptibility describes the dissipation taking place in the system. Therefore, in order to have a mode of a collective excitation propagating through the system without damping, the imaginary part of  $\chi$  has to vanish.

<sup>9</sup>The following discussion on collective excitations follows the theory presented in Refs. [103–105]


 Figure 2.6.: Graphical representation of the *vertex correction* to  $\chi^0$ .

Looking at the condition for the real part, we can distinguish between two extreme cases. If the interaction is short ranged,  $v(\mathbf{q} \rightarrow 0)$  tends towards a constant value  $U$ , representing the local interaction of a Hubbard model. In this case, Eq. (2.38) is satisfied for  $\text{Re}\chi^0 = 1/U$ . The additional approximation of small  $\omega$  leads, after some calculation, to the result that the frequency dependence of the dispersion relation is proportional to the wave vector  $\mathbf{q}$ , characteristic for a sound wave travelling through a system.

The other extreme case is that of long ranged interactions, as for example the Coulomb interaction. Here, the arising excitations are *plasmon* excitations. They are the quantum mechanical equivalent of classical plasma oscillations and describe oscillations of collective oscillations at optical frequencies.

Even the RPA, however, cannot account for all physical processes happening in such systems, as only the effects of creating electron-hole pairs on the interaction are considered. By doing so, this theory misses the interactions between the electron and the hole of a created electron-hole pair itself.

#### 2.4.2. Local Field Effects

An important development of the theory on polarization functions that goes beyond RPA has been introduced by Hubbard [106,107] and includes the so-called *vertex corrections* to the RPA. Hubbard enhanced the *bare* electron-hole polarization function by considering the infinite sum of diagrams depicted in Fig. 2.6. This *ladder expansion* of the electron-hole polarization describes the physical situation that the electron and hole of the same electron-hole pair interact with each other due to a Coulomb potential. Without giving the full derivation, the susceptibility in Hubbard's *local field correction* is given by [106, 107]

$$\chi^{\text{H}}(\mathbf{q}, \omega) = \frac{\chi^0(\mathbf{q}, \omega)}{1 - v(\mathbf{q}) [1 - G^{\text{H}}(\mathbf{q})] \chi^0(\mathbf{q}, \omega)}, \quad (2.39)$$

where we introduced the static local field factor

$$G^{\text{H}}(\mathbf{q}) \approx \frac{q^2}{2(q^2 + k_F^2)}. \quad (2.40)$$

The local field factor described in Eq. (2.40) is a good approximation for many problems. As the exact solution to  $G^H$  is complicated to evaluate, other approximations to this factors have been employed, as for example the *time-dependent local-density approximation* (TDLDA) [108, 109]. There, the field correction is taken as the functional derivative of the exchange-correlation potential  $V_{xc}$  with respect to the electron density  $n$

$$G^H(\mathbf{q}, \omega) = -v(\mathbf{q}) \int d^3x e^{-i\mathbf{q}\cdot\mathbf{x}} \frac{dV_{xc}(\mathbf{x})}{dn(\mathbf{x})}. \quad (2.41)$$

### 2.4.3. Including Interactions in the Case of Iron-Based Superconductors

In the theory of superconductors one is often interested in calculating  $T_c$  for a given model or material. In order to make any predictions on the superconducting temperature, one calculates the superconducting pairing function and tries to solve the eigenvalue equation for the superconducting state. At the heart of all these calculations are again the spin and charge susceptibilities.<sup>10</sup> The excitation physics of materials cannot be described by bare susceptibilities, as one has to consider correlations and interaction effects in some continuative theory. For example, in the FLEX approximation (see for example Ref. [37] and references therein) the interaction vertex  $\Gamma^{\text{FLEX}}$  is written like

$$\Gamma^{\text{FLEX}}(\mathbf{k}, \mathbf{k}', \omega) = \frac{3}{2}U^s\chi^s(\mathbf{k} - \mathbf{k}', \omega)U^s - \frac{1}{2}U^c\chi^c(\mathbf{k} - \mathbf{k}', \omega)U^c + \frac{1}{2}(U^s + U^c),$$

where the superscripts  $s$  and  $c$  stand for spin and charge, respectively.  $U^s$  ( $U^c$ ) is the spin (charge) interaction and  $\chi^s$  ( $\chi^c$ ) the resulting RPA spin (charge) susceptibility, given by Dyson's equation

$$\chi^s = \frac{\chi^0}{\mathbb{1} - U^s\chi^0} \quad \text{and} \quad \chi^c = \frac{\chi^0}{\mathbb{1} + U^c\chi^0}. \quad (2.42)$$

The pairing function, measuring the strength of the superconducting pairing, can in this approximation be written like

$$\Gamma_{i,j}(\mathbf{k}, \mathbf{k}') = \sum_{l_1, l_2, l_3, l_4} a_{\nu_i}^{l_2*}(\mathbf{k}) a_{\nu_i}^{l_3*}(-\mathbf{k}) \Gamma_{l_1, l_2, l_3, l_4}^{\text{FLEX}}(\mathbf{k}, \mathbf{k}') a_{\nu_j}^{l_1}(\mathbf{k}') a_{\nu_j}^{l_4}(-\mathbf{k}'). \quad (2.43)$$

In this notation we have assumed a multiorbital system, with  $l_i$  being orbital indices. The  $a_{\nu_i}^l(\mathbf{k})$  is the orbital matrix element  $\langle \nu_j, \mathbf{k} | l_1 \rangle$  of band  $\nu_i$  and orbital character  $l$  at the wave vector  $\mathbf{k}$ . As given in Eq. (2.43),  $\Gamma^{\text{FLEX}}(\mathbf{k}, \mathbf{k}', \omega)$  describes the irreducible particle-particle scattering of electrons with orbital indices  $l_1, l_4$  and momenta  $\mathbf{k}$  and  $-\mathbf{k}$  into electrons in orbitals  $l_2, l_3$  and momenta  $\mathbf{k}'$  and  $-\mathbf{k}'$ .  $\Gamma_{i,j}(\mathbf{k}, \mathbf{k}')$  then explains the effective pairing interaction for an electron pair scattering on the  $\nu_j$  Fermi surface with momenta and spins  $(\mathbf{k}' \uparrow, -\mathbf{k}' \downarrow)$  to a pair on the  $\nu_i$  Fermi surface and  $(\mathbf{k} \uparrow, -\mathbf{k} \downarrow)$ .

<sup>10</sup>The superconducting pairing is a function where an integral over the whole 1BZ has to be performed with a kernel proportional to  $\chi$ .

To get the leading eigenvalue  $\lambda_\alpha$  of the fully dressed (particle-particle) Bardeen-Cooper-Schrieffer (BCS) gap equation, one has to solve

$$-\frac{T}{N} \sum_{\mathbf{k}'} \Gamma^{PP}(\mathbf{k}, \mathbf{k}') G_\uparrow(\mathbf{k}') G_\downarrow(-\mathbf{k}') \phi_\alpha(\mathbf{k}') = \lambda_\alpha \phi_\alpha(\mathbf{k}) , \quad (2.44)$$

with  $G(\mathbf{k}, i\omega_n)$  being the fully dressed Green's function. The system becomes superconducting, when the leading eigenvalue approaches unity. As we are summing over all momenta  $\mathbf{k}'$  it is evident that  $\chi$  of the whole 1BZ enters the superconducting gap equation and that for superconductivity not only the maximal value of  $\chi$  has to be taken into account, as is the case for the spin (charge) instability of the system.

A proper evaluation of the dressed BCS gap function, however, would require at least including interactions along the lines of FLEX presented above, which is usually done in orbital picture. In an orbital basis, the interaction matrices  $U^s$  and  $U^c$  can be written down for FeSCs in a 5-orbital model quite easily. On the other hand, a big advantage of our implementation lies in the fact that we can calculate  $\chi^0$  without any projections to special orbitals and obtain the full bare susceptibility by summing over all bands, as we describe in Sec. 3 and following chapters. Since we don't want to lose this advantage, we need to transcribe the interaction matrices into band picture.<sup>11</sup>

Let  $U_{l_1, l_2, l_3, l_4} = \langle l_1, l_2 | U | l_3, l_4 \rangle$  be the interaction matrix in orbital space. Following Ref. [110] we have for the spin interaction

$$U_{l_1, l_2, l_3, l_4}^s = \begin{cases} \bar{U} & \text{for } l_1 = l_2 = l_3 = l_4 \\ \bar{J} & \text{for } l_1 = l_2 \neq l_3 = l_4 \\ \bar{U}' & \text{for } l_1 = l_3 \neq l_2 = l_4 \\ \bar{J}' & \text{for } l_1 = l_4 \neq l_2 = l_3 \end{cases} , \quad (2.45)$$

where  $\bar{U}$  is the intraorbital repulsion,  $\bar{U}'$  the interorbital interaction,  $\bar{J}$  the Hund's rule coupling and  $\bar{J}'$  the pair hopping energy. The charge interaction can be written similarly

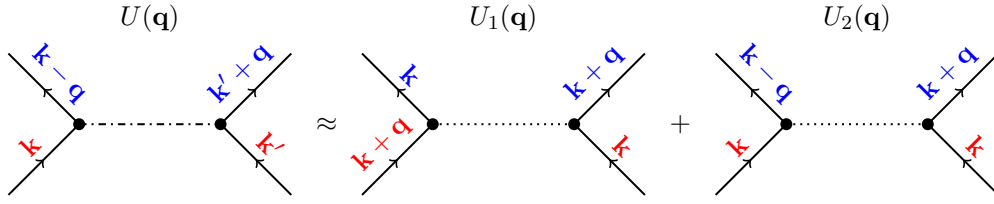
$$U_{l_1, l_2, l_3, l_4}^c = \begin{cases} \bar{U} & \text{for } l_1 = l_2 = l_3 = l_4 \\ 2\bar{U}' - \bar{J} & \text{for } l_1 = l_2 \neq l_3 = l_4 \\ 2\bar{J} - \bar{U}' & \text{for } l_1 = l_3 \neq l_2 = l_4 \\ \bar{J}' & \text{for } l_1 = l_4 \neq l_2 = l_3 \end{cases} . \quad (2.46)$$

In band space, the interaction matrix is a function of three momenta, say for example  $\mathbf{k}$ ,  $\mathbf{k}'$  and  $\mathbf{q}$ .<sup>12</sup> In order to use Dyson's equations as introduced in Eq. (2.44), we need to simplify the expressions and get rid of two momenta, so that  $U$  is just a function of  $\mathbf{q}$ ,

---

<sup>11</sup>The next paragraphs follow very closely a private communication with Ilya Eremin.

<sup>12</sup>The fourth momentum is fixed by the other three because of momentum conservation.


 Figure 2.7.: Diagrammatic depiction of the terms considered in  $U$ 

as is the susceptibility. Therefore, we start with the following ansatz:

$$\begin{aligned} U(\mathbf{q}) \begin{bmatrix} n & m \\ n' & m' \end{bmatrix} &= \sum_{\mathbf{k}, \mathbf{k}'} U_{\mathbf{k}, \mathbf{k}', \mathbf{q}} \begin{bmatrix} n & m \\ n' & m' \end{bmatrix} \\ &= \sum_{\mathbf{k}, \mathbf{k}'} \langle n, \mathbf{k} | \otimes \langle m, \mathbf{k}' | U | n', \mathbf{k}' - \mathbf{q} \rangle \otimes | m', \mathbf{k} + \mathbf{q} \rangle . \end{aligned}$$

Making the transcription to orbital space for the interaction matrix leads to

$$U(\mathbf{q}) \begin{bmatrix} n & m \\ n' & m' \end{bmatrix} = \sum_{\mathbf{k}, \mathbf{k}'} \sum_{l_1, l_2, l_3, l_4} U_{l_1, l_2, l_3, l_4} a_n^{l_1*}(\mathbf{k}) a_m^{l_2*}(\mathbf{k}') a_{n'}^{l_3}(\mathbf{k}' - \mathbf{q}) a_{m'}^{l_4}(\mathbf{k} + \mathbf{q}) ,$$

To proceed any further, we simplify this term further and split the double sum over wave vectors  $\mathbf{k}$  and  $\mathbf{k}'$  into an expression that applies for  $\mathbf{k} \approx \mathbf{k}'$  and one for  $\mathbf{k}' \approx \mathbf{k} + \mathbf{q}$ . The first choice takes into account that the biggest contributions to the interaction for the intra-band transitions will stem from matrix elements where  $\mathbf{k} \approx \mathbf{k}'$ . The inter-band transition, on the other hand, will have the biggest contributions when we connect bands where  $\mathbf{k}$  and  $\mathbf{k}'$  are separated by  $\mathbf{q}$ .

$$\begin{aligned} U(\mathbf{q}) \begin{bmatrix} n & m \\ n' & m' \end{bmatrix} &\approx \underbrace{\sum_{\mathbf{k}} \sum_{l_1, l_2, l_3, l_4} U_{l_1, l_2, l_3, l_4} a_n^{l_1*}(\mathbf{k}) a_m^{l_2*}(\mathbf{k} + \mathbf{q}) a_{n'}^{l_3}(\mathbf{k}) a_{m'}^{l_4}(\mathbf{k} + \mathbf{q})}_{\text{for } \mathbf{k}' \approx \mathbf{k} + \mathbf{q}} \\ &+ \underbrace{\sum_{\mathbf{k}} \sum_{l_1, l_2, l_3, l_4} U_{l_1, l_2, l_3, l_4} a_n^{l_1*}(\mathbf{k}) a_m^{l_2*}(\mathbf{k}) a_{n'}^{l_3}(\mathbf{k} - \mathbf{q}) a_{m'}^{l_4}(\mathbf{k} + \mathbf{q})}_{\text{for } \mathbf{k} \approx \mathbf{k}'} \quad (2.47) \end{aligned}$$

For the further discussion, it is convenient to write the two contributions to  $U(\mathbf{q})$  separately

$$U_1(\mathbf{q}) \begin{bmatrix} n & m \\ n' & m' \end{bmatrix} = \sum_{\mathbf{k}} \sum_{l_1, l_2, l_3, l_4} U_{l_1, l_2, l_3, l_4} a_n^{l_1*}(\mathbf{k}) a_m^{l_2*}(\mathbf{k} + \mathbf{q}) a_{n'}^{l_3}(\mathbf{k}) a_{m'}^{l_4}(\mathbf{k} + \mathbf{q}) \quad (2.48)$$

$$U_2(\mathbf{q}) \begin{bmatrix} n & m \\ n' & m' \end{bmatrix} = \sum_{\mathbf{k}} \sum_{l_1, l_2, l_3, l_4} U_{l_1, l_2, l_3, l_4} a_n^{l_1*}(\mathbf{k}) a_m^{l_2*}(\mathbf{k}) a_{n'}^{l_3}(\mathbf{k} - \mathbf{q}) a_{m'}^{l_4}(\mathbf{k} + \mathbf{q}) \quad (2.49)$$

A numerical evaluation of these terms is quite difficult, as all the matrix elements  $a_n^l(\mathbf{k})$  are complex numbers with a physical phase and an arbitrary one, due to the degree of freedom when solving an eigenvalue equation. Nevertheless, a calculation of Eq. (2.48) in the 1BZ is straightforward, as the matrix elements  $a_n^{l_1}$  and  $a_m^{l_2^\dagger}$  always appear in pairs in terms of the wave vector  $\mathbf{k}$ , which can therefore be combined to a real number, making the interpolation on the  $k$ -grid easy.

For  $U_2(\mathbf{q})$ , as given in Eq. (2.49), this is not possible, as the wave vector  $\mathbf{k}$  has to be combined with  $\mathbf{k} \pm \mathbf{q}$  and the product is still a complex number with an arbitrary complex phase. An extremely careful and elaborate way of interpolation has therefore to be chosen. As the main topic of this work is not on including interactions and correlations to susceptibility calculations, we are not going to discuss the explicit numerical implementation here in detail.

# Chapter 3.

## Numerical Implementation

### 3.1. Introduction

In this chapter we want to give a short review of common methods to calculate electronic susceptibilities and explain our implementation in detail. We will also elaborate on the advantages and disadvantages of our algorithms and show test examples to illustrate those points.

Electronic bandstructure methods exploit the translational symmetry of a crystal to block-diagonalize the Hamiltonian of the system with respect to the wave vector  $\mathbf{k}$ . In further consequence, all one-particle quantities one wants to calculate, like the density of states or in our case susceptibilities, can be obtained by an integration over the 1BZ. The accuracy of these calculations is therefore directly related to the amount of  $k$  points one chooses and the method of integration used.

Over the years, two kinds of algorithms have proven to be the most accurate and useful: the special-point scheme [111,112] and microcell schemes [113,114]. Special-point schemes represent the integral over the 1BZ as weighted sum over a set of specifically chosen  $k$  points [115] and are most applicable to insulators and semiconductors. They have the advantage of delivering very accurate results with a minimum number of  $k$  points, yet struggle with materials without an electron band gap.

The microcell algorithms divide the 1BZ in smaller cells, which can be in principle of *any* shape. The most widely used method is the tetrahedron method, where the 1BZ is partitioned into small tetrahedra. Compared to codes using higher-order polyeders, this method is conceptionally easier and due to linear interpolations of the electron energies and matrix elements within a tetrahedron, the corresponding integrals can be performed analytically [116,117]. Applied to insulators and semiconductor, however, tetrahedron methods needed a large amount of  $k$  points within the 1BZ to get reliable results. This disadvantage was remedied by Blöchl *et al.* [118], who introduced an improved technique that brought this method up to the level of special-point algorithms.

For the electronic susceptibilities calculated for our work, we chose to implement a tetrahedron scheme as it applicable to a wide variety of problems. We will in fact present two implementations. The first one was developed by Heinrich Sormann and uses the integration method by MacDonald, Vosko and Coleridge [119]. We will refer to this program from now on with MVC code. The second one was developed by the author of this work and is built on the foundations of the MVC code. It uses an algorithm, where only the region of 1BZ physically relevant for the  $\chi$  computation is tessellated into

tetrahedra and an analytic integration inside the tetrahedra along the lines of Ref. [116]. The actual integration formulas, however, have been reworked by Wolfgang von der Linden to obtain a more stable and accurate integration routine. In order not to disturb the flow of reading, these formulas are summarized in App. A.

### 3.2. Different Conventions for $\chi^0$

The numerical evaluation of electronic susceptibilities is by no means a trivial task, even with today's computer power. For the moment we will focus on the static bare susceptibility,<sup>1</sup> as presented in Sec. 2.3, and present again Eq. (2.33).

$$\chi^0(\mathbf{q}) = \sum_{n,m} \frac{d\mathbf{k}}{4\pi^3} \int_{\text{1BZ}} \frac{\Theta(\epsilon_F - \epsilon_{\mathbf{k}}^m) - \Theta(\epsilon_F - \epsilon_{\mathbf{k}+\mathbf{q}}^n)}{\epsilon_{\mathbf{k}}^m - \epsilon_{\mathbf{k}+\mathbf{q}}^n} \left| \langle m, \mathbf{k} | e^{-i(\mathbf{q}+\mathbf{K})\cdot\mathbf{r}} | n, \mathbf{k} + \mathbf{q} \rangle \right|^2. \quad (3.1)$$

Two things in particular cause major difficulties for any algorithm. Firstly, the numerical representation of the Heaviside functions, and secondly the treatment of singularities in the energy denominator. Using the substitution  $-\mathbf{k}' = \mathbf{k} + \mathbf{q}$  and the facts that  $\epsilon_{\mathbf{k}}^m = \epsilon_{-\mathbf{k}}^m$  and  $|m, \mathbf{k}\rangle = |m, -\mathbf{k}\rangle$ , we can express Eq. (3.1) differently

$$\chi^0(\mathbf{q}) = \sum_{n,m} \frac{d\mathbf{k}}{2\pi^3} \int_{\text{1BZ}} \frac{\Theta(\epsilon_F - \epsilon_{m,\mathbf{k}}^0) \Theta(\epsilon_{n,\mathbf{k}+\mathbf{q}}^0 - \epsilon_F)}{\epsilon_{\mathbf{k}}^m - \epsilon_{\mathbf{k}+\mathbf{q}}^n} \left| \langle m, \mathbf{k} | e^{-i(\mathbf{q}+\mathbf{K})\cdot\mathbf{r}} | n, \mathbf{k} + \mathbf{q} \rangle \right|^2. \quad (3.2)$$

Equations (3.1) and (3.2) offer two alternatives for the calculation of  $\chi^0(\mathbf{q})$ . In case of Eq. (3.2), one has to evaluate *one* integral over the 1BZ where - apart from the matrix element - the numerator of the integrand consists of a *product* of Heaviside functions. Eq. (3.1), on the other hand, requires the calculation of *two* independent integrals, where each includes only *one* Heaviside function. From the point of view that the numerical treatment of integrals over Heaviside functions is by no means trivial, Eq. (3.1) seems to be the more favourable candidate for a numerical evaluation. In fact, during the last decades a great number of authors dealing with the numerical determination of  $\chi^0(\mathbf{q})$  took this choice [33, 45, 76, 110, 120].

Despite its advantages, the evaluation of Eq. (3.1) has severe shortcomings, as the numerical results of two integrals of similar magnitude are subtracted. The situation is illustrated in Fig. 3.1, where we demonstrate the integration over the 1BZ for a very simple test case, namely a homogeneous electron gas in a 2D square lattice. The square represents the 1BZ and the central circle is the 'Fermi circle', which lies completely within the 1BZ, assuming that we only have one valence electron per unit cell. The union of the yellow and red regions in Fig. 3.1(a) represents the Fermi circle shifted by the wave vector  $\mathbf{q}$ . Note that all parts of this circle lying outside the 1BZ are projected back into the 1BZ. The evaluation of Eq. (3.1) requires an integration over the whole central Fermi

<sup>1</sup>The generalization to the dynamic susceptibility is straightforward and will be discussed in Sec. 3.3.2.

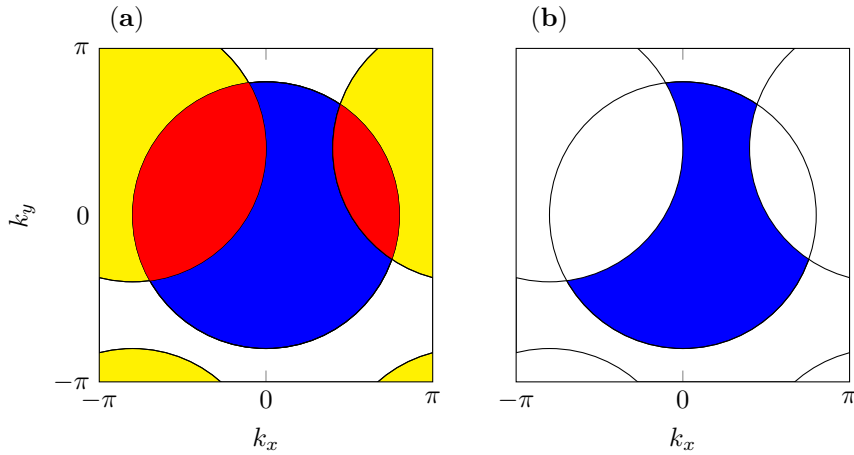


Figure 3.1.: Details of the integration over  $k$ -space for a homogeneous electron gas in a 2D square lattice according to (a): Eq. (3.1) and (b): Eq. (3.2).

circle (blue plus red regions). An analytical analysis of the integrals, however, shows that the red regions in Fig. 3.1(a) do not contribute at all. These *zero regions* increase with decreasing wave number  $|\mathbf{q}|$ . Using Eq. (3.1) for the determination of  $\chi^0$  therefore requires (especially for small values of  $|\mathbf{q}|$ ) many superfluous numerical integrations.

This numerically unpleasant situation is improved considerably if the susceptibility is calculated based on Eq. (3.2). Firstly, there is only *one* integral, and secondly (as illustrated in Fig. 3.1(b)), due to the *product* of the two Heaviside functions, which implies the condition

$$\Theta(\epsilon_F - \epsilon_{\mathbf{k}}^m) \Theta(\epsilon_{\mathbf{k}+\mathbf{q}}^n - \epsilon_F) = 1, \quad (3.3)$$

the red areas described above are explicitly avoided and the summation is restricted to tetrahedra in the blue region of Fig. 3.1(b). As Eq. (3.2) allows for a much more accurate evaluation of  $\chi^0$ , in particular for small values of  $|\mathbf{q}|$ , we have chosen this formula to be the basis of our susceptibility calculations. The implications of using the product of Heaviside functions instead of the difference for the actual numerical implementation will be discussed in more detail in the later part of Sec. 3.3.

### 3.3. Implementation of the Tetrahedron Method

As the MVC code represents the foundations of our newly developed program, we want to give a short summary of the way this algorithm works. By defining

$$F_m(\mathbf{k}) = \frac{1}{2\pi^3} \sum_n \frac{|\langle m, \mathbf{k} | e^{-i(\mathbf{q}+\mathbf{K})\cdot\mathbf{r}} | n, \mathbf{k} + \mathbf{q} \rangle|^2}{\epsilon_{\mathbf{k}}^m - \epsilon_{\mathbf{k}+\mathbf{q}}^n} \Theta(\epsilon_{\mathbf{k}+\mathbf{q}}^n - \epsilon_F), \quad (3.4)$$

we have the compact expression for the susceptibility

$$\chi^0(\mathbf{q}) = \sum_m \int_{1\text{BZ}} d\mathbf{k} \Theta(\epsilon_F - \epsilon_{\mathbf{k}}^m) F_m(\mathbf{k}) . \quad (3.5)$$

Due to the point group symmetry of the crystal, one can restrict the integral over  $k$  points to an irreducible wedge (IW) of the 1BZ. For the following we assume that the crystal's point group has  $T$  elements and we abbreviate the corresponding symmetry matrix of the  $t^{\text{th}}$  element by  $\alpha_t$ . Equation (3.5) then becomes

$$\chi^0(\mathbf{q}) = \sum_m \int_{\text{IW}} d\mathbf{k} \Theta(\epsilon_F - \epsilon_{\mathbf{k}}^m) \sum_t^T F_m(\alpha_t \mathbf{k}) , \quad (3.6)$$

where we made use of the fact that  $\epsilon_{\alpha_t \mathbf{k}}^m = \epsilon_{\mathbf{k}}^m$ . The integration technique as used in the MVC code follows in principle the suggestion by MacDonald *et al.* presented in Ref. [119]. We will therefore only sketch the most important parts needed to understand the working principle of such a program.

- At first, the IW is divided into a number of tetrahedrons, as shown in Fig. 3.2. These tetrahedrons don't have to be of the same size and orientation. In practice, however, it is most convenient to work with a regular mesh of  $k$  points, which constitute the vertex points of the tetrahedrons. For the further discussion we assume to have  $J$  tetrahedrons and the four vertices of the  $j^{\text{th}}$  tetrahedron are given by  $\mathbf{k}_s^j$  with  $s = 1, 2, \dots, 4$ .
- For each  $\mathbf{k}_s^j$ , the quantities  $\epsilon_{\mathbf{k}}^m$  and  $F_m(\alpha_t)$  have to be obtained. In our case, the Bloch energies  $\epsilon_{\mathbf{k}}^m$  and the corresponding wave functions  $\psi_{m,\mathbf{k}}(\mathbf{r})$  are calculated with the *full potential linearized augmented plane wave* (FP-LAPW) code WIEN2k [121, 122]. Then, the wave functions  $\psi_{m,\mathbf{k}}(\mathbf{r})$  are represented by a set of plane wave coefficients  $a_{m,\mathbf{k}}(\mathbf{K})$ , with  $\mathbf{K}$  being a reciprocal lattice vector, i.e.

$$\psi_{m,\mathbf{k}}(\mathbf{r}) = \frac{1}{\sqrt{\Omega}} \sum_{\mathbf{K}} a_{m,\mathbf{k}}(\mathbf{K}) e^{i(\mathbf{k}+\mathbf{K})\cdot\mathbf{r}} . \quad (3.7)$$

with  $\Omega$  being the normalization factor. In this representation, the matrix element in Eq. (3.4) can be written as

$$\langle m, \mathbf{k} | e^{-i(\mathbf{q}+\mathbf{K})\cdot\mathbf{r}} | n, \mathbf{k} + \mathbf{q} \rangle = \sum_{\mathbf{K}'} a_{m,\mathbf{k}}^*(\mathbf{K}') a_{n,\mathbf{k}+\mathbf{q}}(\mathbf{K}' - \mathbf{K}) . \quad (3.8)$$

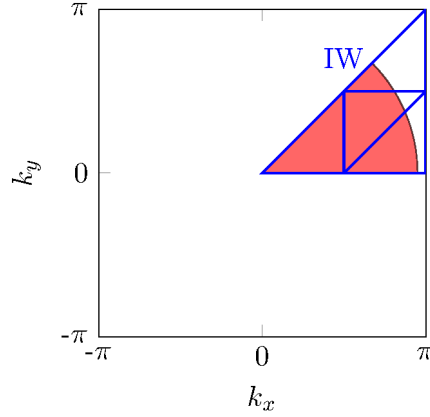


Figure 3.2.: Tetrahedron tessellation of the IW of a simple tetragonal lattice. For the sake of simplicity we use a 2-dimensional representation. The BZ is given by the axis limits and the area where this Heaviside function  $\Theta(\epsilon_F - \epsilon_{\mathbf{k}}^m)$  equals unity is indicated for the IW by the red shading. The Fermi radius has been chosen to be  $k_F(\mathbf{k}) = 1.9\frac{\pi}{a}$ .

- The simplest approximation of  $\chi^0$  is then given by calculating the weighted sum inside each tetrahedron and subsequently summing over all tetrahedrons

$$\chi^0(\mathbf{q}) \approx \sum_m \sum_{j=1}^J v_j \frac{1}{4} \sum_{s=1}^4 \tilde{F}_m(\mathbf{k}_s^j) \Theta(\epsilon_F - \epsilon_{\mathbf{k}}^m). \quad (3.9)$$

Here we used the abbreviation  $v_j$  for the volume of the  $j^{\text{th}}$  tetrahedron, and  $\tilde{F}_m(\mathbf{k}_s^j) = \sum_t F_m(\alpha_t \mathbf{k}_s^j)$ . In this formulation, the effect of the Fermi surface is simply taken into account by the fact that all  $k$  points lying outside the Fermi body are discarded. It is evident that such a simple approximation would require an enormous number of  $k$  points in order to give a result of reasonable accuracy.

- A much better evaluation of Eq. (3.6) is possible with the following approach. The intersection points of the Fermi surface (the border of the red area in Fig. 3.2) with the surfaces of the tetrahedrons are approximately calculated by means of *linear interpolation*. These *new points* define new tetrahedrons, which all fulfill  $\Theta(\epsilon_F - \epsilon_{\mathbf{k}}^m) = 1$ . The Bloch energies and the values of  $\tilde{F}_m(\mathbf{k}_s^j)$  are also linearly interpolated to the new  $k$  points. Staying in the notation of Ref. [119], Eq. (3.5) is written like

$$\chi^0(\mathbf{q}) \approx \sum_m \sum_{j=1}^J v_j n_j \frac{1}{4} \sum_{s=1}^4 I_s^j \tilde{F}_m(\mathbf{k}_s^j), \quad (3.10)$$

where  $n_j$  and  $I_s^j$  include the interpolation mentioned above.<sup>2</sup>

The Heaviside function  $\Theta(\epsilon_{\mathbf{k}+\mathbf{q}}^n - \epsilon_F)$  appearing in Eq. (3.4) assures that the scattered electron states lie *above* the Fermi level. In the MVC code, no interpolation is performed in order to better approximate this Heaviside function for the sake of a simpler and more compact algorithm. In the following we will show that our improved method, which eradicates this weakness,<sup>3</sup> yields results of much higher accuracy.

In order to numerically evaluate Eq. (3.2) properly, our new implementation accurately represents the second Heaviside function by a reshaping of the tetrahedron mesh. This process is performed in two steps.

- **Reshaping of the tetrahedra with respect to  $\Theta(\epsilon_F - \epsilon_{\mathbf{k}}^m)$**

Similar to the method of MacDonald *et al.* we classify every tetrahedron with respect to the first Heaviside function. If the energies  $\epsilon_{\mathbf{k}}^m$  at all tetrahedron vertices are smaller than  $\epsilon_F$ , the corresponding tetrahedron is considered *fully occupied* and added to the list of new tetrahedrons unchanged. A tetrahedron, where only some (but not all) vertex energies are smaller than the Fermi energy, is called *partly occupied*. We then calculate the intersection of the Fermi surface with this tetrahedron by linear interpolation of the energies  $\epsilon_{\mathbf{k}}^m$  and decompose the partly occupied tetrahedron into smaller, fully occupied ones, which are then added to our list of new tetrahedrons.<sup>4</sup> If all energies are smaller than the Fermi energy, the tetrahedron is considered *empty* and discarded. By employing such a procedure, as schematically drawn in Fig. 3.3(b), we end up with a list of tetrahedrons, which occupy only the area where  $\Theta(\epsilon_F - \epsilon_{\mathbf{k}}^m) = 1$ .

- **Reshaping of the tetrahedra with respect to  $\Theta(\epsilon_{\mathbf{k}+\mathbf{q}}^n - \epsilon_F)$**

Having obtained a list of fully occupied tetrahedrons with respect to the first Heaviside function, we proceed to numerically represent the second one with a similar algorithm. Every tetrahedron of our newly created list is subjected to the same classification, (i.e., fully occupied, partly occupied, empty) but now with respect to  $\Theta(\epsilon_{\mathbf{k}+\mathbf{q}}^n - \epsilon_F)$ . As this Heaviside function ensures that the electron is scattered into an available state above the Fermi energy, we now add the empty ones to our list unchanged. The fully occupied tetrahedrons are cast away and the partly occupied ones are broken up into smaller, completely empty tetrahedrons. In the end, we are left with a tetrahedron mesh that fills only the area where the product of both Heaviside functions equals unity (see Fig. 3.3(c), i.e., only the physical scattering processes from occupied to unoccupied electron states are taken into account.

<sup>2</sup>For a detailed derivation we refer the reader to Ref. [119].

<sup>3</sup>coupled with a better integration algorithm (see App. A)

<sup>4</sup>“We also tested a quadratic interpolation of the electron energies and transition matrix elements [118], which requires DFT calculation for additional  $k$  points. We found, however, that it is more advantageous to use these additional  $k$  points directly to create a tighter tetrahedral mesh and to use a linear interpolation.” C. Heil *et al.*, Ref. [80]

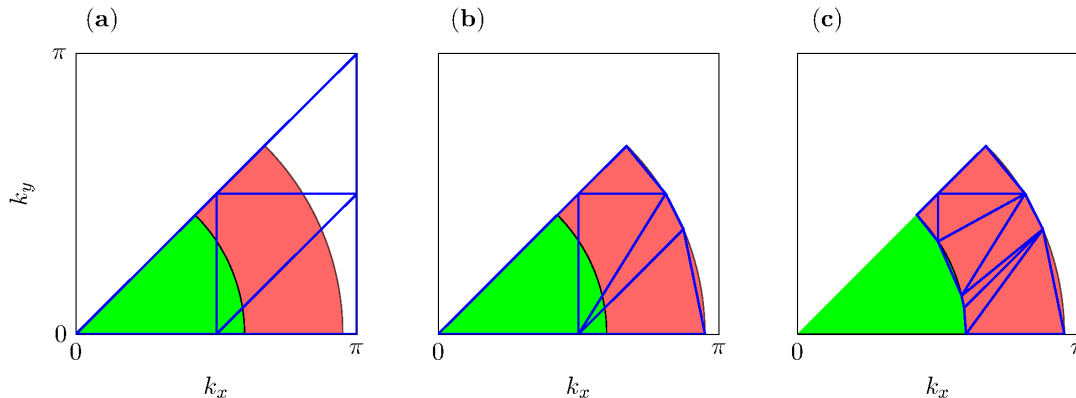


Figure 3.3.: Panel (a): Tetrahedron tessellation of the IW. The red area indicates where the product of Heaviside functions equals unity while the green shading represents the area, where only  $\Theta(\epsilon_F - \epsilon_{\mathbf{k}}^m)$  equals unity. Panel (b): First step of the tetrahedron reshaping to get fully occupied tetrahedrons where  $\epsilon_{\mathbf{k}}^m < \epsilon_F$ . Panel (c): Second step of the tetrahedron reshaping to represent only the area where Eq. (3.3) is fulfilled.

We want to note here that while the first *cutting* described has to be carried out only once for every electron band of the sum over  $m$ , the second *cut* has to be performed

1. for every  $\mathbf{q}$  vector,
2. for every electron band of the sum over  $n$ , and
3. for every point group element of the crystal.

The remaining task is the integration of  $1/(\epsilon_{\mathbf{k}}^m - \epsilon_{\mathbf{k}+\mathbf{q}}^n)$  for every tetrahedron. Integration formulas for such a problem can be found in many studies, as for example in Refs. [114, 116, 123]. However, we experienced problems with either the practical numerical implementation or the resulting accuracy with all of these formulations. A new set of integration formulas was therefore developed, in which all possible cases of singularities and indeterminacies have been carefully evaluated analytically. These formulas are presented in App. A.

### 3.3.1. Comparison of the MVC code and our new implementation

In the following, we want to give a short comparison of results obtained with the MVC code and our improved method. As test material we chose chromium, which is the classical example of a material exhibiting spin-density waves [124]. As our focus here is on the performance of the two implementations, we will review very briefly all the material's properties needed to understand the susceptibility results. A more elaborate

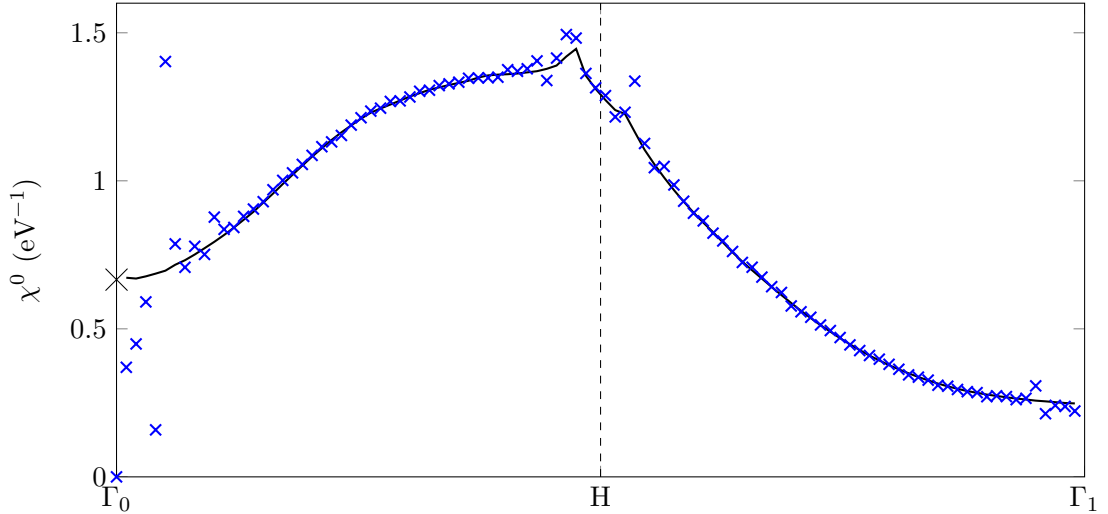


Figure 3.4.: Comparison of results obtained with the MVC code (blue crosses) and our newly developed algorithm (black line) for 506  $k$  points in the IW. The value of  $N(\epsilon_F)$  is indicated by a black cross at  $|\mathbf{q}| = 0$ .

discussion of the electronic structure and its implications for the susceptibility can be found in Sec. 4.

Chromium was the first material for which a spin density wave at a wave vector of  $|\mathbf{q}_{SDW}| \approx \frac{21}{22} \frac{2\pi}{a}$  in the (100) direction was found [125] and many susceptibility calculations were carried out to trace the origin of this SDW [124, 126, 127].<sup>5</sup> In all these studies, a peak in the bell-shaped susceptibility curve is found at  $|\mathbf{q}_{SDW}|$ , which can be connected to a nesting of the Fermi surfaces (see Sec. 4.3 of this work, published in Ref. [80]).

The results of a susceptibility calculation on chromium along the (100) direction can be seen in Fig. 3.4. There, we used 506  $k$  points to represent the IW and included 28 bands around the Fermi energy in our calculation in order to assure convergence with respect to the number of bands. The blue crosses mark the data points calculated with the MVC code and the black solid line is the susceptibility curve obtained by our improved algorithm.

A few observations are in order:

- As discussed in Sec. 2.3.1,  $\chi^0(\mathbf{q})$  has to approach the DOS at the Fermi energy  $N(\epsilon_F)$  for  $\mathbf{q} \rightarrow 0$ . This condition is only met with our new algorithm, which approaches this limit nicely. The MVC code, on the other hand, is unable to handle small values of  $|\mathbf{q}|$  and provides unreliable results for these wave vectors.
- Also at  $\mathbf{q}_{SDW}$ , the MVC code struggles to resolve the peak of the susceptibility. This most important feature of the susceptibility of Cr, however, is well resolved

<sup>5</sup>For a more detailed history of SDW in Cr see M. Bayer, Ph.D. thesis, TU Dresden, 2008.

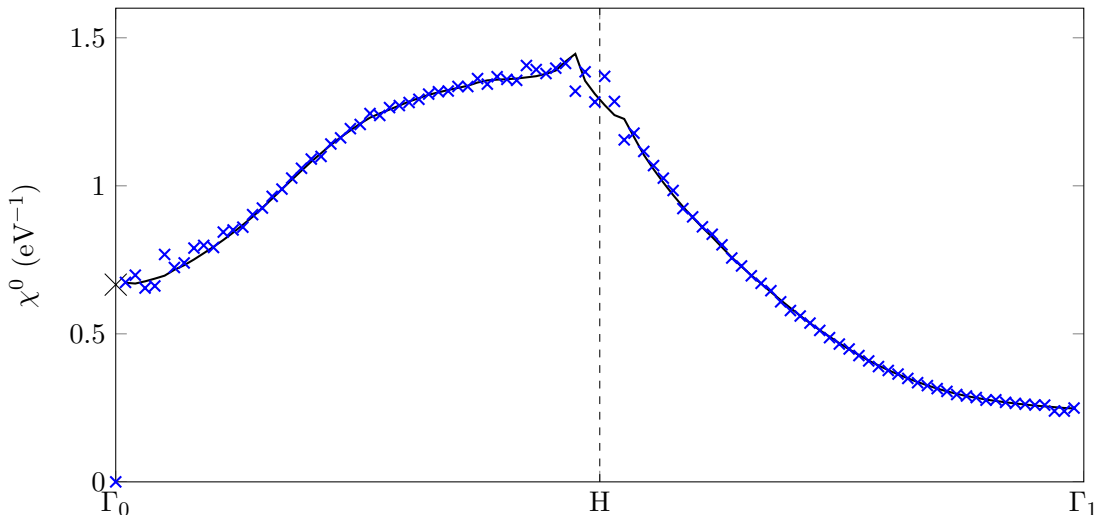


Figure 3.5.: Comparison of results obtained with the MVC code (blue crosses) and our newly developed algorithm (black line) for 1015  $k$  points in the IW. The value of  $N(\epsilon_F)$  is indicated by a black cross at  $|\mathbf{q}| = 0$ .

with our improved program, which yields  $|\mathbf{q}_{SDW}| \approx 0.95 \cdot \frac{2\pi}{a}$ , in accordance with other theoretical studies and experiments [124–126].

- A closer inspection of the blue crosses reveals that also in the region of larger  $|\mathbf{q}|$ , i.e. from  $0.3 \cdot \frac{2\pi}{a}$  onwards, small oscillations can be observed, which are directly related to the size of the tetrahedrons in the IW. The black solid line does not show this behavior.

A way to improve the accuracy of the MVC code is to consider a much tighter tetrahedron mesh. The result of such a calculation is shown in Fig. 3.5, where we used roughly twice as many  $k$  points in the IW as in Fig. 3.4.

The first, obvious observation is the fact that the results of the MVC code for  $|\mathbf{q}| \rightarrow 0$  have indeed improved considerably. While there are still large numerical errors in the blue data points left, the tendency towards  $N(\epsilon_F)$  is reproduced much better than before. The improvement close to the wave vector of the magnetic instability, however, is much smaller. Furthermore, there is no visible response at  $\mathbf{q}_{SDW}$ , which means that the MVC code is completely unable to describe this interesting response of Cr. Also a further doubling of the number of  $k$  points does not improve the situation for the MVC code significantly. The black curves in Figs. 3.4 and 3.5 representing the susceptibility calculated with our improved method, however, match each other nicely. This means that with our new implementation we obtain reliable results already for a small number of  $k$  points.

The situation is even worse in the CMA. In this very simple approximation, often employed to measure Fermi surface nesting (see also Ref. [80]), the matrix elements are

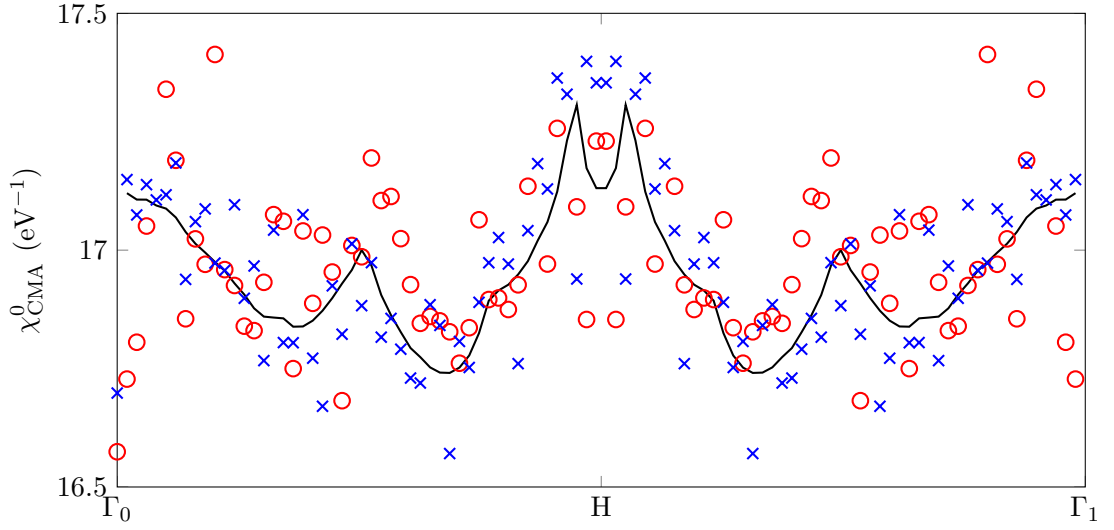


Figure 3.6.: Comparison of results obtained in the CMA with our newly developed algorithm (black line) with 506  $k$  points in the IW and the MVC code for 506 (red circles) and 1015 (blue crosses)  $k$  points.

all set to unity. While the susceptibilities obtained within the CMA are in general very different to properly calculated susceptibility curves, they do show a strong response at wave vectors where parts of the Fermi surface overlap. Results for calculations in the CMA are presented in Fig. 3.6, where the black solid line stands for data obtained with our new algorithm and the red circles and blue crosses represent data points from the MVC code for 506 and 1015  $k$  points, respectively. A discussion on the merits of the CMA will follow in later chapters of this work (Sec. 4), here we only want to note that the MVC code provides completely useless data and the situation does also not improve when more  $k$  points are included.

This leaves us with the conclusion that the MVC code cannot be used in the CMA and in order to get reliable results for the proper bare susceptibility with this technique, one has to consider a huge number of  $k$  points in the IW. While this might be possible for a simple compound such as chromium, it is completely impractical for more complicated compounds such as  $\text{LiFeO}_2\text{Fe}_2\text{Se}_2$  (see Sec. 7). Our new implementation of the tetrahedron method, however, delivers very accurate results already for very few  $k$  points in the IW. This in turn allows us to tackle more expensive calculations such as calculating the dynamic bare susceptibility, as discussed in Sec. 3.3.2. It also presents a firm foundation for calculations beyond the bare susceptibility.

### 3.3.2. Calculation of the dynamic susceptibility

The calculation of the dynamic susceptibility is of particular interest, as this allows the determination of excitation energies and, when going beyond  $\chi^0$ , dispersion relations of

collective modes. It is convenient for the following discussion to split  $\chi^0(\mathbf{q}, \omega)$  into its real and imaginary parts, as done in Eq. (2.30). For these formulas, one can also find expressions where the product of Heaviside functions appears instead of their difference. In analogy to Sec. 3.2. We therefore have

$$\begin{aligned} \text{Re}\chi^0(\mathbf{q}, \omega) &= \sum_{n,m} \int_{1\text{BZ}} \frac{d\mathbf{k}}{4\pi^3} \Theta(\epsilon_F - \epsilon_{\mathbf{k}}^m) \Theta(\epsilon_{\mathbf{k}+\mathbf{q}}^n - \epsilon_F) |\langle m, \mathbf{k} | e^{-i\mathbf{q}\cdot\mathbf{r}} | n, \mathbf{k} + \mathbf{q} \rangle|^2 \\ &\quad \times \left( \frac{1}{\epsilon_{\mathbf{k}}^m - \epsilon_{\mathbf{k}+\mathbf{q}}^n + \hbar\omega} + \frac{1}{\epsilon_{\mathbf{k}}^m - \epsilon_{\mathbf{k}+\mathbf{q}}^n - \hbar\omega} \right), \end{aligned} \quad (3.11)$$

and

$$\begin{aligned} \text{Im}\chi^0(\mathbf{q}, \omega) &= - \sum_{n,m} \int_{1\text{BZ}} \frac{d\mathbf{k}}{4\pi^2} \Theta(\epsilon_F - \epsilon_{\mathbf{k}}^m) \Theta(\epsilon_{\mathbf{k}+\mathbf{q}}^n - \epsilon_F) |\langle m, \mathbf{k} | e^{-i\mathbf{q}\cdot\mathbf{r}} | n, \mathbf{k} + \mathbf{q} \rangle|^2 \\ &\quad \times \delta(\hbar\omega + \epsilon_{\mathbf{k}}^m - \epsilon_{\mathbf{k}+\mathbf{q}}^n). \end{aligned} \quad (3.12)$$

From a numerical point of view it is much more convenient to calculate the imaginary part of the susceptibility and then use a Kramers-Kronig transformation to obtain the real part than to calculate the real part directly. If we consider for a moment the matrix elements to be constant over the volume of the tetrahedron, the integration over the tetrahedron volume  $V$  reduces to

$$I = \int_V d\mathbf{k} \delta(\hbar\omega + \epsilon_{\mathbf{k}} - \epsilon_{\mathbf{k}+\mathbf{q}}). \quad (3.13)$$

This is an equation often encountered in numerics, as for example in DOS calculations. By a linear interpolation of the energies and a Taylor expansion up to first order, Eq. (3.13) can be rewritten

$$I = \int_V d\mathbf{k} \frac{\delta(\hbar\omega - \epsilon_{\mathbf{k}})}{|\nabla_{\mathbf{k}}(\Delta\epsilon)|},$$

where  $\Delta\epsilon = \epsilon_{\mathbf{k}} - \epsilon_{\mathbf{k}+\mathbf{q}}$ . With that, the solution to Eq. (3.13) can be simply written as the area of the constant energy surface  $S$  with energy  $\hbar\omega$ , divided by the gradient of the energy difference

$$I = \frac{S}{|\nabla_{\mathbf{k}}(\Delta\epsilon)|}. \quad (3.14)$$

A schematic representation is given in Fig. 3.7, which shows a tetrahedron cut by the constant energy surface  $S$ . The inclusion of matrix elements in this integration is straightforward by performing a linear interpolation for those as well.

To calculate  $\chi^0(\mathbf{q}, \omega)$ , our algorithm therefore executes the following steps

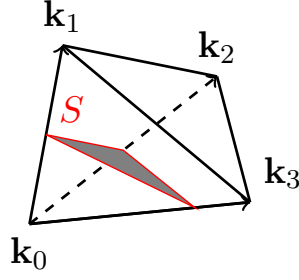


Figure 3.7.: Schematic drawing of a single tetrahedron with its corner coordinates  $\mathbf{k}_i$  to illustrate the integration of Eq. (3.13). The shaded area  $S$  is the constant energy surface inside the tetrahedron with  $\Delta\epsilon = \hbar\omega$ .

- Reshaping of the tetrahedron mesh with respect to  $\Theta(\epsilon_F - \epsilon_{\mathbf{k}}^m)\Theta(\epsilon_{\mathbf{k}+\mathbf{q}}^n - \epsilon_F)$ . As before, this leaves us with only the physically relevant volume of the IW.
- For every value of  $\omega$  the integral

$$\int_V d\mathbf{k} \left| \langle m, \mathbf{k} | e^{-i(\mathbf{q}+\mathbf{K})\cdot\mathbf{r}} | n, \mathbf{k} + \mathbf{q} \rangle \right|^2 \cdot \delta(\hbar\omega + \epsilon_{\mathbf{k}} - \epsilon_{\mathbf{k}+\mathbf{q}}) \quad (3.15)$$

has to be solved for every tetrahedron which is cut by the constant energy surface given by  $\omega$ . This process has to be repeated for (i) every  $\mathbf{q}$  vector, (ii) every electron band of the sum over  $n$ , and (iii) for every point group element, as already discussed in the context of the static case.

- Calculating the real part via a Kramers-Kronig transformation as described in Eq. (2.32). Special attention has to be paid to the fact that in order to perform this transformation properly, the chosen frequency interval needs to be large enough, i.e.,  $\text{Im}\chi^0(\mathbf{q}, \omega)$  has to vanish for all  $\omega \geq \omega_{\text{max}}$ , where  $\omega_{\text{max}}$  is the biggest frequency considered in the transformation.

**Part II.**

**Results**



## Chapter 4.

# Accurate bare susceptibilities from full-potential *ab initio* calculations

C. Heil , H. Sormann, L. Boeri, M. Aichhorn, and W. von der Linden

Physical Review B **90**, 115143 (2014)

Copyright 2014 by the American Physical Society.

### Abstract

Electronic susceptibilities are a very popular tool to study electronic and magnetic properties of materials, both in experiment and theory. Unfortunately, the numerical evaluation of even the bare susceptibility, which depends on the computation of matrix elements and sums over energy bands, is very work intensive and therefore various approximations have been introduced to speed up such calculations. We present a reliable and efficient implementation of the tetrahedron method which allows us to accurately calculate both static and dynamic bare susceptibilities, based on full-potential density functional theory (DFT) calculations. In the light of the exact results we assess the effects of replacing the matrix elements by a constant and the impact of truncating the sum over the energy bands. Results will be given for representative and topical materials such as Cr, a classical transition metal, as well as the iron-based superconductor FeSe.

### 4.1. Introduction

The susceptibility  $\chi$  both of charge and spin is a favoured quantity of theorists as it reveals interesting details of the excitation spectrum of the considered system and can directly be compared with experimental results [128,129]. There is a long list of materials for which susceptibilities have given important insights to unravel the underlying physics. In particular, for the iron-based superconductors [1, 7] (FeSCs), susceptibilities play a crucial role in the discussion of the origin of superconductivity.

Many undoped FeSCs have an antiferromagnetic ground state, whose magnetic ordering vector matches the Fermi surface nesting vector [7]. Since the very beginning of the field, this has been considered a strong indication of spin-fluctuation mediated superconductivity and many theories have been proposed to explain superconductivity based on susceptibility calculations [18,32,33,45,52,79,130–132]. In these weak-coupling

approaches, the full electronic structure is usually reduced to an effective model using analytical approximations for the relevant bands (*ab initio* downfolding or projection techniques) and the many-body interactions responsible for superconductivity, magnetism and other instabilities are treated with more and more sophisticated methods, such as random-phase approximation (RPA), fluctuation exchange approximation, functional renormalization group, etc. [32, 131, 132]. Only very recently, a first-principles scheme for an *ab initio* treatment of spin fluctuations has been proposed [52]. Although they don't allow quantitative predictions of critical temperatures and energy scales, these calculations have provided very important insights into issues such as the symmetry of the order parameter, trends of superconducting critical temperatures, competition of different instabilities, and so on.

These studies have shown that even small changes in the electronic structure can have a large impact on superconductivity and magnetism. This implies that the influence of the approximations employed for the calculations of the non interacting system is a serious issue. The non interacting susceptibility, representing the basis of RPA and of self-consistent DFT for spin fluctuations, is a particularly critical quantity: the results are very sensitive to small details of the electronic structure, therefore very accurate electronic structures and  $k$ -space integration methods are needed; matrix elements are easy to compute in a plane wave basis, but converge very slowly with basis size; in cases where bare susceptibilities are used as input for many-body calculations, the number of bands is also a serious issue.

A common procedure in this case is to downfold the full electronic structure onto an effective low-energy model, which reproduces the band structure in the vicinity of the Fermi level. This truncation can have severe effects on the susceptibility, since the convergence with the number of bands is very slow. In fact, although susceptibility calculations have been performed for a long time and many different algorithms have been proposed for the numerical evaluation [116, 119, 123, 129], the number of fully first-principles calculations of susceptibilities is scarce [47, 52, 79, 120, 133].

In this paper we present a method that enables one to avoid these approximations and yields reliable results for the static and dynamic bare susceptibility, based on full-potential DFT calculations [121] of the electronic structure and tetrahedron integration [113]. We introduce a non standard tetrahedron method that explicitly takes only the non vanishing contributions of the Brillouin zone into account and significantly reduces the number of required  $k$  points. The accuracy of the presented approach is controlled by the number of  $k$  points in the first Brillouin zone, the number of reciprocal lattice vectors  $G$  used in the expansion of the LDA wave functions in plane waves, and the number of electronic bands entering the susceptibility formula. We demonstrate that converged results can be reached with acceptable computational effort.

Based on exact results obtained by this method, we scrutinize the approximation where all matrix elements are replaced by unity - henceforth referred to as *constant matrix element approximation* (CMA) [116, 117, 119, 123]. The CMA, which was very often used in the early days of susceptibility calculations, is at the heart of many qualitative arguments on Fermi surface nesting, which have been revived in recent years to explain different phenomena, ranging from charge and spin density waves (SDWs) to supercon-

ductivity [33, 134]. We show that, in fact, CMA can strongly affect the susceptibility. Moreover, we discuss the effects of downfolding the full band structure to an effective low-energy model.

We would like to remark that the general purpose of this work is to provide a scheme to compute reliable bare susceptibilities. The inclusion of many-body effects, which would allow a direct comparison to experiment, is beyond the scope of this paper.

This paper is organized as follows. In Sec. 4.2 we introduce expressions for the bare susceptibility  $\chi^0$  and the method and algorithm we propose to evaluate them with. In Sec. 4.3 we study the impact of CMA on the static bare susceptibility  $\chi^0$  of two representative examples and we also discuss the error induced by truncating the number of electronic bands. In Sec. 4.4 we extend the analysis to dynamic susceptibilities and our findings are summarized in Sec. 4.5.

## 4.2. Method

For a system of Bloch electrons - taking into account only the diagonal elements of the  $\chi^0$  matrix - the real and imaginary parts of the non interacting (*bare*) dynamic susceptibility [92] read

$$\begin{aligned} \text{Re}\chi^0(\mathbf{q}, \omega) &= \sum_{n,m} \int_{\text{1BZ}} \frac{d\mathbf{k}}{4\pi^3} \Theta(\epsilon_F - \epsilon_{\mathbf{k}}^m) \Theta(\epsilon_{\mathbf{k}+\mathbf{q}}^n - \epsilon_F) \\ &\quad \times |\langle m, \mathbf{k} | e^{-i\mathbf{q}\cdot\mathbf{r}} | n, \mathbf{k} + \mathbf{q} \rangle|^2 \left( \frac{1}{\epsilon_{\mathbf{k}}^m - \epsilon_{\mathbf{k}+\mathbf{q}}^n + \hbar\omega} + \frac{1}{\epsilon_{\mathbf{k}}^m - \epsilon_{\mathbf{k}+\mathbf{q}}^n - \hbar\omega} \right) \end{aligned} \quad (4.1)$$

$$\begin{aligned} \text{Im}\chi^0(\mathbf{q}, \omega) &= - \sum_{n,m} \int_{\text{1BZ}} \frac{d\mathbf{k}}{4\pi^2} \Theta(\epsilon_F - \epsilon_{\mathbf{k}}^m) \Theta(\epsilon_{\mathbf{k}+\mathbf{q}}^n - \epsilon_F) \\ &\quad \times |\langle m, \mathbf{k} | e^{-i\mathbf{q}\cdot\mathbf{r}} | n, \mathbf{k} + \mathbf{q} \rangle|^2 \delta(\hbar\omega + \epsilon_{\mathbf{k}}^m - \epsilon_{\mathbf{k}+\mathbf{q}}^n), \end{aligned} \quad (4.2)$$

where Eq. (4.2) holds for  $\omega \geq 0$ . For negative values of  $\omega$ , the imaginary part is taken from the relation

$$\text{Im}\chi^0(\mathbf{q}, -\omega) = -\text{Im}\chi^0(\mathbf{q}, \omega). \quad (4.3)$$

The real and imaginary parts of  $\chi^0$  are connected via the Kramers-Kronig transformation.  $\mathbf{q}$  is a vector of the extended wave-vector space and  $\mathbf{k}$  represents vectors of the first Brillouin zone (1BZ).  $n$  and  $m$  denote electron band indices,  $\epsilon_F$  is the Fermi energy, and  $\epsilon_{\mathbf{k}}^m$  stands for the energy dispersion of the  $m$ th band. The product of Heaviside functions in the numerator of the integrand ensures that only transitions from occupied to unoccupied electron states contribute to the integral. A similar expression for  $\chi^0$  can be derived where the product of Heaviside functions is replaced by their difference  $\Theta(\epsilon_F - \epsilon_{\mathbf{k}}^m) - \Theta(\epsilon_F - \epsilon_{\mathbf{k}+\mathbf{q}}^n)$ . While the latter is simpler from a geometrical point of view, it has the disadvantage that many contributions of the two terms cancel each other, an effect which becomes increasingly severe with decreasing  $|\mathbf{q}|$ .

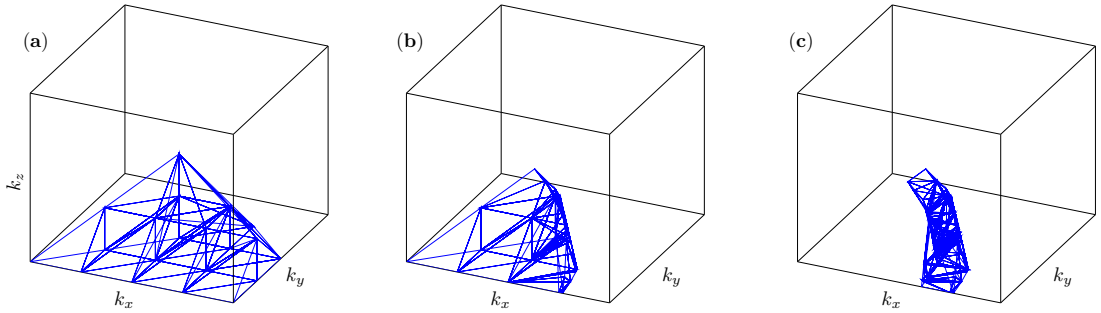


Figure 4.1.: (Color online) (a) Tetrahedral mesh of the irreducible wedge of an fcc lattice. The other panels show the mesh after the first (b) and after the second (c) cut with the Fermi surface (see text). For the sake of simplicity we use a parabolic dispersion  $\epsilon(\mathbf{k}) = |\mathbf{k}|^2$ ;  $\mathbf{q} = (0.15, 0, 0)$  and  $k_F = 0.77$ .

We therefore chose Eqs. (4.1) and (4.2) to be the basis of all our susceptibility calculations. In Sec. 4.3, which is dedicated to the *static* bare susceptibility, all results are obtained by an evaluation of Eq. (4.1) for  $\omega = 0$ , in which case the imaginary part vanishes. However, if one wishes to study the *dynamics* of  $\chi^0$  (as, e.g., in Sec. 4.4 of this paper), one is usually interested in the  $\omega$  dependence of both the real and the imaginary part of  $\chi^0$ . In this case, one normally computes only the imaginary part  $\text{Im}\chi^0(\mathbf{q}, \omega)$  because its numerical evaluation is significantly less challenging than a direct calculation of  $\text{Re}\chi^0(\mathbf{q}, \omega)$  and the corresponding real part can then be easily obtained by the Kramers-Kronig relation, provided that sufficiently large values of  $\omega$  have been considered.

Both expressions (4.1) and (4.2) require a  $k$ -space integration over the irreducible wedge (IW) of the 1BZ. For a numerical evaluation of such integrals, different algorithms have been proposed in literature. Smearing methods are not appropriate for susceptibility calculations, and the most commonly used implementations are *random sampling* [52, 79] or tetrahedron methods [113, 114, 116–118, 123].

In the following we present an implementation of the tetrahedron method that differs from other algorithms in some key aspects, which will be described later. The starting point, however, is the same as in all other implementations, i.e., the IW is decomposed into a number of tetrahedra as depicted in Fig. 4.1(a) and described, for example, in Refs. [114, 123]. The Bloch energies  $\epsilon_{\mathbf{k}}^m$  and the corresponding wave functions  $\psi_{m,\mathbf{k}}(\mathbf{r})$  for  $k$  points at the corners of the tetrahedra are determined by using electron band structure codes, in our case the *full potential linearized augmented plane wave* (FP-LAPW) code WIEN2k [121, 122]. Numerically, each wave function  $\psi_{m,\mathbf{k}}(\mathbf{r})$  is represented by a set of plane wave coefficients  $a_{m,\mathbf{k}}(\mathbf{K})$ , with  $\mathbf{K}$  being the reciprocal lattice vector. Based on this system of input data, the energies  $\epsilon_{\mathbf{k}+\mathbf{q}}^n$  and coefficients  $a_{n,\mathbf{k}+\mathbf{q}}(\mathbf{K})$ , which usually belong to  $k$  points *not* contained in the tetrahedra set, are approximated by linear interpolation. This means that in our calculations both the electron energies and the matrix elements in Eqs. (4.1) and (4.2) are numerically treated *on equal footing*.

The most demanding aspect of the numerical evaluation of the integrals (4.1) and (4.2) comes from the product of Heaviside functions  $\Theta(\epsilon_F - \epsilon_{\mathbf{k}}^m)\Theta(\epsilon_{\mathbf{k}+\mathbf{q}}^n - \epsilon_F)$ : first, the step function  $\Theta(\epsilon_F - \epsilon_{\mathbf{k}}^m)$  reduces the integration within the IW to *initial* electron states  $\epsilon_{\mathbf{k}}^m$  lying *inside* the Fermi surface (FS). The numerical realization of such a reduction is quite popular in the literature; some authors (see, e.g., Charlesworth and Yeung [117]) call this a *geometric interpretation* of the tetrahedra to emphasize that their occupation depends on their spatial position within the IW: a tetrahedron is said to be either empty, fully occupied, or partially occupied, if it is either entirely outside, inside, or cut by the Fermi surface. Empty tetrahedra are removed as they do not contribute to the integral and fully occupied ones remain unchanged. Since the integration over fully occupied tetrahedra is less time consuming and more reliable than over partially occupied ones, the latter are further decomposed into a finer set of completely occupied tetrahedra. This procedure, schematically shown in Fig. 4.1(a) and Fig. 4.1(b), is described in detail by, e.g., MacDonald *et al.* [119] and Rath and Freeman [116].

The key aspect of our implementation is that this process of cutting the tetrahedra to carve out the regions where the Heaviside function equals unity is consequently repeated also for  $\Theta(\epsilon_{\mathbf{k}+\mathbf{q}}^n - \epsilon_F)$ . In this way, the *final* tetrahedra are restricted to the region of the IW, where the condition

$$\Theta(\epsilon_F - \epsilon_{\mathbf{k}}^m)\Theta(\epsilon_{\mathbf{k}+\mathbf{q}}^n - \epsilon_F) = 1 \quad (4.4)$$

is fulfilled.<sup>1</sup> The corresponding (second) reformulation of the set of tetrahedra in the IW is graphically demonstrated by Fig. 4.1(b)  $\rightarrow$  Fig. 4.1(c). While the first step from (a) to (b) has to be performed only once for every electron band (of the sum over  $m$ ), the second step has to be repeated (i) for every value of the  $\mathbf{q}$  vector, (ii) for every electron band of the sum over  $n$ , and (iii) for every point group element of the crystal. The main benefit of this approach is that a lot of numerical issues encountered when integrating over tetrahedra, which do not fulfill condition (4.4) but only  $\Theta(\epsilon_F - \epsilon_{\mathbf{k}}^m) = 1$ , can be avoided and a simpler set of integration formulas can be used. Besides the simplified numerical integration, the number of  $k$  points in the IW can be significantly reduced. For example, the results for chromium, which we are going to discuss in Sec. 4.3, were obtained by using approximately 500  $k$  points in the IW. To achieve the same accuracy without the second carving of the 1BZ, we would have needed to consider more than 2000  $k$  points.

Finally, we also tested a quadratic interpolation of the electron energies and transition matrix elements [118], which requires DFT calculations for additional  $k$  points. We found, however, that it is more advantageous to use these additional  $k$  points directly to create a tighter tetrahedral mesh and to use a linear interpolation.

---

<sup>1</sup> $\Theta(\epsilon_{\mathbf{k}+\mathbf{q}}^n - \epsilon_F)$  reduces the integration within the IW to *final* electron states  $\epsilon_{\mathbf{k}+\mathbf{q}}^n$  lying *outside* the Fermi surface.

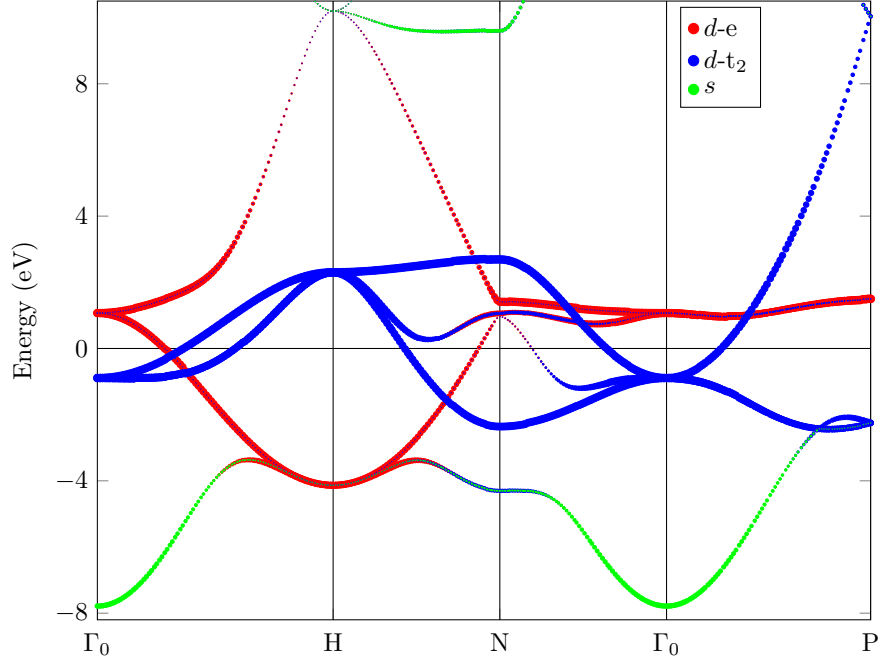


Figure 4.2.: (Color online) LDA bandstructure of Cr, decorated with partial characters:  $s$  (green),  $d-t_2$  (blue), and  $d-e$  (red). The coordinates of the high-symmetry points are  $\Gamma_0=(0,0,0)$ ,  $H=(0,1,0)$ ,  $N=(\frac{1}{2},\frac{1}{2},0)$ , and  $P=(\frac{1}{2},\frac{1}{2},\frac{1}{2})$ , all in units of  $\frac{2\pi}{a}$  with  $a$  being the lattice constant.

### 4.3. Static Bare Susceptibility

The CMA is the simplest approximation to avoid the cumbersome evaluation of the matrix elements entering the bare susceptibility formula. This approximation has been used to interpret susceptibility data and SDW order in many transition metals, such as Pd and Cr. The concept of Fermi surface nesting, which derives from these early CMA calculations, is still quite popular nowadays in several materials, such as FeSCs and layered metal dichalcogenides. We will demonstrate that although CMA in some cases may lead to reasonable results, it fails in other cases. In the light of this unpredictability it is advisable to include matrix elements in all static susceptibility calculations and even more so in the dynamical ones.

In order to calculate the matrix elements  $\langle m, \mathbf{k} | e^{-i\mathbf{q}\cdot\mathbf{r}} | n, \mathbf{k} + \mathbf{q} \rangle$  correctly we expand the LAPW [121] eigenvectors  $|m, \mathbf{k}\rangle$  in a plane wave basis. We carefully checked that our results are converged with respect to the number of plane waves (typically around 4000).

We start our discussion with the  $3d$  transition metal chromium (Cr), a classical SDW material [125], for which different approximations for susceptibilities have been proposed. Neutron scattering experiments show an incommensurate SDW with  $|\mathbf{q}_{\text{SDW}}| \sim \frac{21}{22} \frac{2\pi}{a}$ ,

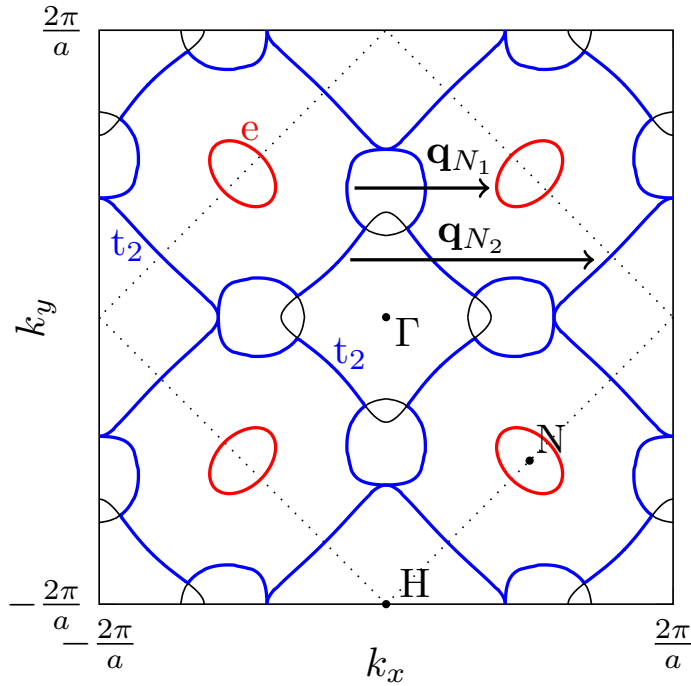


Figure 4.3.: (Color online) FS of Cr in the  $k_z=0$  plane. The different colors indicate different orbital character as described in Fig. 4.2 and the boundary of the 1BZ is indicated by dotted lines.

which corresponds to one of the nesting vectors of the Fermi surface. Fermi surface nesting was however not sufficient to explain why Mo, which has a very similar Fermi surface, does not display any SDW. This led to more refined susceptibility calculations [124, 126, 127], which showed that the susceptibilities of the two materials with matrix elements are quite different, with no obvious SDW instability in Mo.

The electronic structure of Cr in the experimental body centered cubic (BCC) crystal structure is shown in Fig. 4.2; the colored symbols indicate the partial character of the electronic bands:  $s$  (green),  $d$ - $e$ , i.e.,  $3z^2 - 1$ ,  $x^2 - y^2$  (red) and  $d$ - $t_2$ , i.e.,  $xy$ ,  $xz$  and  $yz$  (blue). The  $s$  band is entirely full, and extends from  $\sim 8$  to  $\sim 4$  eV below the Fermi level ( $\epsilon_F$ ). The  $d$  bands lie higher, with a clear separation between  $t_2$  bands, which form a narrow structure  $\pm 2$  eV around  $\epsilon_F$ , and  $e$  bands extending to higher energies. In many cases, however, the bands are not *pure*, i.e., they display contributions from more than one partial character, and this indicates a substantial hybridization between the corresponding real-space orbitals.

The resulting Fermi surface is three dimensional and comprises three types of sheets: large octahedral hole and electron pockets around the center ( $\Gamma$ ) and at the corner ( $H$ ) of the BZ, and several smaller hole pockets around the  $N$  points. A two-dimensional section

of the FS in the  $k_z=0$  plane is shown in Fig. 4.3; the color coding for the dominant partial characters is the same as in Fig. 4.2. The large pockets around  $\Gamma$  and H are mostly of  $t_2$  character, the small ellipsoids around N are mostly of e character.

Based on this electronic structure, we have used our highly accurate susceptibility program to compute the corresponding  $\chi^0$  along the (010)-direction from the  $\Gamma$  point of the 1BZ ( $\Gamma_0$ ) to the center of the next BZ ( $\Gamma_1$ ). In Fig. 4.4 we compare exact results where matrix elements are properly taken into account (black curve) with the CMA (red curve). The left scale belongs to the exact results and the right scale to CMA. The cross at  $|\mathbf{q}| = 0$  marks the value of the density of states at the Fermi energy  $N(\epsilon_F)$  given by the LAPW calculation, a value  $\chi^0(\mathbf{q})$  has to approach in the limit  $|\mathbf{q}| \rightarrow 0$ . Of course,  $N(\epsilon_F)$  can only be calculated reliably when matrix elements are correctly included. The agreement of  $\lim_{\mathbf{q} \rightarrow 0} \chi^0(\mathbf{q})$  with the exact value of the density of states is a stringent test for the  $k$ -space integration.

The exact result yields a broad bell-shaped curve with a small and narrow peak at  $\mathbf{q} = \mathbf{q}_{N_2}$ , with  $|\mathbf{q}_{N_2}| \approx 0.95 \frac{2\pi}{a}$ , which fits perfectly to the experimentally observed wavelength of the SDW in chromium, [125] and is in very good agreement with previous tight-binding [126] and supercell calculations.<sup>2</sup> Although there is a peak at the same wave number in the CMA result (red curve) as well, the rest of the susceptibility differs significantly from the exact result. In particular, we observe a second very strong peak at  $\mathbf{q} = \mathbf{q}_{N_1}$ , with  $|\mathbf{q}_{N_1}| \approx \frac{\pi}{a}$ , which is not present in the exact result.

In order to understand these results in detail, we first compare the converged susceptibility [Fig. 4.4(b)], which was obtained by summing over 30 bands, with the result we would obtain restricting the sum in Eq. (4.1) only to bands at the Fermi level [Fig. 4.4(a)]. First of all, we notice that the red curves in panels (a) and (b) are almost identical, i.e., in the CMA the shape of  $\chi^0$  is almost entirely determined by the transitions between bands at the Fermi level. The situation is very different for the exact susceptibility (black curves), where matrix elements strongly enhance transitions between “outer” bands, i.e., bands that do not cross the Fermi level; in this particular case, this enhancement is very strong for  $k$  points half-way between  $\Gamma$  and H.

While it is almost impossible to give a detailed account of all the transitions involving outer bands, since their number is very large, it is extremely instructive to trace back the enhancement of the susceptibility due to matrix elements, when only bands at the Fermi surface are included [panel a]. Indeed, the two peaks seen at  $q_{N_1}=0.52 \frac{2\pi}{a}$  and  $q_{N_2}=0.95 \frac{2\pi}{a}$  in the CMA correspond to two nesting vectors of the Fermi surface, illustrated in Fig. 4.3. The shorter vector ( $q_{N_1}$ ) connects the large hole FS with small ellipsoidal pockets around N, while the larger one ( $q_{N_2}$ ) connects it to the large electron pocket at H. The large difference in the matrix elements stems from the fact that  $q_{N_2}$  connects parts of the Fermi surface for which not only the geometrical, but also the orbital overlap, is large, and this does not happen for  $q_{N_1}$ .<sup>3</sup>

<sup>2</sup>For a review of SDW in Cr, see M. Bayer, PhD Thesis, TU Dresden 2008

<sup>3</sup>The effect of orbital overlap is easy to understand in the tight-binding approximation, [126, 135] where the matrix elements in Eqs. (4.1) and (4.2) are approximated by  $\sum_i c_i^n(\mathbf{k})c_i^m(\mathbf{k} + \mathbf{q})$ . Here,  $c_i^n(\mathbf{k})$  are the normalized coefficients of the  $i^{\text{th}}$  atomic orbitals for the electronic Bloch state of band  $n$  at wave-vector  $\mathbf{k}$ .

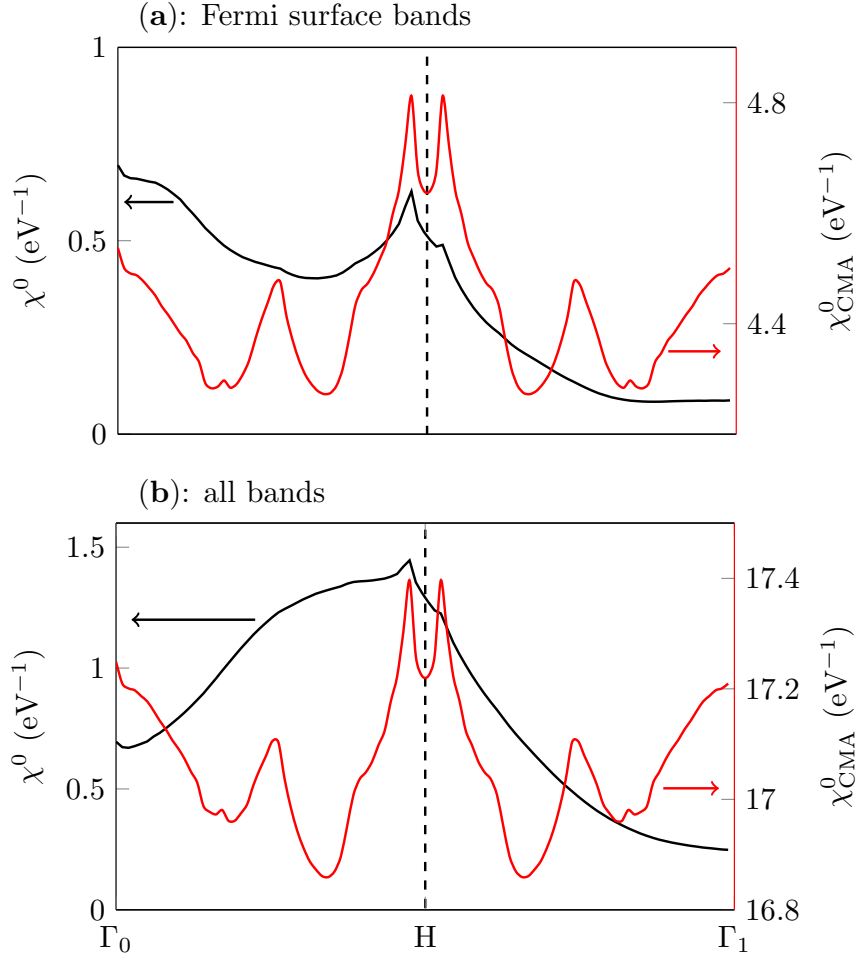


Figure 4.4.: (Color online) Static bare susceptibility  $\chi^0$  for Cr. CMA results (red, right axis) are compared with the exact results (black, left axis).  $\Gamma_1$  stands for the  $\Gamma$  point in the second BZ. The upper panel (a) shows the converged results, while in the lower panel (b) only the contributions of the bands at the Fermi level have been included in the susceptibility.

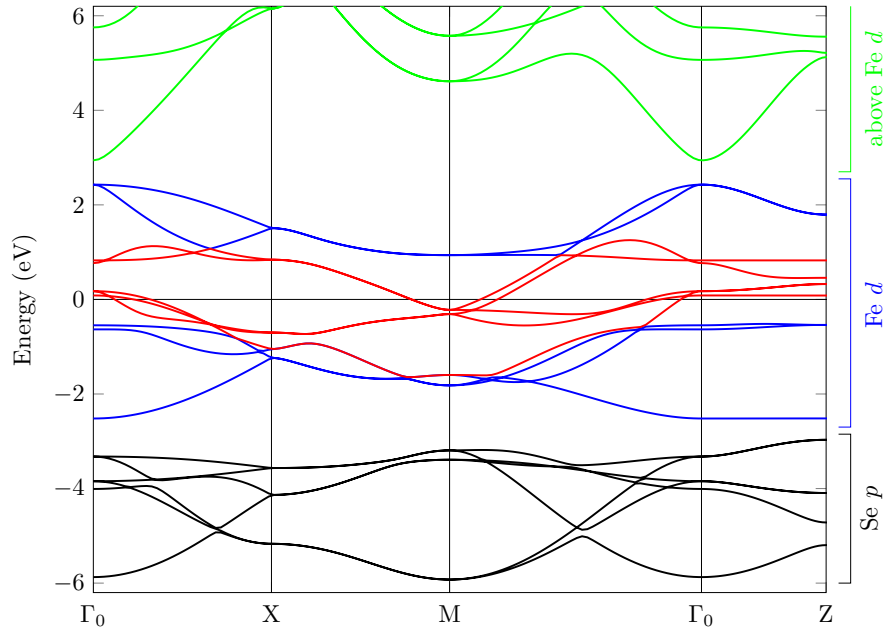


Figure 4.5.: (Color online) LDA bandstructure for FeSe at ambient pressure with the bands labeled according to their dominant orbital character. The five Fe  $d$  bands that form the Fermi surface are shown in red, while all other Fe  $d$  bands are depicted in blue. The Se  $p$  are shown in black and the bands above Fe  $d$  in green.

The main conclusions of our first detailed comparison is that the CMA is a very poor approximation for the full susceptibility for two reasons: (i) it overemphasizes the role of the bands that cross the Fermi surface; (ii) it neglects completely the information on the orbital character of the electronic states, which has a major effect on matrix elements. Finally, we also want to remark that in CMA, the  $\mathbf{q}$ -dependence of the susceptibility solely stems from the energies  $\epsilon_{\mathbf{k}+\mathbf{q}}$ , which are periodic with respect to any reciprocal lattice vector  $\mathbf{K}$  of the crystal. Therefore one has  $\chi^0(\mathbf{q}) = \chi^0(\mathbf{q} + \mathbf{K})$ , as observed in all red curves of Figs. 4.4, which is an artifact of the approximation.<sup>4</sup>

After the classical example of Cr, we next present results for FeSe as a representative example of the wide class of the recently-discovered FeSCs [1, 7], where models based on susceptibilities have played a major role in the past few years. For the following discussion we have chosen FeSe because it is one of the “simplest” FeSCs in terms of chemical formula and crystal structure. This allows us to discuss the electronic structure without entering the details of hybridization with intercalated atoms and layers and three-dimensional interlayer hopping; to avoid the problem of unfolding, we also chose to work in the two-Fe unit cell.

<sup>4</sup>For a more detailed discussion of momentum dependence of the matrix elements see Refs. [136, 137].

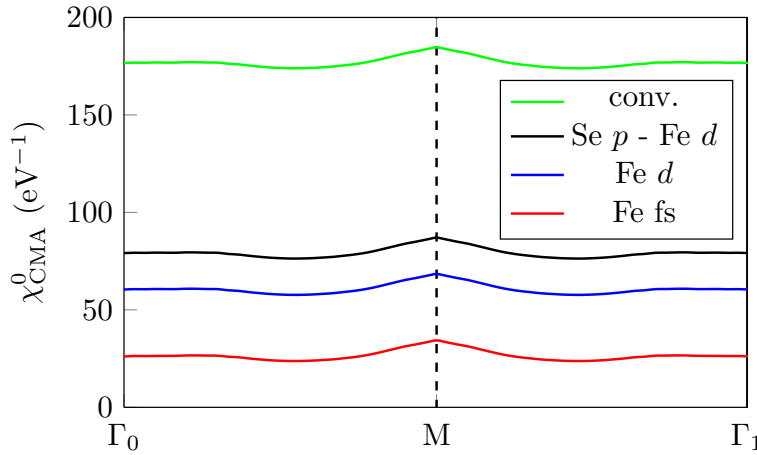


Figure 4.6.: (Color online) Static bare susceptibility in CMA  $\chi_{\text{CMA}}^0$  for FeSe calculated by including different sets of bands, as shown in Fig. 4.5. From bottom to top the included bands are: Fe  $d$  that cross the Fermi energy (red), all Fe  $d$  bands (blue), Se  $p$  plus all Fe  $d$  bands (black), and Se  $p$  plus Fe  $d$  plus all higher bands which are needed to ensure convergence of the full susceptibility  $\chi^0$ .

All calculations presented here employ the crystal structure at ambient pressure measured by Kumar *et al.* in Ref. [138]. Our electronic structure, shown in Fig. 4.5, agrees nicely with previous studies [16, 138]; similarly to what we did in Fig. 4.2, we have colored the bands according to their dominant character and/or position with respect to the Fermi level. This choice allowed us to introduce a compact notation for the susceptibility plots, but it does not permit one to appreciate the full complexity of the electronic structure. This issue is discussed in more detail in other publications [58, 135, 139]. Here we only want to recall that, due to the sizable  $p-d$  hybridization, there is a substantial contribution of Se  $p$  states to the Fe  $d$  bands, and vice versa.

The sixteen Fe  $d$  - Se  $p$  bands form a manifold which extends from  $\sim -6$  to  $\sim +2$  eV around the Fermi energy; the six lowest bands have mostly selenium character, and are separated by a small gap from the ten Fe bands at  $\pm 2$  eV. The Fermi level cuts the iron bands at a nominal electron count  $d^6$ , creating three hole pockets at the  $\Gamma$  point, and two electron pockets at the M point. The  $k_z$  dispersion of the bands is so small that the FS is essentially two dimensional.

The inner and outer hole pockets have dominant  $xz, yz$  orbital character, while the middle hole pocket is mostly of  $xy$  character; the electron pockets are formed by two ellipsoids with the long axis along the 110 and  $1\bar{1}0$  directions, with dominant  $xz/yz$  character on the long side and  $xy$  on the short one.

A clear geometrical nesting for  $\mathbf{q} \sim \text{M} = (\frac{\pi}{a}, \frac{\pi}{a}, 0)$  exists between the hole and electron pockets; this feature is common to many Fe-based superconductors, but the different

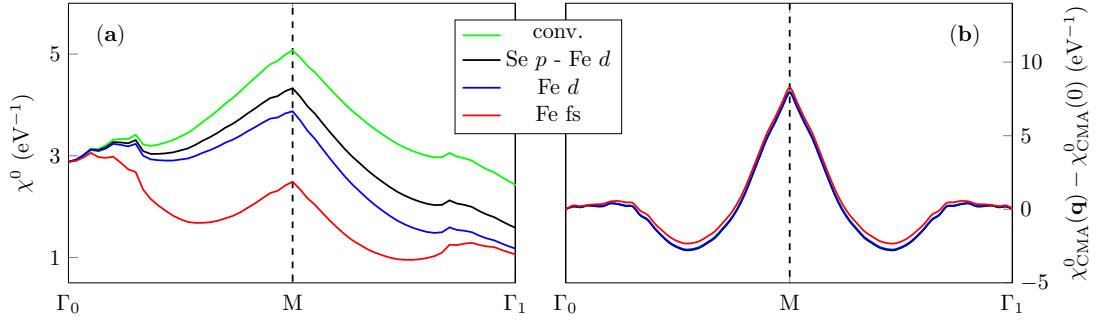


Figure 4.7.: (Color online) Static bare susceptibility  $\chi^0$  for FeSe at ambient pressure calculated by including different sets of bands, as explained in Fig. 4.6. The left panel (a) shows the exact result while the right panel (b) contains the CMA result.

shape and orbital composition in different compounds can lead to marked differences in the full susceptibility. Note also that all partial character of the hole and electron pockets match over a considerable part of the BZ.

We analyze its behavior in detail for FeSe, studying  $\chi^0$  in the (110)-direction in  $k$ -space. We start from the CMA picture, shown in Fig. 4.6. The color coding in the figure is consistent with Fig. 4.5:  $\chi_{\text{CMA}}^0$  results calculated considering only transitions between the Fe bands that create the Fermi surface are drawn in red, those which also involve the rest of the Fe  $d$  bands not crossing  $\epsilon_F$  in blue, while in black we have all transitions from Se  $p$  to Fe  $d$ . The converged results with respect to the number of bands is shown in green.

In  $\chi_{\text{CMA}}^0$ , since matrix elements are neglected and the denominator of Eq. (4.1) is almost  $k$  independent for large energies, the inclusion of more bands in the sum results in an almost rigid shift in the susceptibility, which decreases as  $1/\Delta\epsilon$  for bands away from the Fermi level. This background shift has no physical meaning, and in order to compare susceptibility curves with different numbers of bands, it is more meaningful to shift them to a common offset. This is done in the right panel of Fig. 4.7, where  $\chi_{\text{CMA}}^0$  is set to zero at  $|\mathbf{q}| = 0$  for all curves. Due to the constant matrix elements,  $\chi_{\text{CMA}}^0$  depends purely on  $1/(\epsilon_{\mathbf{k}}^m - \epsilon_{\mathbf{k}+\mathbf{q}}^n)$ . This expression is large only for the partially filled Fermi surface bands and  $\chi_{\text{CMA}}^0(\mathbf{q}) - \chi_{\text{CMA}}^0(0)$  therefore depends mainly on these bands; the most evident feature is a pronounced peak at the M point, due to the nesting of hole and electron Fermi sheets. An enhancement is seen also around the  $\Gamma$  point, for  $\mathbf{q} \lesssim 0.4\overline{\Gamma\text{M}}$  due to hole-hole and electron-electron transitions; no inter- or intra-band transitions are possible for  $0.4 \lesssim |\mathbf{q}| \lesssim 0.6\overline{\Gamma\text{M}}$ , and this accounts for the depletion seen in  $\chi_{\text{CMA}}^0$  for these values of  $|\mathbf{q}|$ .

The full susceptibility, with matrix elements correctly taken into account, is shown in the left panel of Fig. 4.7. We want to stress that in this case no scaling or shifting of the results has been performed. As long as all bands which cross the Fermi level are

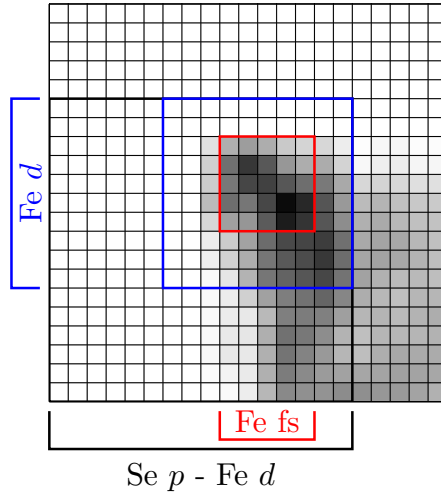


Figure 4.8.: (Color online) Contributions of the band transitions to  $\chi^0$  for FeSe at ambient pressure at the M point. The red square contains transitions only between Fermi surface bands and the blue square contains all band transitions between the Fe 3d bands. Inside the black square are all Fe  $d$  and Se  $p$  bands. We employed a logarithmic color scale to visually enhance small values.

included in the calculation,  $\chi^0$  approaches  $N(\epsilon_F)$  in the limit  $|\mathbf{q}| \rightarrow 0$ . Away from  $\Gamma_0$  the absolute value does of course depend on the number of included bands. All curves have a peak at the M point. However, quite surprisingly, the absolute maximum of the red curve, calculated based only on the Fermi surface bands, is not at M, but close to  $\Gamma_0$ . This means that at the Fermi surface the matrix element enhances hole-hole and electron-electron transitions more than electron-hole ones. Note that based on this result, we could conclude that this particular system has a dominant instability at small  $|\mathbf{q}|$ , at variance with most other FeSCs. However, the full susceptibility, including bands fairly away from the Fermi energy, has its maximum at M; the convergence to the exact curve in terms of included bands is quite slow<sup>5</sup>.

This is also graphically illustrated in Fig. 4.8, where the contributions of the individual band transitions to the susceptibility  $\chi^0$  at the M point are represented in a two-dimensional histogram. The red square contains all bands that create the Fermi surface, while the blue square includes all transitions between Fe  $d$  bands and the black square all Fe  $d$  and Se  $p$  bands. The biggest contribution originates from the transition of the middle hole pocket to the outer electron pocket of the Fermi surface. One can also observe that there are considerable contributions to the susceptibility outside the red square and also outside the blue square, again substantiating the vital importance of including enough bands in a  $\chi^0$  calculation. We note in passing that similar calculations

<sup>5</sup>We found that the results for the full  $\chi^0$  converge if approximately 50 bands around  $\epsilon_F$  are included.

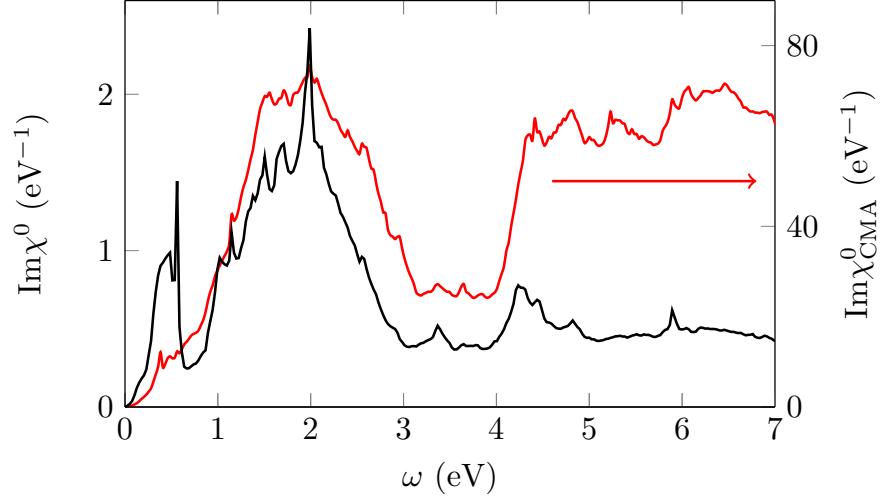


Figure 4.9.: (Color online) Imaginary part of the dynamic bare susceptibility  $\chi^0$  for FeSe halfway between  $\Gamma$  and M. The black line represents the result obtained with exact matrix elements and the red line depicts the CMA result.

for other FeSCs (not shown) display a different convergence as a function of the number of included bands.

We can summarize this section noting that in systems like FeSCs, with a complicated multi-orbital Fermi surface and a large  $p$ - $d$  hybridization which distributes the spectral weight of the bands over a wide energy range, susceptibility calculations are extremely delicate. In particular, one should avoid the CMA, as it can lead to wrong results, and carefully monitor the convergence of the results with the number of bands. The latter *caveat* is particularly relevant for model studies of trends in FeSCs based on downfolded models of the electronic structure [58, 135].

Needless to say, the convergence of the interacting susceptibility with the number of bands might differ, since  $s$ ,  $p$ , and  $d$  bands will respond differently to correlations due to different interaction parameters.

#### 4.4. Dynamic Bare Susceptibility

In addition to the static susceptibility, which is connected to instabilities towards ordered ground states, valuable information can be obtained also from the *dynamic* susceptibility. This quantity describes the elementary excitations of the system. We focus here on its imaginary part, which is directly related to scattering experiments and has therefore a transparent physical interpretation. We show below that the approximations discussed in the previous section for the static susceptibility have even more dramatic effects in the dynamical case. Of course, direct comparison to experiments requires knowledge of the full interacting susceptibility, which is beyond the scope of this work. However, a crucial

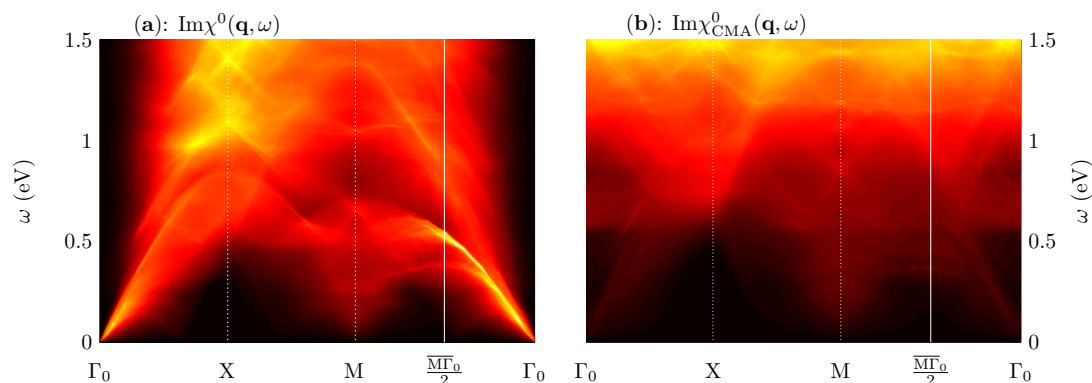


Figure 4.10.: (Color online) Imaginary part of the dynamic bare susceptibility for FeSe at ambient pressure. The left panel (a) shows  $\text{Im}\chi^0$  whereas the right panel (a) contains the results for  $\text{Im}\chi_{\text{CMA}}^0$ . The  $\mathbf{q}$  point shown in Fig. 4.9 is indicated by a vertical white line.

ingredient to all theoretical descriptions is a proper calculation of the bare susceptibility, which we discuss here.

In Fig. 4.9 we show the frequency dependence of  $\text{Im}\chi^0$  for a representative  $\mathbf{q}$  point in the 1BZ, which sits half-way between  $\Gamma$  and M. The black line shows the result with all matrix elements properly included. As compared to the CMA result, the matrix elements strongly enhance some parts of the spectrum and suppress others. For example, the small shoulder around 0.5 eV in the CMA result (red line) is enhanced forming a well-defined peak, while the high-energy contributions are strongly suppressed. The reason for this deviation is again that the CMA completely neglects the effect of orbital character, leading to an overestimation of certain transitions. This is most obvious for energies above 4 eV, where the discrepancy increases sharply. At this energy, the transitions are to a very large extent from the bands with dominant Se  $p$  orbital character to those with dominant Fe  $d$  and vice versa. In this case, the matrix elements are small compared to direct  $d$ - $d$  transitions; this effect is not at all reflected in the red curve of Fig. 4.9. As a result, the overall spectral weight in the CMA is too large at high frequencies. The susceptibility even shows a linear increase for very large frequencies, which makes the use of a Kramers-Kronig transformation meaningless.

Figure 4.10 shows intensity plots along high symmetry lines in the 1BZ for  $\text{Im}\chi^0$  (left) and  $\text{Im}\chi_{\text{CMA}}^0$  (right). The  $\mathbf{q}$  point used in Fig. 4.9 is indicated by a vertical white line. The narrow peak at approximately 0.5 eV in Fig. 4.9 translates into a well-defined branch of single-particle excitations, extending up to 0.7 eV. Another high-intensity region of  $\text{Im}\chi^0$  starts around 1 eV, concentrated at the X point. In the CMA results, the spectral weight distribution is very different. For example, the low energy branch is almost completely suppressed and a large, featureless continuum above 1.5 eV appears.

The bare spectrum as presented here contains information about the single-particle

excitations of the system, and these can be measured by inelastic neutron scattering. However, their intensity is rather weak compared to collective excitations, such as (para)magnons.

As mentioned above, these require a calculation of the full susceptibility, which is highly non-trivial. Even if one of the simplest approximations is used, namely the random-phase approximation (RPA) [18, 32], further assumptions on the interaction Hamiltonian are needed to make the calculation feasible; in particular, the computational cost grows with the number of included bands, and this requires downfolding the electronic structure to an effective low-energy model. More refined methods exist - FLEX, fRG - which improve the treatment of many-body interactions, but they are even more expensive computationally. An alternative approach that treats the interacting kernel *ab initio* has been suggested recently by Essener *et al.* [52].

However, every calculation for the full susceptibility relies on an accurate evaluation of the bare susceptibility. Following results of Ref. [52], we want to note that the position of collective excitations is crucially influenced by the precise structure of the bare susceptibility. For instance, (para)magnon dispersions form in regions of the  $\mathbf{q}$ - $\omega$  plane, where the intensity of the single-particle excitations is low. This of course means that a precise calculation of the bare susceptibility, as we present it in this work, is an absolutely necessary ingredient also for an accurate calculation of the interacting susceptibility, which can then be compared to experimental results.

## 4.5. Conclusions

In this paper we have presented a practical implementation of bare static and dynamic susceptibilities, based on full-potential LAPW calculations, and a very efficient tetrahedron method for  $k$ -space integration. This allowed us to study in detail the effect of matrix elements and the convergence with the number of bands for some representative and topical materials (Cr, FeSe). We were able to show that the approximation, where all matrix elements in the susceptibility formula are replaced by a constant value (CMA), can lead to unreliable results. Therefore, nesting arguments, which are based on this approximation and are often employed to explain instabilities towards different orderings, are many times unfounded. [134, 140]

Moreover, we have studied the convergence of the results as far as the summation over the bands is concerned. It appears that the convergence is slower than commonly expected. This could affect schemes that are based on downfolded models of the electronic structure, where only a few bands are taken into account. These effects, already significant in the static susceptibility, are even more severe for the dynamic susceptibility. For instance, low-energy excitations might not be visible or misplaced when matrix elements are not treated properly.

In view of the unpredictable accuracy of CMA and/or a band-summation restriction it is advisable to refrain from any approximations and to evaluate the susceptibility formula exactly. One possible and efficient approach has been presented in this paper.

## **Acknowledgments**

We are grateful to E. Schachinger for insightful discussions. Calculations have been done on the dcluster of TU Graz. L.B. acknowledges financial support from DFG, Project No. SPP1458 BOE3536-2. We thank NAWI Graz for support.



# Chapter 5.

## LaFeAsO and the Effects of Doping

### 5.1. Introduction

The field of iron-based superconductors was established with the discovery of superconductivity in fluorine-doped LaFeAsO<sub>1-x</sub>F<sub>x</sub> by Kamihara *et al.* [1] in 2008, which is *the* prototypical example for an FeSC of the 1111 family. In LaFeAsO, superconductivity was introduced by replacing oxygen, which is in a 2<sup>-</sup> oxidation state, with fluorine. As F has an oxidation number of 1<sup>-</sup>, this doping process adds electrons to the system. The phase diagram for LaFeAsO, summarized in Ref. [142], is reproduced here in Fig. 5.1 with kind permission from the publisher. From  $x = 0$  to approximately 0.04, one observes a single-stripe antiferromagnetic ground state of the parent - and weakly doped - material. With increased F doping (open squares) the superconducting behavior sets in and reaches its maximum  $T_c \approx 26$  K at 11% electron doping. Because of the poor solubility of fluorine for concentrations  $x > 0.2$ , an F *overdoping* of the compound is not possible and the full phase diagram with respect to doping could not be obtained.

In 2012, however, Iimura *et al.* [142] doped LaFeAsO with hydrogen (filled symbols in Fig. 5.1), which has a much better solubility in LaFeAsO. It was therefore possible to reach higher doping concentrations and to dope the system up to the breakdown of superconductivity at about  $x \approx 0.53$ . These authors found a *two-dome* structure with maxima at  $x \approx 0.08$  and 0.36 at ambient pressure (filled squares). It has to be said, however, that the errors in the experiments in the region of minimal  $T_c$  are quite large. It is imaginable that the dependence of  $T_c$  as a function of doping exhibits not a pronounced two-dome feature, but rather a very broad plateau.

In the region of the phase diagram, where both F and H doping are possible, the qualitative agreement between the two different dopings is very good. This is remarkable, as the sizes of the H and F atoms are quite different and one would therefore expect a stronger response from the lattice. At higher pressures of 3 GPa, Iimura *et al.* don't find a two-dome structure, but a very broad peak (inverted triangles). One has to be careful with interpreting this higher pressure data set, however, as the experimental data points are very scarce.

In the following, we want to investigate the low-energy behavior of doped LaFeAsO and study the response of the bare susceptibility to the application of doping. From a theoretical point of view it is more advantageous to consider F doping with a hypothetically unlimited solubility instead of H doping, as fluorine is much closer to oxygen in terms of atomic number and mass. A first hint that both types of doping result in the

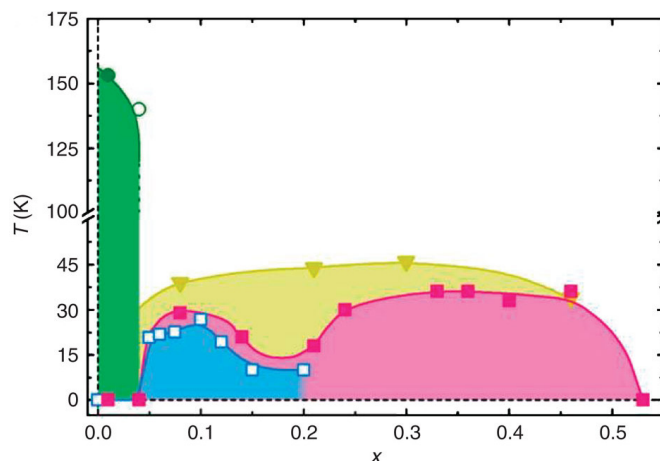


Figure 5.1.: Electronic phase diagram for  $\text{LaFeAsO}_{1-x}\text{H}_x$  (filled symbols) and  $\text{LaFeAsO}_{1-x}\text{F}_x$  (Ref. [141]; open symbols). The  $T_c$  obtained under ambient pressure is shown with squares and for 3 GPa with inverted triangles. Reprinted by permission from Macmillan Publishers Ltd: Nature Communications 3, Article number: 943, Iimura *et al.*, copyright 2012.

same behavior has already come from the overlap of the  $T_c$  vs. doping concentration curves in the phase diagram of Fig. 5.1.

Other evidence of the equivalence of F and H as electron donors for the 1111 FeSCs comes from Matsuishi *et al.* [143]. They performed detailed studies on the behavior of the closely related compound  $\text{CeFeAsO}$  when doped with either H or F. By looking at the bandstructure and density of states, they found that, apart from the  $2p$  fluorine and the  $1s^2$  hydrogen bands far away from the Fermi energy, the low-energy behavior of  $\text{CeFeAsO}_{1-x}\text{H}_x$  is practically identical to the one of  $\text{CeFeAsO}_{1-x}\text{F}_x$ . Ref. [143] also reports the composition of the compounds, showing that H is actually substituting the O atoms and is not simply incorporated in interlayers. Additionally, they point out that the unit cells of all their measured compounds correspond to the same  $\text{ZrCuSiAs}$ -type (P4/nmm) structure. More studies on the effects of hydrogen doping on parent materials of the type  $\text{ReFeAsO}$  with  $\text{Re}=\{\text{Ce}, \text{Sm}, \text{Ca}\}$  can be found in Refs. [143–145].

With the knowledge that H and F doping have very similar effects on the electronic bandstructure and that the lattice constants are in a first approximation unchanged, it is valid to assume F doping with a hypothetically unlimited doping range. For a theoretical investigation of doping effects, two very common approximations in first-principle calculations to avoid huge supercells are the *rigid band model* and the *virtual crystal approximation* (VCA). A rigid band approximation is a simple shift of the Fermi energy that leaves the band curvatures unchanged. In VCA, on the other hand, the integer electron number of a given atom is changed to a non-integer one in order to represent doping or impurity effects in the crystal (see for example Ref. [146]). This

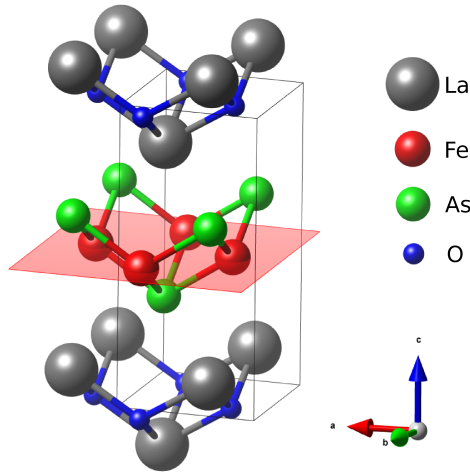


Figure 5.2.: Crystal structure of LaFeAsO with the unit cell indicated by the solid black lines. The Fe plane is indicated by the red shading.

works reasonably well as long as the core electrons of the original atom match the core electrons of the substituting atom. As VCA also takes into account changes in the band structure apart from a simple shift of the filling, this method is clearly preferable to the rigid band model and has therefore been also applied in our studies.

The crystal structure of LaFeAsO is depicted in Fig. 5.2. The Fe atoms are shown in red and the plane of the Fe square lattice is schematically drawn in transparent red. Tetrahedrally coordinated to them are the As atoms. Intercalated in these FeAs planes are the LaO planes, where also the O atoms form a square lattice with La on their tetrahedral positions.

Iimura *et al.* [142] reported the experimental As heights but unfortunately no information on the other unit cell parameters were given. We therefore used the unit cell parameters  $a = b = 7.6250 a_0$ ,  $c = 16.5181 a_0$  (in the P4/nmm crystal structure) and  $z_{La} = 0.1415$  from Ref. [20]. The  $z_{As}$  as a function of doping used were taken from a linear fit of the experimental values reported by Ref. [142]. These values can be found in Table 5.1.

For our DFT calculations we again employed the FP-LAPW package WIEN2k [121] using a GGA-PBE exchange-correlation functional [147].<sup>1</sup>

Fig. 5.3 shows the bandstructure for the undoped parent compound LaFeAsO. From  $-5.5$  eV to  $-2$  eV are mostly As  $p$  bands, which are shown in black. Then subsequently with a small gap at  $-2$  eV up until about  $2.2$  eV lie the Fe  $d$  bands. The five Fe bands, which cross the Fermi energy, are depicted in red in Fig. 5.3, while the other Fe bands

<sup>1</sup>RKmax was set to 7.0 and the following MT radii were chosen:  $La_{RMT} = 2.36 a_0$ ,  $Fe_{RMT} = 2.40 a_0$ ,  $As_{RMT} = 2.13 a_0$  and  $O_{RMT} = 2.09 a_0$ . For the DOS calculations we used Gaussian broadenings of 0.003 and 0.006 and counterchecked the results.

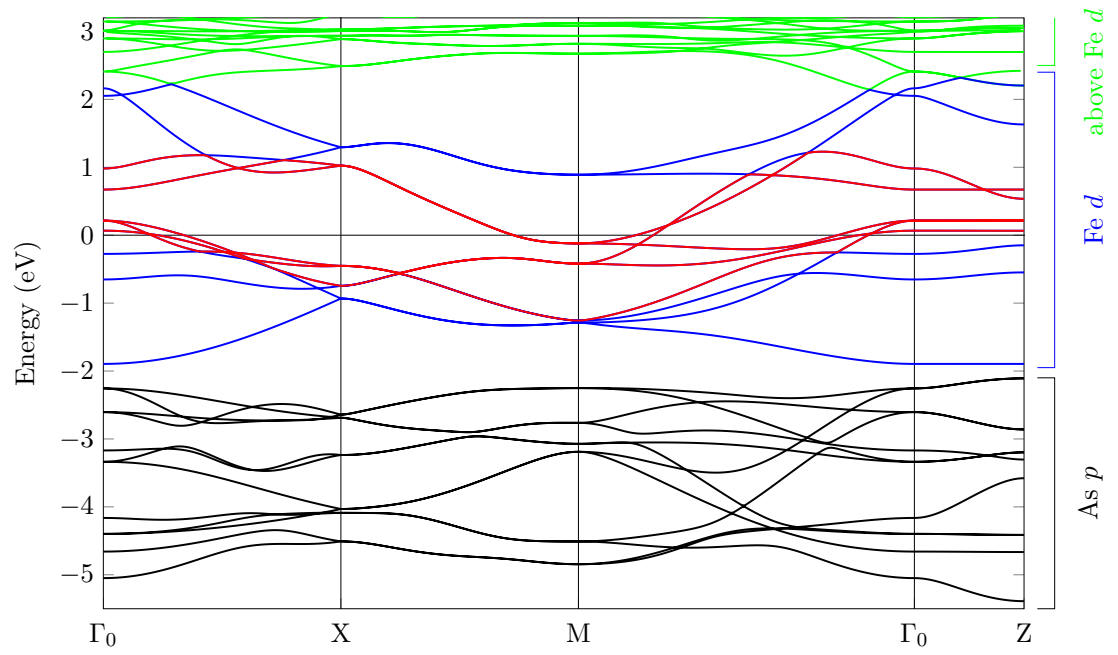


Figure 5.3.: DFT bandstructure for *LaFeAsO*. The five Fe *d* bands that form the Fermi surface are shown in red, while all other Fe *d* bands are depicted in blue. The As *p* are shown in black and the bands above Fe *d* in green.

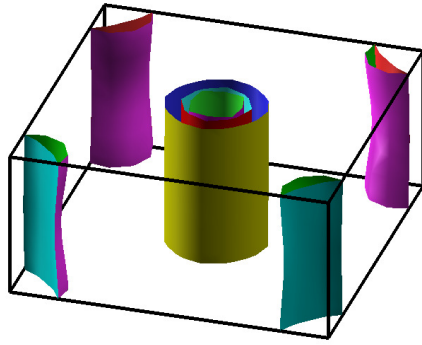


Figure 5.4.: Fermi surface of LaFeAsO with the reciprocal unit cell indicated by the solid black lines.  $\Gamma$  is at the center of the reciprocal unit cell and the M points are located at the corners.

are shown in blue. All bands above the Fe  $d$  are drawn in green. Undoped LaFeAsO constitutes a prototypical example for a FeSC bandstructure. At the  $\Gamma$  point one finds three hole pockets and at the M point there are two electron pockets, all having  $xy$  and  $xz+yz$  character. The dispersion of the bands in LaFeAsO is also exceptionally low in  $z$ -direction, giving an almost perfect two-dimensional character to the Fermi surface, which therefore consists of five cylinders. Depending on the structural details (for example, if one uses experimental structures instead of DFT optimized ones), another heavy hole pocket may appear at the Z point with  $z^2$  character and considerable dispersion along the  $z$ -direction. The Fermi surface for the structure given in Ref. [142] is shown in Fig. 5.4 and a cut through the  $k_z = 0$  plane is presented in the left panel of Fig. 5.8, where the three concentric cylinders of the hole pockets in the center and the two cylinders from the electron pockets at the M points are depicted. (see also Refs. [17, 33, 120])

After having discussed the electronic structure of the undoped material, we now want to focus on the effects of electron doping on the low-energy physics of LaFeAsO. For the corresponding band structure calculations of LaFeAsO $_{1-x}$ F $_x$  in the VCA, we reset the oxygen charge ( $Z = 8$ ) by a virtual nuclear charge of  $Z = 8 + x$ , where  $x$  is the fluorine fraction. Additionally, we reset the original value of  $z_{As}$  by  $x$ -dependent values which were taken from a linear fit of the experimental values reported in Ref. [142]. These values can be looked up in Table 5.1 along with the calculated Fermi energies and DOS at  $\epsilon_F$  as a function of F doping. As we are adding electrons to the system, the Fermi energy has to increase with increasing concentration of F atoms. The monotonic increase of  $N(\epsilon_F)$ , however, is not immediately evident. We therefore provide in Fig. 5.5 a better picture of the behavior of the DOS in the low energy regime. In this picture, the 40% doping case has been omitted for the sake of readability.

Apart from the increasing value of  $N(\epsilon_F)$ , there is another very interesting effect of the doping visible at around  $-0.5$  eV. As one can see in the green line, which represents

Table 5.1.: Experimentally determined As positions  $z_{As}$  for various dopings (see Ref. [142]). The dopings not coinciding with the exact experimental values were calculated using a linear fit. Additionally, the Fermi energies  $\epsilon_F$  in eV and the DOS at  $\epsilon_F$  are given.

x	$z_{As}$ [Å]	$\epsilon_F$ [eV]	$N(\epsilon_F)$ [eV <sup>-1</sup> ]
0.00	1.3053	8.2	4.15
0.10	1.3134	8.7	4.19
0.20	1.3279	8.9	4.37
0.30	1.3453	9.0	4.77
0.40	1.3642	9.1	5.23

the undoped compound, there is a lot of weight in the DOS at  $\approx -0.4$  eV. This feature becomes smaller and is shifted to lower energies when doping is increased. We will see later on, when discussing the imaginary part of the dynamic susceptibility, that there are excitations with wave vector  $(\pi, \pi, 0)$  showing a similar dependence on doping, i.e., a shift to higher energies and decreasing strength. We attribute this effect to the fact that the bands responsible for the high weight of the DOS are the same ones creating the excitations.

The low energy bandstructure as a function of doping can be seen in Fig. 5.6. The bands of the undoped compound is again depicted in green, the 10% doped compound in black and the bands of the 20% doped one in blue. The other cases of 30% and 40% doping are not shown in order to keep the figure easily readable. There are two major effects to be observed here: First, the bandstructures are shifted downwards with increased doping as electrons are added.<sup>2</sup> Second, we see that the differences in the bands at the M point for example are quite small, while they are big for  $\Gamma_0$  and Z. This difference in the curvature of the bands would have been overlooked in a rigid band approximation (see also Ref. [148]). As the susceptibility, which we will discuss later, depends very strongly on even small changes in the bandstructure, it is favourable to describe the doping at least on the level of a VCA approximation.

## 5.2. Static Bare Susceptibility

The static bare susceptibility for LaFeAsO<sub>1-x</sub>F<sub>x</sub> has been calculated as described in Sec. 2 and 3 and is plotted along the (110) direction in Fig. 5.7. Matrix elements have been properly included, which leads to the already discussed loss of periodicity of  $\chi^0$  in reciprocal space.<sup>3</sup> The gray shaded areas in the vicinities of  $\Gamma_0$  and  $\Gamma_1$  are regions with very small  $\mathbf{q}$ . It depends a lot on the material, if our numerical implementation

<sup>2</sup>The Fermi energy is set to  $\epsilon_F = 0$ .

<sup>3</sup>We included more than 50 bands around the Fermi energy in order to assure convergence with respect to bands. 546  $k$  points in the irreducible wedge were chosen for the integral over 1BZ and 3993 plane waves to describe the matrix elements.

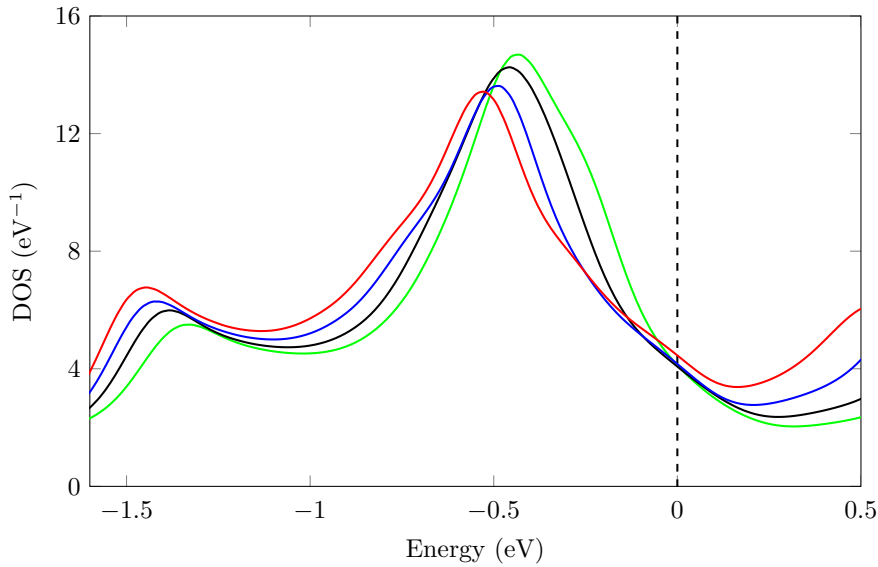


Figure 5.5.: DOS of  $\text{LaFeAsO}_{1-x}\text{F}_x$  near the Fermi energy at  $\epsilon_F = 0$  as a function of doping. The  $\text{LaFeAsO}$  DOS is shown in green, the DOS for 10% doping in black, for 20% in blue and for 30% in red.

can deal well with these extreme cases of  $\mathbf{q}$ . While it works reasonably well in the case of  $\text{FeSe}$ , discussed in Sec. 3, our tests showed that the computation struggles in the case of  $\text{LaFeAsO}$ . Anywhere outside the shaded areas, however, our calculations are very reliable.

The susceptibility of undoped  $\text{LaFeAsO}$  is drawn in green, the 10% doped compound in black, 20% in blue and the case with a doping concentration of 30% in red.  $\chi^0$  of the undoped material features a pronounced maximum at the M point, presented already in many studies, as for example in Refs. [33, 43, 45, 79, 120]. This maximum is attributed to the nesting of the Fermi surface cylinders at  $\Gamma$  with those at the M point. In general, a maximum of  $\chi^0$  at  $\mathbf{q}$  gives the wave vector, where the system is most instable towards charge or spin fluctuations and might develop a long-range, itinerant magnetic order. Indeed, experiments find single stripe antiferromagnetic order in  $\text{LaFeAsO}$ , which is in accordance with the  $(\pi, \pi, 0)$  nesting vector observed in  $\chi^0$ .

When electrons are added to the system via doping, the radii of the electron pockets grow while the radii of the hole pockets shrink. This can be seen by comparing the left and right panel of Fig. 5.8, where we show a cut through the Fermi surface at  $k_z = 0$  for undoped  $\text{LaFeAsO}$  (left) and 20% electron doping (right). A perfect nesting of the cylinders over large areas is no longer existing in the doped case, notable in a reduction of  $\chi^0$  at the former nesting vector. Although the curvatures of the cylinders do not match each other as nicely as for the undoped compound, one can still get portions of the Fermi surfaces to overlap by shifting  $\mathbf{q}$  by  $\Delta q$ , which is the difference in the cylinders'

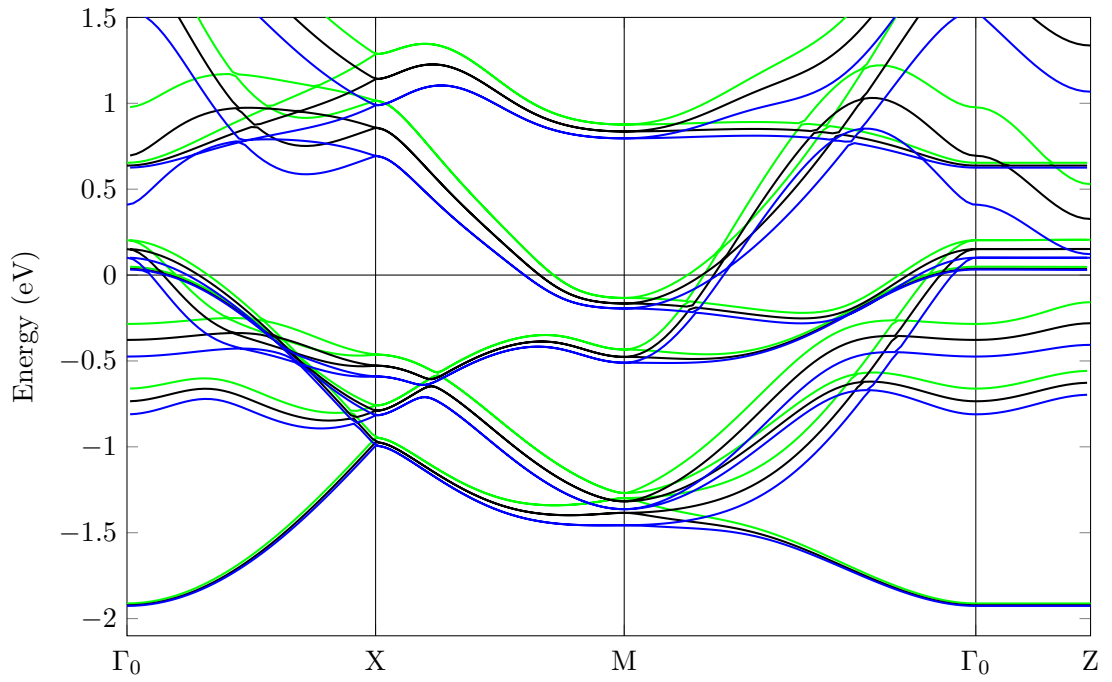


Figure 5.6.: DFT bandstructure for  $\text{LaFeAsO}_{1-x}\text{F}_x$  as a function of doping. The LaFeAsO bands are shown in green, the bands for 10% doping in black the the ones for 20% in blue. The Fermi energy for all bandstructures was chosen to be  $\epsilon_F = 0$ .

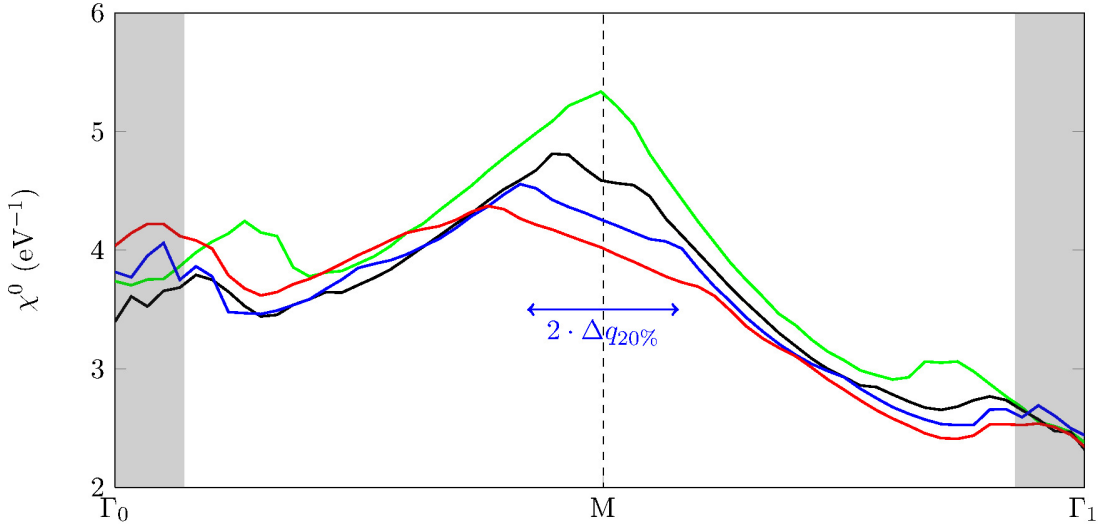


Figure 5.7.: Static bare susceptibility  $\chi^0$  for LaFeAsO (green), LaFeAsO<sub>0.9</sub>F<sub>0.1</sub> (black), LaFeAsO<sub>0.8</sub>F<sub>0.2</sub> (blue) and LaFeAsO<sub>0.7</sub>F<sub>0.3</sub> (red). The gray-shaded areas are areas with very small  $\mathbf{q}$ , where the reliability of our calculations is lessened. The blue arrow marks the length  $2 \cdot \Delta q_{20\%}$ , where  $\Delta q_{20\%}$  is the difference of the Fermi cylinders' radii for the 20% doping case.

radii. This  $\Delta q$  is easily discernable as a plateau in  $\chi^0$ , as shown for the 20% doping case in Fig. 5.7 (see also Ref. [149]). With increasing doping this difference in the radii becomes bigger, until the Fermi surface topology loses its cylindrical shape entirely.

We want to investigate this doping effect on the bare static susceptibility further by considering not only the path  $\Gamma_0$ -M- $\Gamma_1$  as before, but explore the whole  $(q_x, q_y, 0)$  plane. The results of such a calculation are reported in Fig. 5.9, where we show  $\chi^0$  in the  $q_z = 0$  plane for undoped LaFeAsO in the left panel and for 20% doped compound LaFeAsO<sub>0.8</sub>F<sub>0.2</sub> in the right panel. The parent compound on the left emphasizes the results already reported in Fig. 5.7, i.e., the typical strong response expected from an 1111 FeSC with the marked peaks at the M points. The 20% doped material, however, reveals that doping does not simply cut through the peaks, leaving an area of constant gradient with size  $2 \cdot \Delta q$ , but actually shifts weight to other areas of the BZ. Figuratively speaking, Fig. 5.9 (right) looks like cylinders with radius  $\Delta q$  and main axis in the  $\Gamma_0$ -M direction being “pressed” into  $\chi^0$  at the M point, thus shifting weight into the M-X-M directions.

This means that the strength of the instability towards a magnetic ordering of the system is much reduced, as this depends solely on the value of the maximum of  $\chi$ , while the superconducting pairing is an integral over the whole 1BZ with  $\chi$  appearing in the kernel (see Sec. 2). In relation, the superconducting state should become more stable than the long range magnetic order upon doping, which may explain the increase of  $T_c$

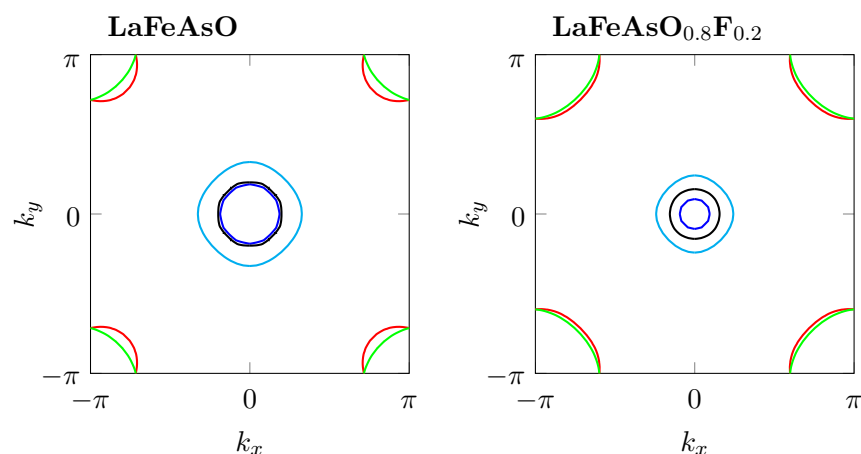


Figure 5.8.: Top view of the Fermi surface at  $k_z = 0$  of LaFeAsO (left) and LaFeAsO<sub>0.8</sub>F<sub>0.2</sub> (right). Different colours indicate different bands.

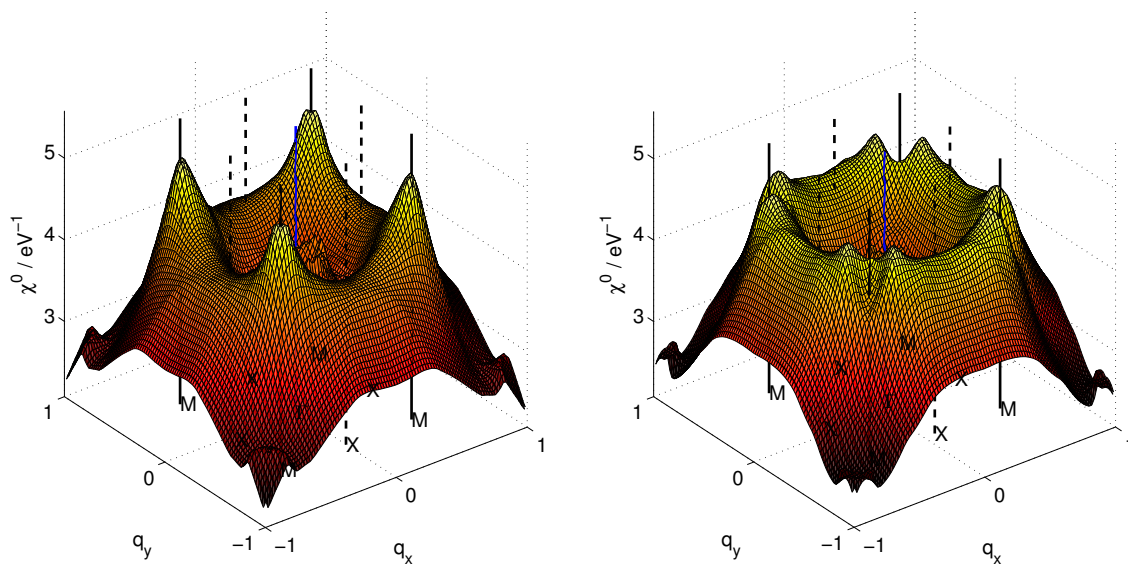


Figure 5.9.:  $\chi^0(\mathbf{q})$  as a function of  $\mathbf{q} = (q_x, q_y, 0)$  for undoped LaFeAsO (left) and LaFeAsO<sub>0.8</sub>F<sub>0.2</sub> (right). The components of the wave vector  $\mathbf{q}$  are given in units  $\pi/a$ . The blue vertical line marks  $\Gamma$  in the center of the 1BZ, the black solid lines specify the M points at  $(\pm\frac{1}{2}, \pm\frac{1}{2}, 0)$  and the dashed lines the positions of X at  $(\pm\frac{1}{2}, 0, 0)$  and  $(0, \pm\frac{1}{2}, 0)$ .

with doping in LaFeAsO. This simple argumentation, however, is not very satisfactory and also can't explain the double-dome feature observed by Iimura.

In Refs. [148] and [150] the behavior of the static susceptibility of LaFeAsO as a function of doping was also studied with included interactions. There, the authors calculate DFT bandstructures for various cases of doping and derive a five-band tight-binding model. From this tight-binding fit, with the inclusion of spin and orbit interaction, the RPA susceptibility is calculated.<sup>4</sup> From their results in Ref. [150], the authors conclude that the second superconducting dome in LaFeAsO is associated with a new antiferromagnetic ordering. Ref. [148] explains the reappearing order of spins and orbitals for  $x \sim 0$  with commensurate electron-hole FS nesting, while for  $x \sim 0.4$  it is due to an incommensurate electron-electron FS nesting. It has to be said, however, that these theoretical results and even the experimental ones are still debated about,<sup>5</sup> as the double-dome could also be a simple single-dome structure with a very broad maximum, within the errors given for the experiment.

### 5.3. Dynamic Bare Susceptibility

In this section, we will present results of the dynamical bare susceptibility obtained with our method as a function of electron doping, as results on dynamic bare susceptibilities for LaFeAsO are very scarce (see [79]). The dynamical part of the susceptibility, as already discussed in Sec. 2, is directly related to INS experiments. Of course, to correctly describe the excitations of real systems, we would also need to include interactions and correlations in our calculations of the dynamical susceptibilities. Yin *et al.* in Ref. [28] however showed in DMFT calculations that materials of the 1111 and 122 families are amongst the least correlated compounds with mass enhancement factors between 2 – 3, compared to 3 – 7 for iron-chalcogenides. We therefore think that important aspects of the excitation spectrum of LaFeAsO can already be seen within a dynamical calculation of  $\chi^0$ , while for the collective excitations a RPA treatment should allow for a comparison with experiment. The numerical evaluation of  $\text{Im}\chi(\mathbf{q}, \omega)$  has already been discussed in Sec. 3 and we will in the following present results obtained for LaFeAsO and the effect of doping.

We show the imaginary part of the dynamical bare susceptibility for undoped LaFeAsO along high symmetry lines in the left panel of Fig. 5.10. As we are working in the non-interacting regime, the bright areas in the surface plot represent single-particle excitations. An excitation without energy gap arises for small  $|\mathbf{q}|$ , i.e., at the  $\Gamma$  point, both in the (100) and (110) direction. With increasing  $|\mathbf{q}|$ , the peak of the excitations gets shifted to higher frequencies. In the low-energy regime we find another, yet weaker excitation at the M point, which disperses in the form of an arc towards  $\Gamma$ . At 0.5 eV there is another excitation with very low dispersion at M. A hint that the  $\sim 0.5$  eV range will be a hotspot for excitations was already given in the DOS, shown in Fig. 5.5, as a lot of

<sup>4</sup>see Ref. [32] and references therein for an excellent review on these tight-binding models for FeSCs and RPA calculations.

<sup>5</sup>D. Singh, private communications

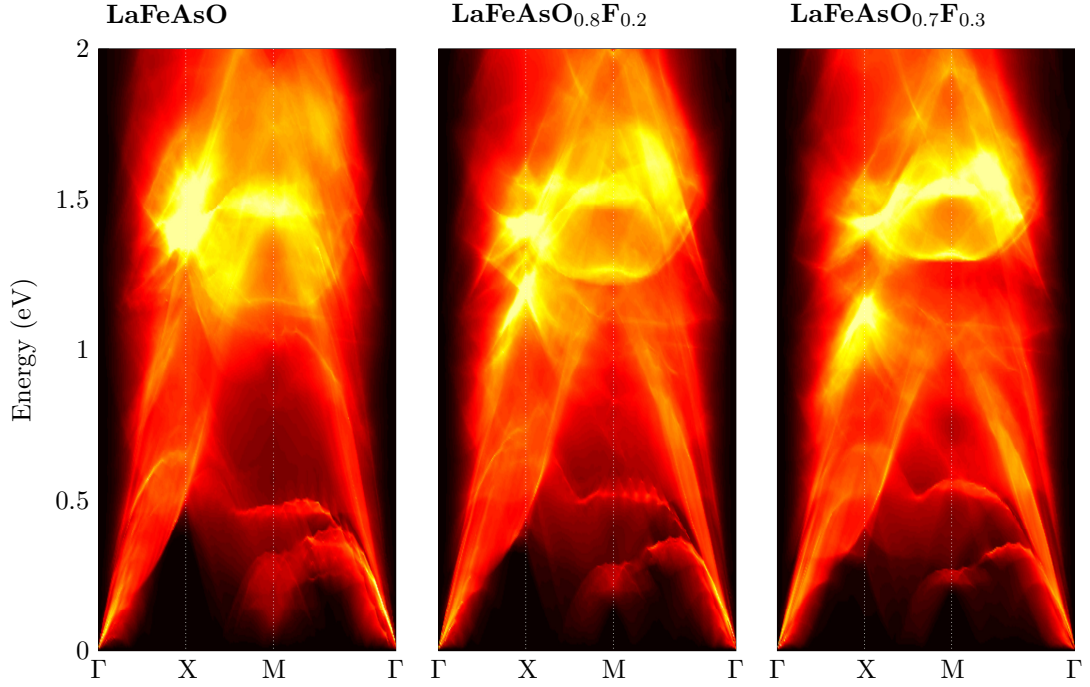


Figure 5.10.:  $\text{Im}\chi^0(\mathbf{q}, \omega)$  along high symmetry lines for undoped LaFeAsO (left) and LaFeAsO<sub>0.8</sub>F<sub>0.2</sub> (middle) and LaFeAsO<sub>0.7</sub>F<sub>0.3</sub> (right). The colormap was chosen in a way that black represents vanishing values and the brightest yellow is  $5 \text{ eV}^{-1}$ . All panels share the same scaling of the colormap.

states are available in this energy regime. In the higher-energy region at approximately 1.4 eV we observe the strongest peak at the X point.

The middle and right panels of Fig. 5.10 depict  $\text{Im}\chi^0$  for the cases of 20% and 30% electron doping, respectively. In comparison with the undoped compound we find that the long wavelength excitations, i.e., at  $\Gamma$ , are basically unchanged. At  $(\pi, \pi, 0)$ , however, a gap opens, which increases with doping. Also at 0.5 eV, the former low dispersing, broad feature gets pushed to higher energies and becomes more curved. The higher energy excitation at 1.4 eV around  $(\pi, 0, 0)$  gets split into two clearly separable excitations, when the system is doped. With increasing doping, one of these excitations is shifted to lower energies and lies around 1.2 eV for LaFeAsO<sub>0.7</sub>F<sub>0.3</sub>, while the second one is more or less pinned to 1.4 eV and does not move as a function of doping.

To better distinguish the single excitations we plot in Fig. 5.11 the imaginary part of  $\chi^0(\mathbf{q}, \omega)$  at two fixed wave vectors  $\mathbf{q}$ . The upper panel shows  $\text{Im}\chi^0$  at the X point, where the undoped compound is represented by the green curves and the 30% doped compound by the red curve. The red arrows indicate the splitting of the big excitation of LaFeAsO at 1.4 eV into two peaks located at around 1.2 eV and 1.4 eV. We also observe the clear energy gap at this wave vector.

The lower panel of the same figure shows the same quantities and compounds as the

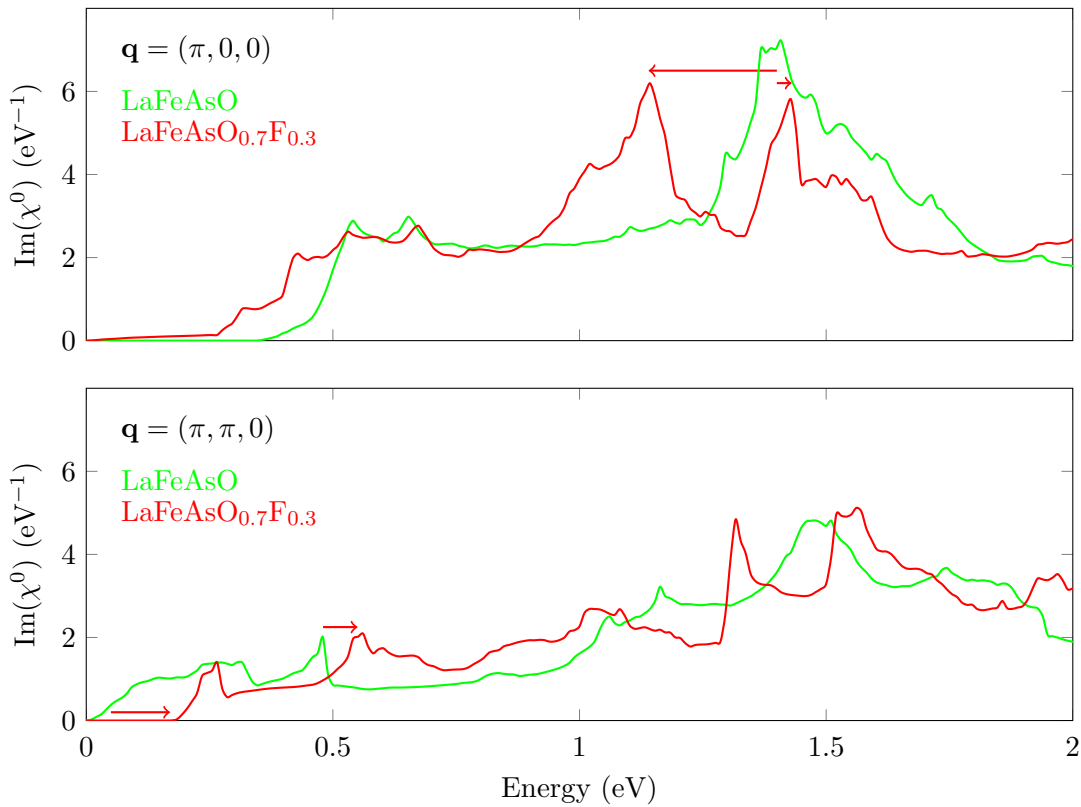


Figure 5.11.:  $\text{Im}\chi^0(\mathbf{q}, \omega)$  at X (upper panel) and M (lower panel) for undoped LaFeAsO (green) and Land LaFeAsO<sub>0.7</sub>F<sub>0.3</sub> (red).

upper one, albeit at the M point. As we mentioned before, the undoped compound (green) exhibits a zero-energy excitation and a small but sharp feature around 0.5 eV. Upon doping, a non-vanishing energy gap is introduced at the M point and the peak at 0.5 eV is pushed to slightly higher energies, as indicated by the red arrows.

Unfortunately, we are not aware of any INS experiments for LaFeAsO with electron doping above 20% to classify the validity of bare susceptibility calculations for this and similar compounds.

## 5.4. Conclusions

In the last sections we have discussed the case of LaFeAsO with electron doping. Normally, additional electrons are incorporated in this compound by substituting oxygen with fluorine, for which the solubility is very low. If hydrogen is used instead of fluorine, however, it is possible to overdope this compound and by doing so reach the end of the superconducting dome. When such a hydrogen doping experiment was performed by Iimura *et al.* [142] they observed a two-dome structure of the superconducting phase.

Our calculations of the static bare susceptibility for the undoped parent material show the expected strong response at  $\mathbf{q}_N = (\pi, \pi, 0)$ , which is in accordance with the single-stripe antiferromagnetic order observed experimentally. We have also shown that the strength of the magnetic instability at this point decreases with increased doping. This again is consistent with the physical situation depicted in the phase diagram, i.e., a loss of the magnetic order to the benefit of an emergent superconducting phase. The static bare susceptibility, however, cannot reproduce the observed two-dome character of the superconducting phase and we can therefore not speculate on its origin.

In the second part of this chapter we presented results of dynamical bare susceptibility calculations for the undoped compound, for the 20% doped case and for 30% doping. We observe modes with vanishing energy gap originating from the  $\Gamma$  point and excitation hotspots around 1.5 eV at the X and the M point. The excitation at the X point is particularly interesting, as it gets split when the material is doped. We also detect an excitation with very low energy at the M point, whose strength decreases with increasing doping. Unfortunately, due to the missing effects of interaction in our calculations, we cannot directly compare our results with INS experiments.

*Note:* While finishing this thesis we became aware of a work by Suzuku *et al.* [151], who studied the 1111 systems with fluor and hydrogen doping in the FLEX approximation. They found that the first  $T_c$  dome originates from spin fluctuations in the  $d_{xz/yz}$  orbitals induced by Fermi nesting, and that the second dome is due to spin fluctuations enhanced by interactions of electrons of  $d_{xy}$  character, whose second nearest neighbor hoppings are larger than the nearest neighbor ones. Although we cannot comment on the results of their FLEX calculations, their findings for the first  $T_c$  dome is in agreement with our calculations.

## Chapter 6.

# Static susceptibility and Fermi surface nesting in FeSe under pressure from first-principle calculations

C. Heil , M. Aichhorn, H. Sormann, E. Schachinger, W. von der Linden

preprint available at <http://arxiv.org/abs/1210.2593> (2012)

### Abstract

In many iron-based superconductors the occurrence of superconductivity was related to nesting properties of the underlying Fermi surfaces. However, it is not clear if this picture still applies in iron-chalcogenides. In order to investigate this issue we calculate from first-principles the static susceptibility of FeSe under applied pressures, both hydrostatic and non-hydrostatic. We show that the electronic band structures are highly sensitive to the way pressure is applied and confront our theoretical results with conclusions drawn from experiments. The calculated susceptibility shows strong dependence on the way pressure is applied, with robust peaks for hydrostatic pressures and vanishing peaks in the non-hydrostatic case, whereas experimentally the critical temperature of FeSe is quite universal as function of pressure. This is clear evidence that in FeSe the evolution of the susceptibility and Fermi surface nesting cannot be related to the evolution of the critical temperature with pressure.

### 6.1. Introduction

The discovery of a new class of iron based high- $T_c$  superconductors by Kamihara *et al.* [1] has kicked off an avalanche of research in solid state physics, a lot of it dedicated to the key question of the superconducting pairing mechanism. A feature that has been agreed upon is that the parent compounds of the FeAs superconductors exhibit an antiferromagnetic (AFM) spin density wave (SDW) phase, as seen in  $LnOFeAs$  ( $Ln = La, Ce, Pr, Sm$  [4, 152, 153]) and  $AeFe_2As_2$  ( $Ae = Ba, Sr, Ca$  [6, 154, 155]), or are on the verge of it, as in  $AFeAs$  ( $A = Li, Na$  [156, 157]). In such materials, superconductivity (SC) arises or is enhanced, respectively, when this long-range magnetic order is suppressed by doping or by application of physical or chemical pressure. In this respect,

pnictide and chalcogenide compounds are much more flexible as compared to the cuprate high- $T_c$  superconductors, where the superconducting state can be reached only by doping, and intercalating layers between the copper-oxygen planes are therefore essential. This large flexibility has been underpinned by the discovery of SC in FeSe [5, 158–160], a material lacking completely the intercalated planes of the iron-pnictides. This structural simplicity and its enormous response to external pressure ( $T_c$  increases from 8 K at ambient pressure [158] to 37 K at about 7 GPa [161]) made it a popular testing ground to study mechanisms of SC in iron-based superconductors.

Theoretical studies have shown [28, 87, 162, 163] that iron chalcogenides are significantly stronger correlated than the iron pnictide materials. Since this goes hand-in-hand with the enhancement of localized magnetic moments, the applicability of the Fermi surface nesting (FN) scenario in this class of compounds has to be clarified. In that scenario, SC can be regarded as a consequence of perturbations of the AFM ordering of the parent material [16, 138, 164–167]. Often a suppression of peaks in the susceptibility is regarded as an indicator for the occurrence of SC. From the experimental side, many independent experimental studies on pressure vs.  $T_c$  phase diagrams have been published for FeSe [161, 165, 168–170]. The general consensus seems to be that  $T_c$  starts around 8 K for ambient pressure, has a maximum at about 7 GPa and decreases again for even higher pressures. While all the works mentioned above applied pressure hydrostatically, a recent study investigated how  $T_c$  changes under *non*-hydrostatical pressure [171]. It is interesting to observe that the corresponding phase diagram is quite similar, i.e. the way how pressure is applied seems to be of minor importance for SC.

In this paper we investigate by first-principle calculations the evolution of the static susceptibility [33, 79, 120] under applied pressure in FeSe. We show that non-hydrostatic pressures have a strong impact on the shape of the Fermi surface and, hence, result in a strong suppression of the peaks in the susceptibility. This is not the case for hydrostatic pressures. Since the evolution of  $T_c$  is quite universal in experiments, as discussed above, our results evidence that there is no relationship between the evolution of the susceptibility and SC whatsoever, neither positive nor negative, in FeSe. This also means that the evolution of the peaks in the susceptibility should not be taken as a criterion for the strength of SC in FeSe.

## 6.2. Method

A very useful quantity for theoretical investigations of the strength and changes of the FN is the static susceptibility matrix  $\chi^0(\mathbf{q})$  (in short  $\chi^0$ ). For a system of Bloch electrons - taking into account only the diagonal elements of this matrix - it reads in the random phase approximation

$$\chi^0(\mathbf{q}) = \frac{1}{2\pi^3} \sum_{n,m} \int_{\text{(BZ)}} d\mathbf{k} \frac{f_m(\mathbf{k}) [1 - f_n(\mathbf{k} + \mathbf{q} + \mathbf{G})]}{\epsilon_m(\mathbf{k}) - \epsilon_n(\mathbf{k} + \mathbf{q} + \mathbf{G})} |\langle m, \mathbf{k} | e^{-i\mathbf{q}\cdot\mathbf{r}} | n, \mathbf{k} + \mathbf{q} + \mathbf{G} \rangle|^2, \quad (6.1)$$

where  $\mathbf{q}$  represents a vector of the *extended* wave number space,  $n$  and  $m$  denote electron

band indices,  $\mathbf{k}$  belongs to the first Brillouin zone (BZ), and  $\epsilon_m(\mathbf{k})$  and  $f_m(\mathbf{k})$  mean the energy dispersion of the  $m$ th band and the Fermi function, respectively. The reciprocal lattice vector  $\mathbf{G}$  is defined such that  $\mathbf{k} + \mathbf{q} + \mathbf{G} \in \text{BZ}$ . We want to stress that the matrix elements  $\langle m, \mathbf{k} | e^{-i\mathbf{q}\mathbf{r}} | n, \mathbf{k} + \mathbf{q} + \mathbf{G} \rangle$  are fully included in our calculation.

FN leads to a pronounced peak of  $\chi^0$  at the nesting vector  $\mathbf{q} = \mathbf{q}_N$  due to singularities of the integrand. Many undoped parent materials of iron-based superconductors show a marked FN and consequently a maximum of  $\chi^0$  at  $\mathbf{q}_N$ . A perturbation of the crystal structure due to applied pressure or of the electronic band structure due to (electron or hole) doping is able to suppress the FN and the strong response of  $\chi^0$ . It was argued [33, 45, 172, 173] that the reduction of the collectively AFM-ordered electron spins in favor of the appearance of spin-flip processes may act as a generator for electron pairing and SC.

All results presented in this work have been obtained on the basis of non-spinpolarized DFT full-potential linearised augmented-planewave band-structure calculations using the WIEN2k package [121]. The exchange-correlation potential has been approximated by the generalized-gradient approximation GGA, and the base-centered orthorhombic crystal structure Cmma has been used. The numerical integration over the first Brillouin zone has been performed with a semi-analytical tetrahedron method. This newly developed algorithm is able to manage the very difficult integration even for  $\mathbf{q} \rightarrow 0$  with an accuracy that satisfies the relation  $\chi^0(0) = N(\epsilon_F)/\Omega_0$  numerically, where  $N(\epsilon_F)$  is the electronic density of states at the Fermi energy  $\epsilon_F$  and  $\Omega_0$  the volume of the unit cell of the crystal. Each electron wave function has been represented by about 4000 plane waves, and 52 electron bands, corresponding to an energy interval from  $-1.2$  Ry below to  $3$  Ry above the Fermi energy, have been included. Instead of the real Cmma structure with  $\tilde{a} \neq \tilde{b} \neq \tilde{c}$ , where  $\tilde{a}, \tilde{b}$  and  $\tilde{c}$  are the FeSe unit cell lattice parameters, many studies use the P4/nmm structure instead, which occurs when  $\tilde{a} = \tilde{b}$ . For a better comparison of our results we therefore inscribed our Cmma unit cell into the P4/nmm unit cell with modified lattice parameters  $a = \sqrt{\tilde{a}^2 + \tilde{b}^2}$ ,  $c = \tilde{c}$ . The momentum vectors  $\mathbf{q}$  are expressed in units of  $(\pi/a, \pi/a, \pi/c)$  throughout this work and  $\chi^0$  is presented in units  $(\text{eV} \cdot a_0^3)^{-1}$  with  $a_0$  being the Bohr radius. The lattice and unit cell parameters are taken from experiment, where we used data by Margadonna *et al.* [161] and Kumar *et al.* [138] for hydrostatic pressures, and for the non-hydrostatic case data from Uhoja *et al.* [171].

### 6.3. Results

We start the discussion of the pressure dependence with the hydrostatic case. We checked that the results based on the crystal structures reported by Kumar *et al.* [138] are essentially the same as the results based on structures reported by Margadonna *et al.* [161] In the following, we will hence show only results based on data by Kumar *et al.* In Fig. 6.1 a surface plot of the static susceptibility over the  $(q_x, q_y, 0)$ -plane for FeSe at a hydrostatic pressure of  $2.8$  GPa is presented. The dominating features are the marked peaks, indicating a strong FN of the hole pockets at the  $\Gamma$  point and the electron pockets at

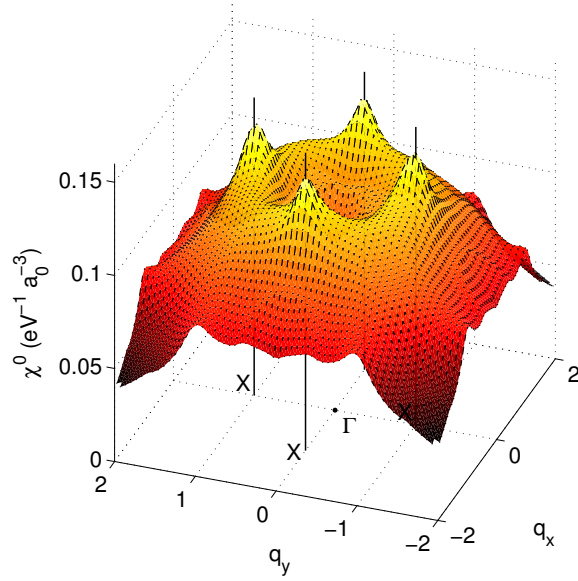


Figure 6.1.: Static susceptibility  $\chi^0$  in the  $(q_x, q_y, 0)$ -plane of FeSe at a hydrostatic pressure of 2.8 GPa. The vertical solid black lines mark the positions of the X points in the reciprocal unit cell and  $q_x, q_y$  are given in units of  $\pi/a$ .

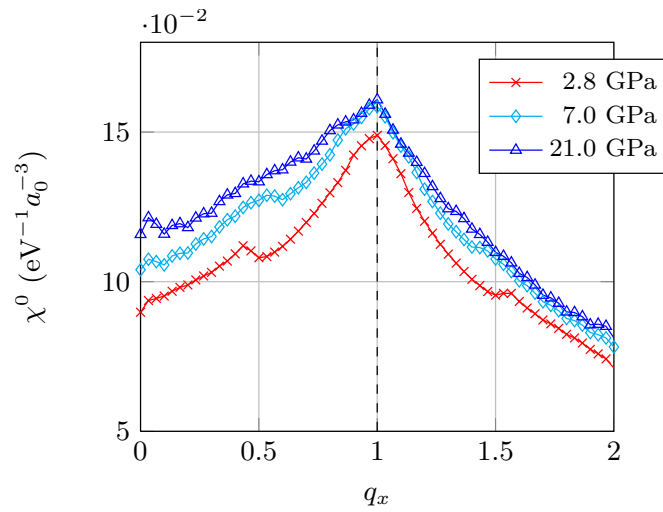


Figure 6.2.: Static susceptibility  $\chi^0$  in the  $(q_x, 0, 0)$  direction of FeSe for different hydrostatic pressures ( $q_x$  is given in units of  $\pi/a$ ). Apart from the vertical shift, due to the increasing density of states at the Fermi energy,  $\chi^0$  shows very little dependence on pressure.

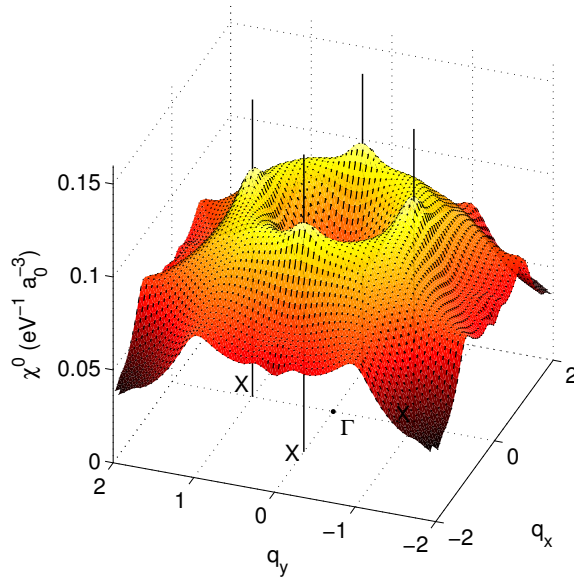


Figure 6.3.: Static susceptibility  $\chi^0$  in the  $(q_x, q_y, 0)$ -plane for FeSe at a non-hydrostatic pressure of 4 GPa. The vertical solid black lines mark the positions of the X points in the reciprocal unit cell and  $q_x, q_y$  are given in units of  $\pi/a$ .

the X points, corresponding to the FN vector  $\mathbf{q}_N = (1, 0, 0)$ . For a better quantitative discussion of the pressure dependence, we show a  $(q_x, 0, 0)$  cut of the susceptibility in Fig. 6.2. In this diagram we compare the susceptibility in the  $(1, 0, 0)$  direction for three structures at pressures 2.8 GPa (red,  $\times$ ), 7 GPa (cyan,  $\diamond$ ) and 21 GPa (blue,  $\triangle$ ). Interestingly, the three calculated profiles have a quite similar shape. They differ only by a vertical shift, reflecting the increase of  $N(\epsilon_F)$  with increasing pressure. However, the prominent peak at  $\mathbf{q}_N = (1, 0, 0)$  does not vanish with increasing pressure, leading to the conclusion that the strength of the FN is not pressure-dependent in the hydrostatic case.

The situation is different in the non-hydrostatic case, as demonstrated in Figs. 6.3 and 6.4. Here we present the static susceptibility for the compounds reported by Uhoya *et al.* [171]. Fig. 6.3 depicts the situation for 4 GPa, where the marked maxima at the X points, similar to the hydrostatic case, can still be observed. On the other hand, for the high pressure case (12.9 GPa) shown in Fig. 6.4, these maxima are reduced significantly. This change of the susceptibility is even better demonstrated in Fig. 6.5, where we depict again a  $(q_x, 0, 0)$  cut of the susceptibility. Here we compare  $\chi^0$  for the case of non-hydrostatic pressures at 4 GPa (red,  $\times$ ), 7 GPa (cyan,  $\diamond$ ) and 12.9 GPa (blue,  $\triangle$ ). For the intermediate pressure regime of 7 GPa we interpolated the structural data from Uhoya *et al.* [171] for 4 GPa and 12.9 GPa. It is known from experiments [138, 143, 161] that - in such moderate pressure regimes - the unit cell parameters change linearly with

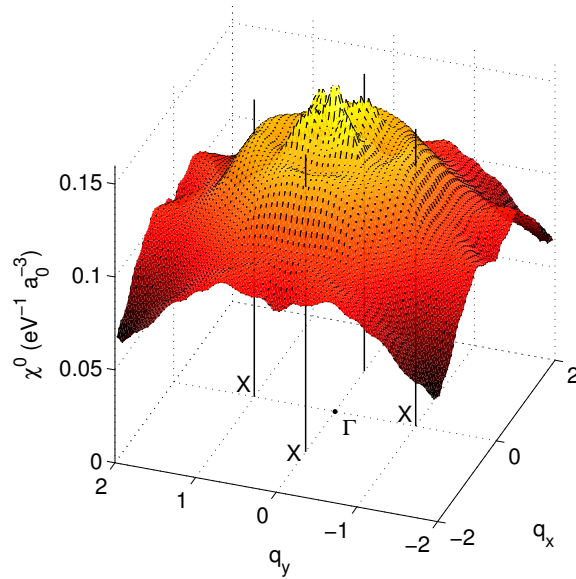


Figure 6.4.: Static susceptibility  $\chi^0$  in the  $(q_x, q_y, 0)$ -plane for FeSe at a non-hydrostatic pressure of 12.9 GPa. The vertical solid black lines mark the positions of the X points in the reciprocal unit cell and  $q_x, q_y$  are given in units of  $\pi/a$ .

pressure, supporting this approach. While the strong response at  $\mathbf{q}_N$  is still present for the cases with 4 and 7 GPa (albeit slightly reduced for the 7 GPa structure), it has vanished completely for the high pressure case. This behavior of  $\chi^0$  allows the conclusion that the FN in FeSe is rather strong for low and is reduced considerably for higher non-hydrostatic pressures.

In order to get better insight into this different FN behavior, we present in Figs. 6.6 and 6.7 the cuts of the Fermi surfaces in the  $(q_x, q_y, 0)$ -plane for low (4 GPa) and high (12.9 GPa) non-hydrostatic pressures. The different colors in these diagrams correspond to different bands, while the black dotted lines mark the edges of the unit cell in reciprocal space.

For low pressures (Fig. 6.6), it can clearly be seen that there is a marked FN, originating mainly from the interband transitions between the hole-like pockets around the  $\Gamma$  point and the electron-like pockets around the X point. Different to doping, where hole pockets shrink and electron pockets grow - or vice versa - the effect of non-hydrostatic pressures is a bit more subtle: Large pressures lead to considerable changes in the  $a/b$  lattice parameters, and as a consequence, not only the sizes of the pockets, but also their shapes are altered substantially (Fig. 6.7). In the case of low pressures the electron and hole pockets are in good approximation circular. For high pressures on the other hand, the pockets at the X points disappear completely and the Fermi surfaces at the  $\Gamma$  point are distorted to more complicated quasi-elliptical shapes. This results in a complete

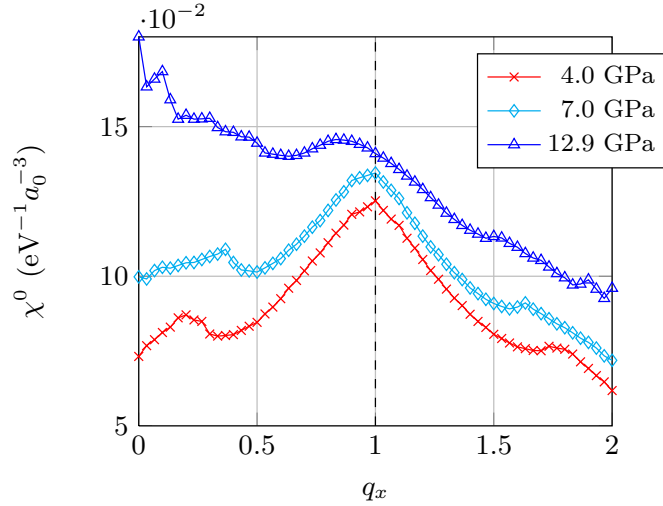


Figure 6.5.: Static susceptibility  $\chi^0$  in the  $(q_x, 0, 0)$  direction for FeSe for different non-hydrostatic pressures ( $q_x$  is given in units of  $\pi/a$ ).  $\chi^0$  shows a marked peak at the FN vector  $\mathbf{q}_N$  for the 4 GPa case, which is still present, albeit reduced, for the 7 GPa compound. At high pressures of 12.9 GPa no prominent feature can be seen.

loss of the FN vector  $\mathbf{q}_N$  and further supports our conclusion drawn from Figs. 6.3-6.5, namely, that increasing non-hydrostatic pressure causes a significant decrease of the FN: While in the 4 GPa case the nesting vector  $\mathbf{q}_N = (1, 0, 0)$  can clearly be observed, such a feature is not visible for a pressure of 12.9 GPa. We want to emphasize that the calculation of the complete susceptibility offers more detailed and reliable information about the position of the SDW-vector and the strength of the FN. This is based on the fact that  $\chi^0$  involves the integration over the whole Brillouin zone and the inclusion of the matrix elements, as can be seen in Eq. (6.1).

## 6.4. Discussions and Conclusions

The results presented above have important implications concerning the behavior of SC in FeSe. For low pressures the static susceptibility of this material exhibits a strong response at the FN vector. For higher pressure the suppression of the peak in the susceptibility depends crucially on whether pressure is applied hydrostatically or not. According to our calculations there is no visible reduction of the FN for applied hydrostatic pressures, even as large as 21 GPa. On the other hand, we observe that the FN is reduced significantly if pressure is applied non-hydrostatically, resulting in a complete suppression of the peaks at the FN vector in the susceptibility. Based on these theoretical results alone, without knowing the experimental facts, one would argue that - in the framework of FN-mediated pairing - SC in FeSe is only supported efficiently by

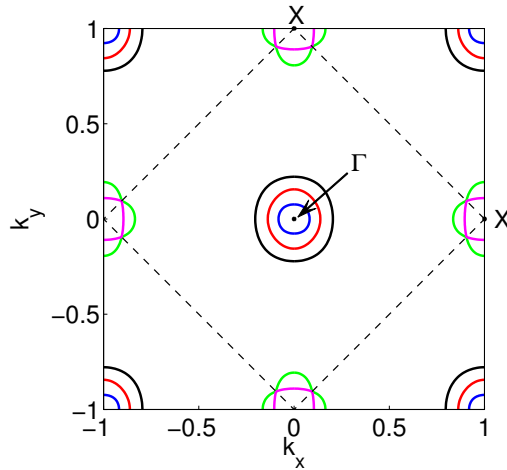


Figure 6.6.: Fermi surface  $k_z = 0$  cut for FeSe at a non-hydrostatic pressure of 4 GPa. The different colors correspond to different electron bands that cross the Fermi energy.  $k_x$  and  $k_y$  are given in units of  $\pi/a$  and the black dashed lines mark the boundaries of the reciprocal Cmma unit cell.

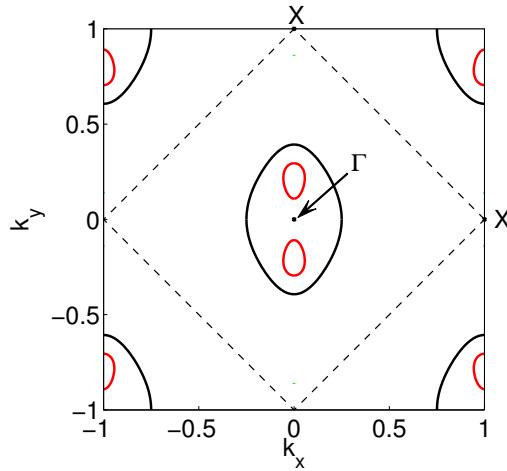


Figure 6.7.: Fermi surface  $k_z = 0$  cut for FeSe at a non-hydrostatic pressure of 12.9 GPa. The different colors correspond to different electron bands that cross the Fermi energy.  $k_x$  and  $k_y$  are given in units of  $\pi/a$  and the black dashed lines mark the boundaries of the reciprocal Cmma unit cell.

non-hydrostatic pressures. However, such a result contradicts experiments, which report a considerable increase of  $T_c$  with increasing pressure *independent* of the way pressure is applied. This shows clearly that the evolution of the theoretically calculated susceptibility and - in particular - of its peaks with pressure cannot be taken as a criterion for the evolution of  $T_c$  in this compound.

This leads to the conclusion, that SC in the FeSe compounds is not based on a weak-coupling nesting between electron and hole pockets, and therefore not mediated by spin fluctuations coming from an itinerant SDW state. In addition, recent studies have shown [174–176] that the pronounced increase of  $T_c$  with pressure cannot be explained by phononic Cooper-pairing either. In order to explain SC in FeSe in agreement with our results we argue that other mechanisms should be invoked. Since these materials obviously show enhanced electronic correlations [28, 87, 162, 163], a mechanism based on short-ranged spin fluctuations mediating between more localised magnetic moments [168, 177–179] might be promising.



## Chapter 7.

# Effect of the iron valence in the two types of layers in $\text{LiFeO}_2\text{Fe}_2\text{Se}_2$

C. Heil, L. Boeri, H. Sormann, W. von der Linden, M. Aichhorn

Physical Review B **90**, 165122 (2014)

Copyright 2014 by the American Physical Society.

### Abstract

We perform electronic structure calculations for the recently synthesized iron-based superconductor  $\text{LiFeO}_2\text{Fe}_2\text{Se}_2$ . In contrast to other iron-based superconductors, this material comprises two different iron atoms in  $3d^5$  and  $3d^6$  configurations. In band theory, both contribute to the low-energy electronic structure. Spin-polarized density functional theory calculations predict an antiferromagnetic metallic ground state with different moments on the two Fe sites. However, several other almost degenerate magnetic configurations exist. Due to their different valences, the two iron atoms behave very differently when local quantum correlations are included through the dynamical mean-field theory. The contributions from the half-filled  $3d^5$  atoms in the  $\text{LiFeO}_2$  layer are suppressed and the  $3d^6$  states from the FeSe layer restore the standard iron-based superconductor fermiology.

### 7.1. Introduction

The discovery of iron-based high- $T_c$  superconductors (FeSCs) in 2008 [1] has triggered an enormous amount of research in solid state physics, both experimental and theoretical. Since then, many new compounds have been discovered and investigated, which differ considerably in their structural details [7]. They all share a common structural motif, i.e., a square lattice of Fe atoms to which pnictogen or chalcogen atoms are tetrahedrally coordinated. In the case of pnictogen compounds, spacer layers such as layers of lanthanide oxides [153, 180, 181] or alkaline (earth) atoms [6, 157, 182] between the Fe planes ensure charge neutrality. In chalcogenide compounds, these layers are not necessary, leading to the structurally simplest iron-based superconductors FeSe and FeTe.

Recently, Lu *et al.* [183] synthesized  $\text{LiFeO}_2\text{Fe}_2\text{Se}_2$ , i.e., a FeSe compound, intercalated with  $\text{LiFeO}_2$  layers, and reported a very high critical temperature of  $T_c = 43$  K,

comparable to that of many other high- $T_c$  FeSCs, including (mol)-FeSe [1, 161, 184, 185]. Together with  $\text{Sr}_2\text{VO}_3\text{FeAs}$  [186], and rare-earth (Ce,Pr,Eu) 1111 pnictides, this is one of the few examples of a FeSC with a magnetic atom in the intercalated layers. What makes this compound special is that the magnetic atom is itself iron. The iron atoms in the  $\text{LiFeO}_2$  and FeSe layers,  $\text{Fe}_{\text{Li}}$  and  $\text{Fe}_{\text{Se}}$ , respectively, have very different properties related to their nominal charge. Since  $\text{Fe}_{\text{Li}}$  is in a  $3d^5$  configuration and therefore at half filling, correlations are very effective and may lead to a Mott-insulating state for moderate values of the Coulomb interaction  $U$  and Hund's coupling  $J$  [85].  $\text{Fe}_{\text{Se}}$ , on the other hand, is in  $3d^6$  configuration, i.e., well into the Hund's metal regime [28, 86, 94], where the correlated metallic state extends to much larger values of the Coulomb interaction  $U$ . This compound could thus provide two *qualitatively* different realizations of correlation effects due to Hund's coupling in one and the same compound.

The electronic structure of  $\text{LiFeO}_2\text{Fe}_2\text{Se}_2$  was studied in Ref. [187] with standard density functional calculations. The authors found an antiferromagnetic (AFM) ground state in which both layers are metallic, and argued that with the inclusion of local correlations the  $\text{LiFeO}_2$  plane would become insulating, while the FeSe layer would exhibit a bad metallic behavior. However, no quantitative evidence for this argument was provided.

In this paper, we study the electronic structure of  $\text{LiFeO}_2\text{Fe}_2\text{Se}_2$  *including* strong local correlations, using DFT+U [188] and DFT+DMFT calculations. We show that at the DFT level both  $\text{Fe}_{\text{Li}}$  and  $\text{Fe}_{\text{Se}}$  exhibit a strong tendency to magnetism, leading to a double-AFM ground state in which both layers are either metallic or insulating at the same time. Magnetism appears extremely fragile, with many almost-degenerate configurations competing with the ground state one. This indicates a strong tendency to a *paramagnetic* behavior, which we describe using dynamical mean field theory (DMFT). We find that in this regime the behavior of the two Fe atoms is qualitatively very different, due to the different charge state:  $\text{Fe}_{\text{Li}}$  is an incipient Mott insulator, while  $\text{Fe}_{\text{Se}}$  is fully into the Hund's metal regime. As a result,  $\text{Fe}_{\text{Li}}$  states are almost entirely removed from the Fermi level, while  $\text{Fe}_{\text{Se}}$  bands retain a strongly coherent character and form a typical FeSC Fermi surface.

This paper is organized as follows: In Sec. 7.2 we report the computational details of our calculations. Section 7.3 contains the results of our DFT and DFT+U calculations in the non-magnetic and magnetic regime. In Sec. 7.4 we present calculations including correlations within DFT+DMFT. We conclude and summarize our findings in Sec. 7.5.

## 7.2. Computational Details

According to Lu *et al.* [183]  $\text{LiFeO}_2\text{Fe}_2\text{Se}_2$  crystallizes in a simple tetragonal unit cell with  $a = b = 3.7926 \text{ \AA}$ ,  $c = 9.2845 \text{ \AA}$ , and  $\alpha = \beta = \gamma = 90^\circ$ , which belongs to the P4/nmm space group and contains one formula unit (*f.u.*). Each unit cell comprises two different types of layers: the FeSe layer common to all FeSCs, and a  $\text{LiFeO}_2$  layer, in which Li and Fe are randomly distributed on a square lattice and O atoms tetrahedrally coordinated to them. Fe atoms in the  $\text{LiFeO}_2$  -  $\text{Fe}_{\text{Li}}$  - and FeSe layers -  $\text{Fe}_{\text{Se}}$  - are inequivalent.

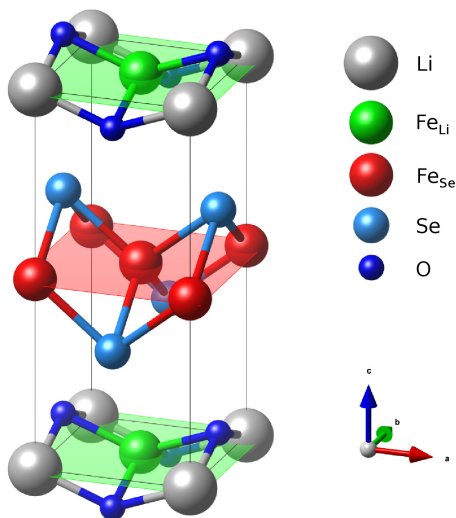


Figure 7.1.: (Color online) Nonmagnetic unit cell of  $\text{LiFeO}_2\text{Fe}_2\text{Se}_2$ . The two different iron atoms are shown with two different colors,  $\text{Fe}_{\text{Li}}$  in green and  $\text{Fe}_{\text{Se}}$  in red. The  $\text{Fe}_{\text{Li}}$  and  $\text{Fe}_{\text{Se}}$  planes are shaded in green and red, respectively.

They are shown in green and red in Fig. 7.1, respectively. For all our calculations we assumed a regular, alternating in-plane arrangement of the Li and  $\text{Fe}_{\text{Li}}$  atoms, so that Li and  $\text{Fe}_{\text{Li}}$  sit on top of  $\text{Fe}_{\text{Se}}$  atoms. In this configuration,  $\text{Fe}_{\text{Se}}$  occupies  $4e$  and Se  $8j$  Wyckoff positions with  $z = 0.6645$ ; Li and  $\text{Fe}_{\text{Li}}$  occupy  $4d$  positions, O  $8j$  positions with  $z = 0.0764$ . We want to note here that the Fe concentration in the  $\text{LiFeO}_2$  layer is only half that of the one in the FeSe layer; thus the average nearest-neighbor Fe-Fe distance in the  $\text{LiFeO}_2$  layer is a factor of  $\sqrt{2}$  larger. The FeSe tetrahedra are strongly elongated; in fact, the distance of the Se atoms from the Fe planes is  $h_{\text{Se}} \approx 1.53 \text{ \AA}$ , much larger than  $h_{\text{Se}} \approx 1.45 \text{ \AA}$  in bulk FeSe at zero pressure [161].

For all our electronic structure calculations we have employed the full-potential linearized augmented plane-wave package WIEN2k [121] using a GGA-PBE exchange-correlation functional. [147].<sup>1</sup> For the DFT+DMFT calculations we use the charge self-consistent implementation of the TRIQS toolkit. [26, 189, 190] As impurity solver we employ continuous-time quantum Monte-Carlo. [191–193]

<sup>1</sup>RKmax was set to 7.0 and the following MT radii were chosen:  $\text{RMT}(\text{Li}) = 1.90a_0$ ,  $\text{RMT}(\text{Fe}_{\text{Li}}) = 2.02a_0$ ,  $\text{RMT}(\text{Fe}_{\text{Se}}) = 2.02a_0$ ,  $\text{RMT}(\text{Se}) = 2.15a_0$  and  $\text{RMT}(\text{O}) = 1.79a_0$ . For the reciprocal  $k$ -space integration we took 720  $k$ -points in the irreducible wedge.

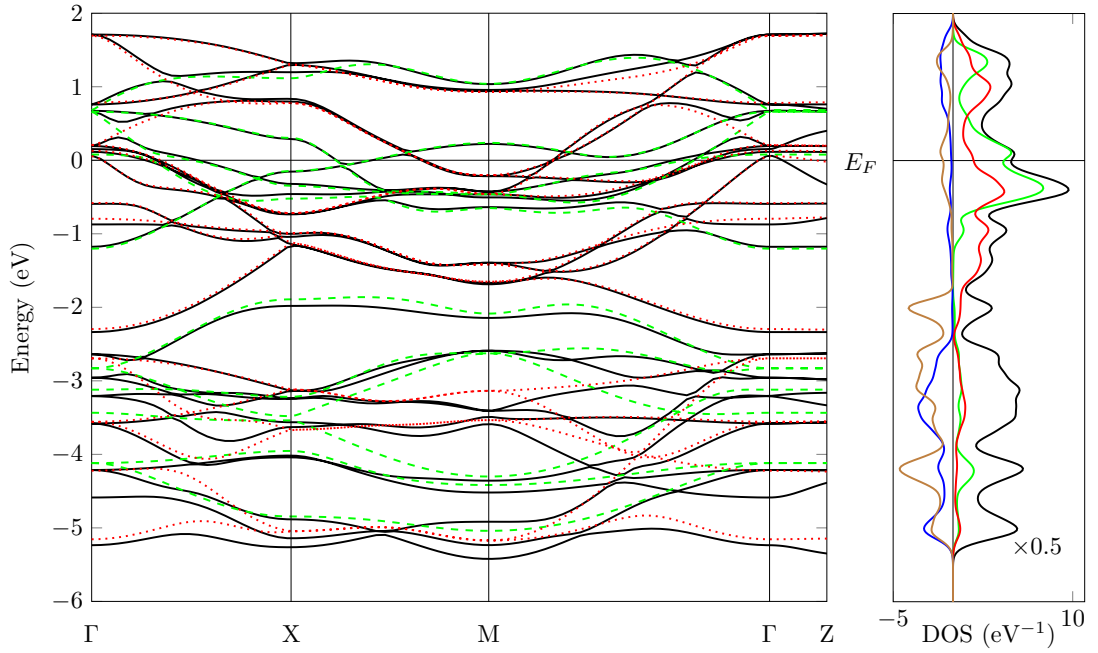


Figure 7.2.: (Color online) Left: DFT band structure of nonmagnetic  $\text{LiFeO}_2\text{Fe}_2\text{Se}_2$  (solid black lines), isolated  $\text{LiFeO}_2$  (dashed green lines), and isolated  $\text{FeSe}$  (red dotted lines). Right: (p)DOS of nonmagnetic  $\text{LiFeO}_2\text{Fe}_2\text{Se}_2$ . The pDOS of  $\text{Fe}_{\text{Li}}$  is shown in green and the pDOS of  $\text{Fe}_{\text{Se}}$  in red. The contributions from Se and O are plotted in blue and brown, respectively, on the negative axis. The units are  $\text{st}/\text{eV}$  (two spins) per atom for the pDOS; the total DOS is in  $\text{st}/\text{eV}$  f.u. (two spins) and has been rescaled by a factor of 2 to improve the readability of the figure.

### 7.3. Electronic Structure

Figure 7.2 shows the non-magnetic DFT bandstructure (left panel) and the (partial) density of states (pDOS) of  $\text{LiFeO}_2\text{Fe}_2\text{Se}_2$  (right panel), in an energy range of  $[-6, 2]$  eV around the Fermi level, which is chosen at zero energy. The bandwidth of  $\text{Fe}_{\text{Li}}$  is about 2 eV, which is due to the larger average Fe-Fe distance in this layer, and that of  $\text{Fe}_{\text{Se}}$  3.5 eV. States at the Fermi level have mostly  $\text{Fe}_{\text{Li}}$  and  $\text{Fe}_{\text{Se}}$  partial character, while ligand (O, Se) bands lie lower in energy. The peak at approximately  $-2$  eV has mainly O character and it is clearly seen that around  $-4.1$  eV there is a strong hybridization between  $\text{Fe}_{\text{Li}}$  and O, while  $\text{Fe}_{\text{Se}}$  and Se show hybridization between  $-3.9$  eV and  $-2.5$  eV. The DOS at the Fermi energy is  $N(E_F) = 7.7 \text{ eV}^{-1} \text{ f.u.}$  per spin, i.e., above the Stoner criterion.

The left panel of Fig. 7.2 shows the corresponding electronic structure along high-

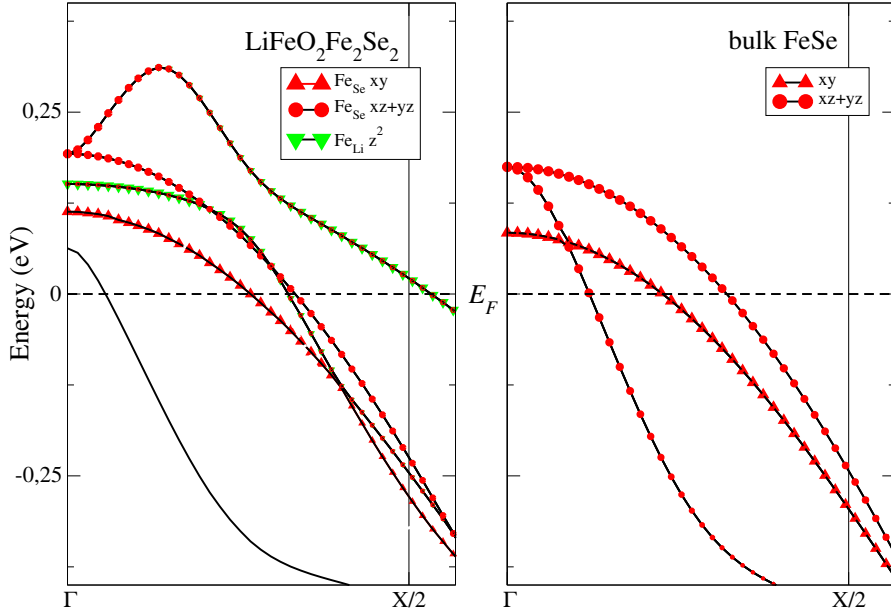


Figure 7.3.: (Color online) Left: Zoom of Fig. 7.2 with the bands of  $\text{LiFeO}_2\text{Fe}_2\text{Se}_2$  in solid black. The dominant character of the  $\text{LiFeO}_2\text{Fe}_2\text{Se}_2$  bands is shown by the symbols. The band without special character markers is a mixture of all characters. Right: Band structure of bulk FeSe calculated for the experimental crystal structure at ambient pressure from Ref. [161].

symmetry lines in the Brillouin zone (BZ). Our results agree with those of Ref. [187]. In addition to the bands of the full compound (solid black lines), we also show the bands of the *isolated*  $\text{LiFeO}_2$  (dashed green lines) and FeSe layers (dotted red lines) in the original unit cell. In order to align the bands, we had to shift the bands of isolated  $\text{LiFeO}_2$  down by  $-0.1$  eV, which corresponds to a charge transfer of  $0.35 e^-$  from FeSe to  $\text{LiFeO}_2$  layers. Except for an increased dispersion of the FeSe bands along the  $\Gamma$ -Z direction, the low-energy band structure of  $\text{LiFeO}_2\text{Fe}_2\text{Se}_2$  coincides almost exactly with that of the isolated layers.

Due to the strong elongation of the Fe-Se tetrahedra and to hybridization with the  $\text{LiFeO}_2$  states, the fermiology of  $\text{LiFeO}_2\text{Fe}_2\text{Se}_2$  is quite different compared to typical iron-chalcogenide SCs. In Fig. 7.3, we show the low-energy bandstructure of  $\text{LiFeO}_2\text{Fe}_2\text{Se}_2$  and bulk FeSe decorated with the dominant orbital characters along a short section of the  $\Gamma$ -X path. This permits us to highlight and understand the difference in the shape of the hole pockets.

The  $\text{FeSe}$   $3d_{xy}$  band close to the Fermi energy (red triangles in Fig. 7.3) has the same dispersion in  $\text{LiFeO}_2\text{Fe}_2\text{Se}_2$  and bulk FeSe. On the other hand, the remaining hole bands have very different dispersions in the two compounds. In particular, one of the doubly

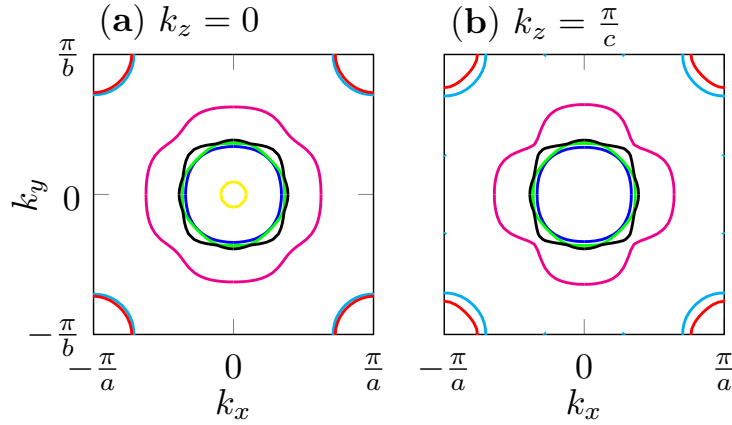


Figure 7.4.: (Color online) Top view of the Fermi surface at  $k_z = 0$  (left) and  $k_z = \pi/c$  (right) of non-magnetic  $\text{LiFeO}_2\text{Fe}_2\text{Se}_2$ . Different colours indicate different bands.

degenerate  $d_{xz/yz}$  bands which form the hole pockets in most FeSCs is pushed up in  $\text{LiFeO}_2\text{Fe}_2\text{Se}_2$  due to the large  $h_{\text{Se}}$ , [45, 139] and is further modified by hybridizations with  $\text{Fe}_{\text{Li}} d_{z^2}$ . These hybridizations are so strong that when this band crosses  $E_F$ , it has mostly  $\text{Fe}_{\text{Li}}$  character. As one  $d_{xz/yz}$  band is removed from the Fermi surface, another band appears at  $E_F$ . This new band is mainly a mixture of  $\text{Fe}_{\text{Se}} d_{xz/yz}$  and  $\text{Fe}_{\text{Li}} d_{z^2}$ .

Figure 7.4 shows the Fermi surface of  $\text{LiFeO}_2\text{Fe}_2\text{Se}_2$  in the  $k_z = 0$  and the  $k_z = \pi/c$  planes. In this figure, different colors indicate different bands and are not related to orbital character. The smallest hole pocket has a three-dimensional cigar shape and is located around the  $\Gamma$  point [yellow line in Fig. 7.4(a) and not present in Fig. 7.4(b)]. The other hole pockets are shown in blue ( $\text{Fe}_{\text{Se}} d_{xy}$ ), green ( $\text{Fe}_{\text{Li}}/\text{Fe}_{\text{Se}}$ ), and black ( $\text{Fe}_{\text{Se}} 3d_{xz+yz}$ ). The electron pockets at the M points, shown in cyan and red, have mostly  $d_{xz/yz/xy}$  character and are much less affected by hybridization and changes in selenium height  $h_{\text{Se}}$ . In addition to the FeSe pockets, the  $\text{LiFeO}_2$  layer provides an additional hole pocket in the middle of the Brillouin zone (magenta lines in Fig. 7.4), which has a considerable three-dimensional character.

The charge transfer between the layers and the presence of the additional  $\text{LiFeO}_2$ -derived band are quite visible also in the susceptibility  $\chi^0$ , plotted in Fig. 7.5. Details of the calculations are given in Ref. [80]. The susceptibility of the full compound, shown as a black solid line, grows towards the border of the Brillouin zone (X-M line), and shows a dip around the M point, in contrast to most FeSCs, which show a clear maximum at M. Indeed, the isolated FeSe layer (red curve) shows a well-defined peak at this point. The  $\text{LiFeO}_2$  layer (green solid line) has an even larger susceptibility, with a dip around the M point. In order to explain the full susceptibility it is not sufficient to sum the contributions from the isolated layers, which still shows a maximum around the M point

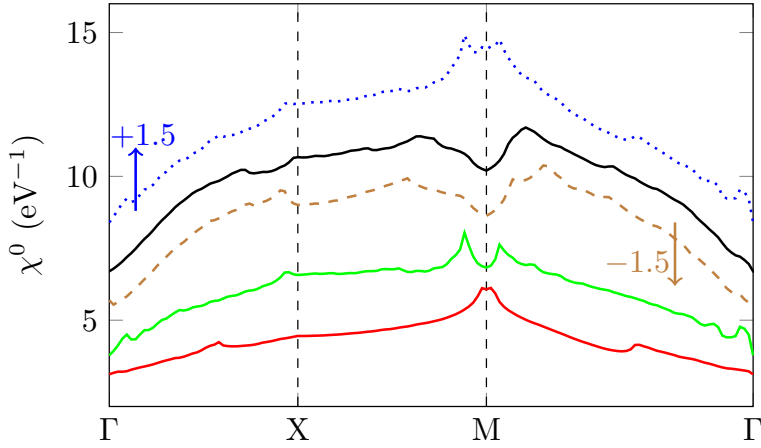


Figure 7.5.: (Color online) Static bare susceptibility  $\chi^0$  for isolated FeSe (red), isolated LiFeO<sub>2</sub> (green), and the full LiFeO<sub>2</sub>Fe<sub>2</sub>Se<sub>2</sub> compound (black). The dotted blue line results when summing  $\chi^0$  for the two isolated layers. The dashed brown line depicts the summed  $\chi^0$  of the isolated layers, where we performed a rigid-band shift in order to account for the charge transfer. All susceptibilities are given per spin and for all Fe atoms in the respective unit cells. The blue and brown curves have been shifted up (down) by 1.5 eV<sup>-1</sup> to improve readability. For details on the susceptibility calculation see Ref. [80].

(dotted blue curve). In order for the sum of the two layers to reproduce the susceptibility, the Fermi levels have to be adjusted as done in Fig. 7.2. This results in the dashed brown curve of Fig. 7.5 and highlights the occurrence of charge transfer in this material.

We now discuss results of spin-polarized DFT calculations for the magnetically ordered states, which are shown in Tables 7.1 and 7.2. We considered the most important magnetic configurations for the isolated layers and the full compound. In Table 7.1 we show the results for the magnetic moments ( $m_{\text{Fe}}$ ) and the stabilization energy per Fe atom ( $\Delta E$ ) for ferromagnetic (fm), checkerboard (cb), single stripe (ss), and double stripe (ds) configurations for the isolated layers. In isolated LiFeO<sub>2</sub> we find that the cb order is the one with the lowest energy, with an energy difference of 221 meV from the ss and 335 meV from the fm configuration. In the isolated FeSe compound the ss magnetic order is the most favourable one, separated from the cb order by 53 meV and from the ds order by 141 meV. Fe<sub>Se</sub> and Fe<sub>Li</sub> have different magnetic moments; the filling of the atoms implies a saturation moment of 4 and 5  $\mu_B$ , respectively. In fact, we find that  $m$  of Fe<sub>Se</sub> is 2.4  $\mu_B$ <sup>2</sup>, while the magnetic moment of Fe<sub>Li</sub> in LiFeO<sub>2</sub> is  $\sim 3.6 \mu_B$ . These values are almost independent of the magnetic ordering pattern, both in the isolated layers and in the full compound.

<sup>2</sup>This is in line with DFT calculations for other FeSCs in  $d^6$  configuration [16, 28]. This larger  $m(\text{Fe}_{\text{Se}})$  is a consequence of the large Se height.

Table 7.1.: Energies (with respect to the non-magnetic configuration) and magnetic moments of isolated  $\text{LiFeO}_2$   $m(\text{Fe}_{\text{Li}})$  and isolated  $\text{FeSe}$   $m(\text{Fe}_{\text{Se}})$  for ferromagnetic (fm), checker-board (cb), single stripe (ss), and double stripe (ds) magnetic configurations.

isolated $\text{LiFeO}_2$	$\Delta E/\text{Fe}$ (meV)	$m(\text{Fe}_{\text{Li}})$ ( $\mu_B$ )
fm	-1358.12	3.79
<b>cb</b>	<b>-1693.55</b>	<b>3.57</b>
ss	-1472.59	3.55
isolated $\text{FeSe}$	$\Delta E/\text{Fe}$ (meV)	$m(\text{Fe}_{\text{Se}})$ ( $\mu_B$ )
fm	-274.56	2.38
cb	-511.29	2.29
<b>ss</b>	<b>-564.28</b>	<b>2.51</b>
ds	-423.70	2.53

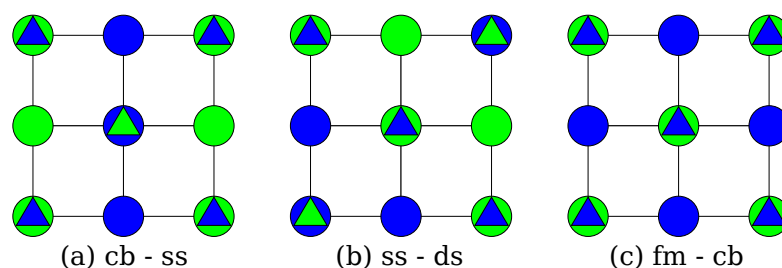


Figure 7.6.: (Color online) Top view of the Fe lattices in  $\text{LiFeO}_2\text{Fe}_2\text{Se}_2$  for the three most preferable magnetic configurations in terms of energy. The circles represent the  $\text{Fe}_{\text{Se}}$  and the triangles  $\text{Fe}_{\text{Li}}$ . Blue signifies an up-spin on that particular Fe atom and green a down-spin.

Table 7.2.: Energies (with respect to the nonmagnetic configuration) and magnetic moments of  $\text{LiFeO}_2\text{Fe}_2\text{Se}_2$  in different magnetic configurations (compare with Fig. 7.6).

$\text{LiFeO}_2\text{Fe}_2\text{Se}_2$	$\Delta E/\text{Fe}$ (meV)	$m(\text{Fe}_{\text{Li}})$ ( $\mu_B$ )	$m(\text{Fe}_{\text{Se}})$ ( $\mu_B$ )
fm - fm	-247.90	3.71	1.77
<b>cb - ss</b>	<b>-738.25</b>	<b>3.55</b>	<b>2.40</b>
ss - ds	-655.25	3.60	2.38
fm - cb	-575.29	3.81	2.21

Table 7.2 reports the most stable configurations for the full compound; the corresponding patterns are also shown in Fig. 7.6. Note that, since the two Fe sublattices are rotated by  $45^\circ$  with respect to each other, and the reciprocal unit cell of the  $\text{Fe}_{\text{Li}}$  sublattice is smaller, we have  $\mathbf{Q}_{\text{cb,ss}} = (\pi, \pi, 0)$ ,  $\mathbf{Q}_{\text{ss,ds}} = (\pi, 0, 0)$ , and  $\mathbf{Q}_{\text{fm,cb}} = (2n\pi, 0, 0)$ ; i.e., the most stable configurations are those in which the ordering vectors of the two sublattices are commensurate. In particular, we find that the configuration with the lowest energy is the one where the  $\text{Fe}_{\text{Li}}$  have *cb* order and the  $\text{Fe}_{\text{Se}}$  are aligned in an *ss* way [see Fig. 7.6(a)]. This is in agreement with what was reported by Liu *et al.* [187]. The magnetic coupling *between* the  $\text{FeSe}$  and  $\text{LiFeO}_2$  planes is extremely weak; indeed, we find that an AFM alignment of the spins along the  $z$  direction is slightly favorable, but the energy difference from the FM case is  $\lesssim 3$  meV. In addition to the configurations reported in the table, we also found many metastable ones, indicating a very fragile nature of magnetism and a strong tendency to magnetic fluctuations in this compound.

In all the cases we considered, both layers in  $\text{LiFeO}_2\text{Fe}_2\text{Se}_2$  are metallic in spin-polarized DFT. Panel (b) of Fig. 7.7 depicts the total and partial DOS of  $\text{LiFeO}_2\text{Fe}_2\text{Se}_2$  in the *cb-ss* configuration, compared with the non-magnetic one (a). The figure clearly shows a considerable depletion of the spectral weight at the Fermi level in both layers, but both  $\text{Fe}_{\text{Se}}$  (red) and  $\text{Fe}_{\text{Li}}$  (green) contribute states at the Fermi level. Liu *et al.* [187] have argued that a small Coulomb interaction  $U$  would be sufficient to open a gap at the Fermi level for  $\text{Fe}_{\text{Li}}$ , but not for  $\text{Fe}_{\text{Se}}$ . To check this hypothesis, we performed DFT+ $U$  calculations for several values of  $U$ , and found that a gap opens *simultaneously* in the two layers, for values of  $U > 2$  eV. A calculation for  $U = 2.7$  eV is reported in panel (c) of Fig. 7.7, and shows fully developed gaps for both layers.

In Fig. 7.8 we plot the values of the magnetic moments obtained in DFT+ $U$  calculations. The results for the full compound are shown as black symbols; they almost perfectly match those obtained for the isolated layers, shown in red and green, respectively, confirming the small coupling between the two layers. Note that  $U$  in this figure ranges from  $-7$  to  $7$  eV; positive values of  $U$  have a clear physical meaning, while “negative  $U$ ” DFT+ $U$  calculations have been introduced in the early days of FeSCs as a phenomenological way to simulate the reduction of the magnetic moment due to spin fluctuations [194]. We will use them in this context only to visually characterize how robust the magnetism is.

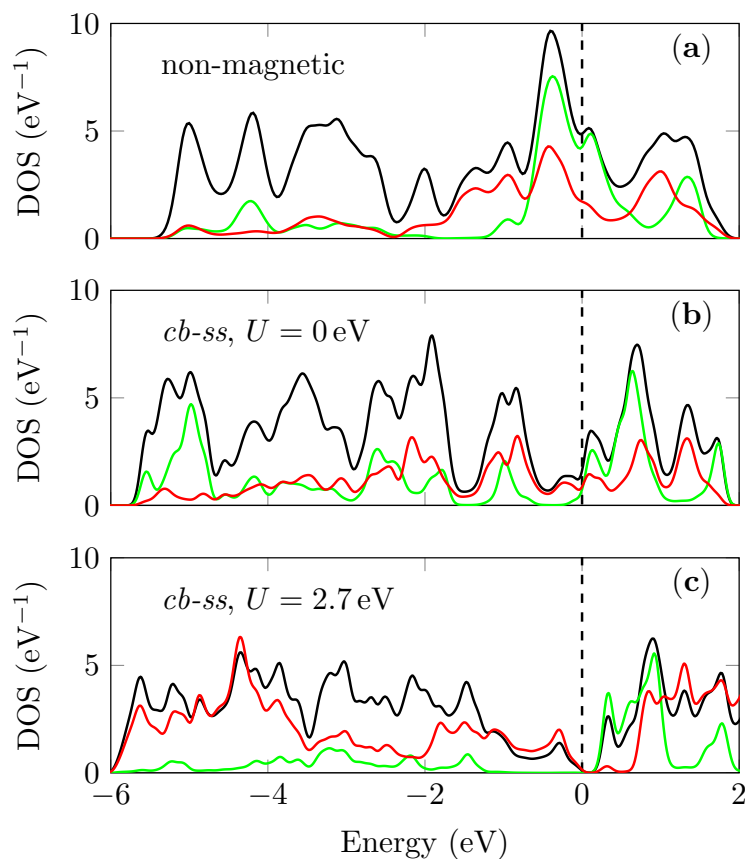


Figure 7.7.: (Color online) (a): (p)DOS of non-magnetic  $\text{LiFeO}_2\text{Fe}_2\text{Se}_2$ . The total DOS is shown in black and the pDOS of  $\text{Fe}_{\text{Li}}$  in green and of  $\text{Fe}_{\text{Se}}$  in red (same as Fig. 7.2). (b): (p)DOS of cb-ss  $\text{LiFeO}_2\text{Fe}_2\text{Se}_2$ . The total DOS is shown in black and the pDOS of  $\text{Fe}_{\text{Li}}$  in green and of  $\text{Fe}_{\text{Se}}$  in red, where we summed over majority and minority spins. (c): (p)DOS of cb-ss  $\text{LiFeO}_2\text{Fe}_2\text{Se}_2$  and  $U = 2.7$  eV. Otherwise the same as (b). Units are the same as in Fig. 7.2.

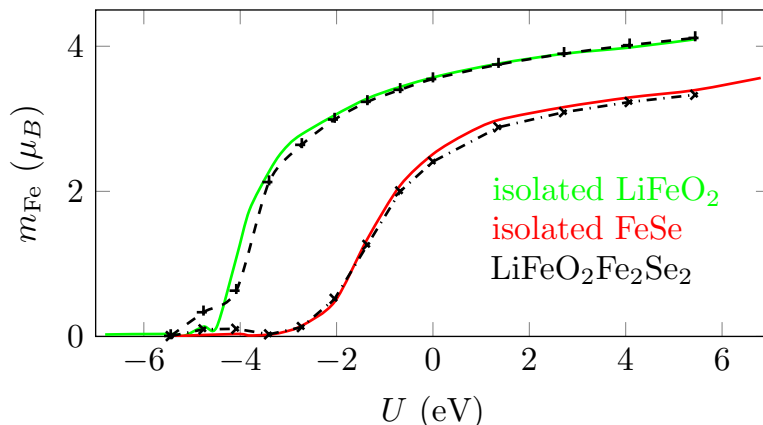


Figure 7.8.: (Color online) Magnetic moment of Fe in ss isolated FeSe (red), cb isolated LiFeO<sub>2</sub> (green) and of Fe<sub>Li</sub> (dotted black, +) and Fe<sub>Se</sub> (dash-dotted black, ×) in cb-ss LiFeO<sub>2</sub>Fe<sub>2</sub>Se<sub>2</sub>.

Several observations are in place at this point: the saturation values are clearly different for LiFeO<sub>2</sub> and FeSe, but they are not reached for  $U = 7$  eV, indicating that charge fluctuations are important in both compounds. Magnetism is much more robust in LiFeO<sub>2</sub>, since it takes much larger negative values of  $U$  to suppress it; however, the suppression is much faster, once the critical  $U$  is approached. It is possible that in the full compound the effective value of the Coulomb interaction is different in the two layers, due to the different nature of the ligands and different Fe-Fe distance. However, in order to recover (within DFT+U) a solution with no long-range magnetic order in the FeSe layer and an insulating LiFeO<sub>2</sub> layer it would be necessary to assume negative  $U$  values for Fe<sub>Se</sub> and positive values for Fe<sub>Li</sub>. This indicates that DFT+U is not able to describe this system consistently. An alternative description, which takes into account the dynamical nature of correlations, is given in the following section.

## 7.4. Correlated electronic structure

As mentioned in the beginning, the two iron atoms have very different properties related to their nominal charge. For a half-filled atomic shell, as in Fe<sub>Li</sub>, the Hund's rule coupling enhances correlation effects resulting in an insulating behavior, whereas off half filling, as in Fe<sub>Se</sub>, Hund's metallicity (small coherence scale but no Mott transition) shows up [28, 85, 86]. Since in LiFeO<sub>2</sub>Fe<sub>2</sub>Se<sub>2</sub> we have iron atoms with the two valences *in one single compound*, it is interesting to study their response to correlations in DMFT, and to see whether the general arguments given above hold here.

For the band structure calculations, we again use the WIEN2k code package. For the treatment of correlations we apply the continuous-time quantum Monte Carlo technique in the hybridization expansion formulation [191, 192], as implemented in the TRIQS

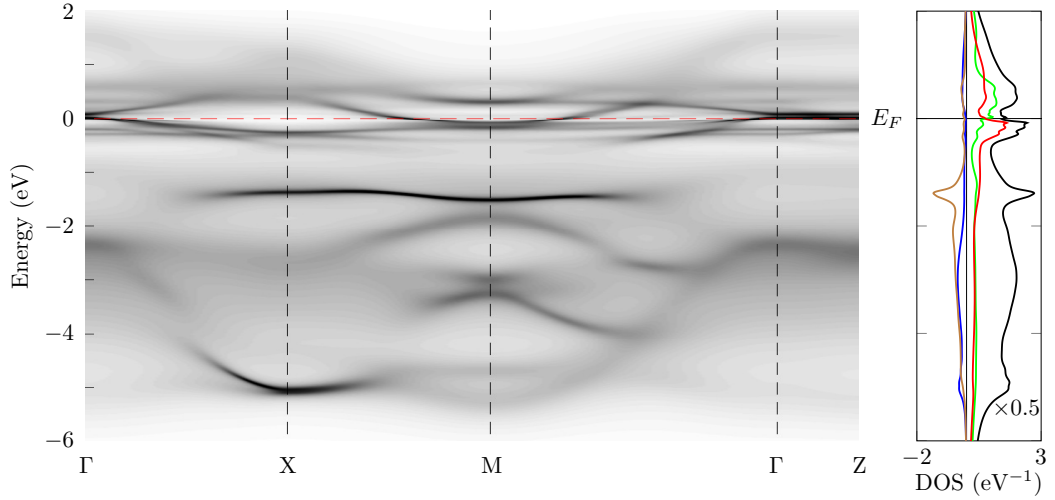


Figure 7.9.: (Color online) Left: DFT+DMFT spectral function of paramagnetic  $\text{LiFeO}_2\text{Fe}_2\text{Se}_2$  for  $U = 4 \text{ eV}$  and  $J = 0.9 \text{ eV}$ . Right: DFT+DMFT DOS of paramagnetic  $\text{LiFeO}_2\text{Fe}_2\text{Se}_2$  for the same  $U$  and  $J$  parameters. The pDOS of  $\text{Fe}_{\text{Li}}$  is shown in green and the pDOS of  $\text{Fe}_{\text{Se}}$  in red. The contributions from Se and O are plotted on the negative axis and are displayed in blue and brown, respectively. For the definition of units, see Fig. 7.2.

package [189, 193]. We use full charge self-consistency [190], as well as spin-flip and pair-hopping terms in the local Hamiltonian [195]. Wannier functions are constructed from Fe  $d$ , Se  $p$ , and O  $p$  states within an energy window of  $[-6, 2.5] \text{ eV}$ . Consistent with previous work on bulk FeSe [87] we choose  $U = 4 \text{ eV}$  and  $J = 0.9 \text{ eV}$  as interaction values, for both  $\text{Fe}_{\text{Li}}$  and  $\text{Fe}_{\text{Se}}$  atoms.

The spectral function and the (p)DOS of paramagnetic  $\text{LiFeO}_2\text{Fe}_2\text{Se}_2$  can be seen in Fig. 7.9. The left panel clearly shows a shrinking of the bandwidth of the bands around the Fermi level and that excitations become incoherent already at rather low binding energies of around  $0.4 \text{ eV}$ . From  $-5.5 \text{ eV}$  to  $-2 \text{ eV}$  the bands have mainly O and Se character, with only very little Fe contributions. The sharp peak around  $-1.4 \text{ eV}$  has solely O character.

In order to disentangle the effect of correlations on  $\text{Fe}_{\text{Li}}$  and  $\text{Fe}_{\text{Se}}$  atoms we show a close-up of the spectral function around the Fermi level in Fig. 7.10. The contributions from  $\text{Fe}_{\text{Li}}$  to the spectral function are drawn in green, while the  $\text{Fe}_{\text{Se}}$  bands are shown in black. It is immediately clear that the sharp features in the band structure, corresponding to well-defined quasiparticles, stem solely from the  $\text{Fe}_{\text{Se}}$  atom, which has a  $3d^6$  configuration and is hence in the Hund's metallic regime. In particular, when comparing with the DFT band structure (Fig. 7.2, redrawn in Fig. 7.10 as white lines) one can easily see that correlations remove all coherent contributions of the  $\text{Fe}_{\text{Li}}$  atom to the low-energy band structure. The only contributions from  $\text{Fe}_{\text{Li}}$  that survive in the vicinity of  $E_F$  are

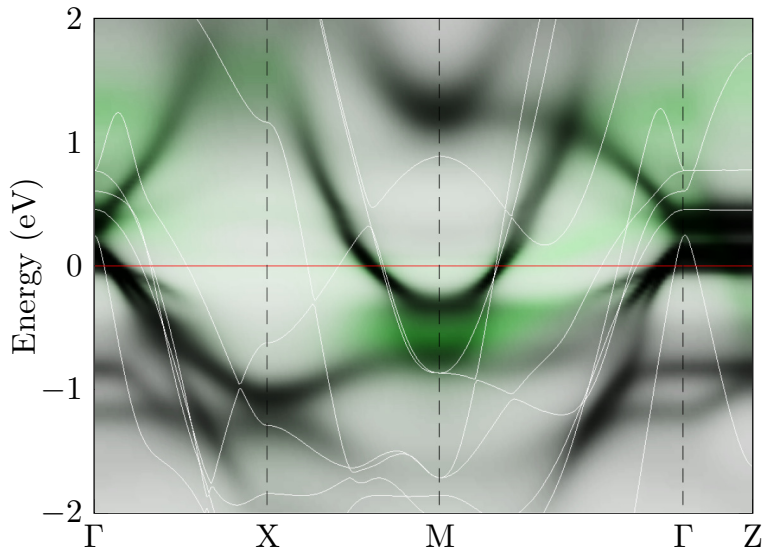


Figure 7.10.: (Color online) DFT+DMFT spectral function of paramagnetic  $\text{LiFeO}_2\text{Fe}_2\text{Se}_2$  for  $U = 4\text{ eV}$  and  $J = 0.9\text{ eV}$ . The  $\text{Fe}_{\text{Li}} 3d_{z^2}$  contributions are drawn in green and the DFT band structure is overlaid in white.

at the  $\Gamma$  and M points and are of  $3d_{z^2}$  character. They have, however, very incoherent character and are thus heavily smeared out. The remaining bands from  $\text{Fe}_{\text{Se}}$  restore a very familiar picture of the Fermi surface topology: three hole pockets at the  $\Gamma$  point and two electron pockets near the M points.

The  $\text{Fe}_{\text{Se}}$  orbital character of the bands is shown in Fig. 7.11. While the  $\text{Fe}_{\text{Se}} 3d_{z^2}$  has distinct features exclusively below the Fermi energy and the  $\text{Fe}_{\text{Se}} 3d_{x^2+y^2}$  contributes only slightly to the middle hole pocket, the main parts of the Fermi surface come from  $\text{Fe}_{\text{Se}} 3d_{xy}$  and  $3d_{xz/yz}$ . The outer hole pocket has almost only  $\text{Fe}_{\text{Se}} 3d_{xy}$  character, while the two inner hole pockets have  $3d_{xz/yz}$  character. The electron pocket at the M point is a combination of those two, with  $3d_{xz/yz}$  being the stronger one. The mass enhancements of these orbitals are between  $\sim 2$  for the  $e_g$  orbitals, 2.8  $d_{xz/yz}$ , and 3.2 for  $d_{xy}$ . Again, let us stress that there is no coherent contribution from the  $\text{Fe}_{\text{Li}}$  atom to the bands forming the Fermi surface.

It is interesting to compare our band structure with that of bulk FeSe. In Ref. [87] this band structure is shown and reveals a striking similarity with our compound here. In agreement with bulk FeSe [87] we have 3 hole pockets at the  $\Gamma$  point, where the outermost pocket is of dominantly  $d_{xy}$  character. In both compounds we have orbital-dependent mass renormalization, with the  $d_{xy}$  being the most heavy orbital.

However, differently from what was argued based on DFT+U calculations [187], we do not find a strict Mott insulator for the  $\text{LiFeO}_2$  layer, when the interaction values

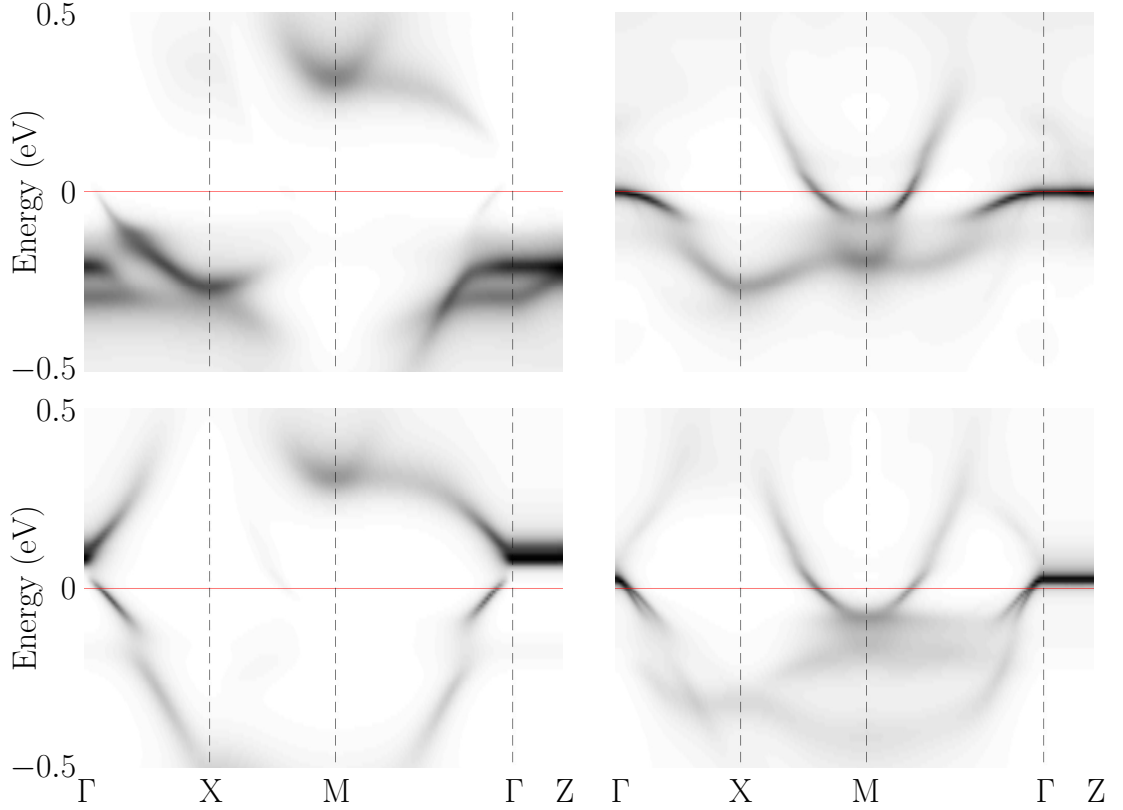


Figure 7.11.: (Color online) Contributions of  $\text{Fe}_{\text{Se}}$  to the spectral function of paramagnetic  $\text{LiFeO}_2\text{Fe}_2\text{Se}_2$  for  $U = 4 \text{ eV}$  and  $J = 0.9 \text{ eV}$  separated into orbital contributions. Top left:  $\text{Fe}_{\text{Se}} 3d_{z^2}$  orbital, top right:  $\text{Fe}_{\text{Se}} 3d_{x^2+y^2}$ , bottom left:  $\text{Fe}_{\text{Se}} 3d_{xy}$ , bottom right:  $\text{Fe}_{\text{Se}} 3d_{xz+yz}$ .

are taken as  $U = 4.0 \text{ eV}$  and  $J = 0.9 \text{ eV}$ . Instead,  $\text{Fe}_{\text{Li}}$  is in a strongly orbital-selective Mott regime [28, 88, 89, 196], with 4 out of 5 orbitals being insulating, and only one (the  $d_{z^2}$ ) with some finite, but very incoherent, weight at zero energy. An increase of the interaction values for  $\text{Fe}_{\text{Li}}$  to  $U = 6 \text{ eV}$  and  $J = 1.0 \text{ eV}$ , however, results in the suppression of also the  $\text{Fe}_{\text{Li}} d_{z^2}$  states from the Fermi surface. We relate this to the fact that a completely incoherent state can be reached with not too large values for the interaction parameters due to the atomic configuration (half-filled) of the  $\text{Fe}_{\text{Li}}$  atom.

However, as already discussed above, there is some intrinsic charge transfer from  $\text{Fe}_{\text{Se}}$  to  $\text{Fe}_{\text{Li}}$  in this compound. Calculating the charge of the iron atoms from DFT, using  $d$ -only Wannier functions, gives 5.12 electrons for  $\text{Fe}_{\text{Li}}$ , which is slightly above the integer value for half filling. That means that correlations have to overcome this small charge transfer and push the  $\text{Fe}_{\text{Li}}$  closer to half filling, before a complete suppression of the  $\text{Fe}_{\text{Li}}$  contributions can take place.

## 7.5. Conclusions

We presented calculations for the electronic and magnetic behavior of the recently synthesized Fe-based superconductor  $\text{LiFeO}_2\text{Fe}_2\text{Se}_2$  using first-principles DFT methods and DFT+DMFT calculations.

The most favourable magnetic configuration in DFT has checkerboard order in the  $\text{LiFeO}_2$  and single stripe order in the FeSe layer. When correlations in the framework of DFT+U are included, the magnetic moments of  $\text{Fe}_{\text{Li}}$  and  $\text{Fe}_{\text{Se}}$  react very differently to the Coulomb interaction  $U$ . While  $m(\text{Fe}_{\text{Li}})$  of the  $\text{LiFeO}_2$  layer is robust over a wide range of interactions and breaks down at a negative  $U$  of  $-4\text{ eV}$  in a sharp transition, the moment  $m(\text{Fe}_{\text{Se}})$  of the FeSe layer changes rather smoothly with  $U$ . We find that the pDOS of  $\text{Fe}_{\text{Li}}$  and  $\text{Fe}_{\text{Se}}$  of cb-ss  $\text{LiFeO}_2\text{Fe}_2\text{Se}_2$  have states at the Fermi energy for  $U < 2\text{ eV}$ , while for  $U > 2\text{ eV}$  this compound is fully gapped, in contrast to previous reports [187].

We also observed that there are many magnetic configurations that are very close in energy to the ground state. This means that the spins are able to fluctuate as the magnetic configuration of the whole compound can change easily.

The nonmagnetic DFT electronic band structure is much richer compared to other FeSCs, due to the presence of  $\text{LiFeO}_2$ -derived states at the Fermi level. However, the picture is strongly modified when including correlation effects by means of DFT+DMFT. Almost all contributions from the intercalated  $\text{Fe}_{\text{Li}}$  in the  $\text{LiFeO}_2$  are removed from the vicinity of the Fermi energy with the exception of the  $\text{Fe}_{\text{Li}} 3d_{z^2}$  band. This has, however, a much smaller and incoherent weight than the contributions from  $\text{Fe}_{\text{Se}}$ , which means that the low-energy physics of  $\text{LiFeO}_2\text{Fe}_2\text{Se}_2$  is governed by the  $\text{Fe}_{\text{Se}}$  of the FeSe layer. This low-energy electronic structure, stemming from  $\text{Fe}_{\text{Se}}$ , is very similar to what was found for bulk FeSe [87]. Three hole pockets are located in the vicinity of the  $\Gamma$ -point and two electron pockets near the M-point, recovering the usual Fermi surface picture of Fe-based superconductors. Our calculations show unambiguously that the topology of the Fermi surface, even above a magnetic ordering temperature, should be very similar to the well-known pocket structure of other iron-based pnictides; this should be immediately verifiable in ARPES experiments.

The striking difference between the behavior of  $\text{Fe}_{\text{Li}}$ - and  $\text{Fe}_{\text{Se}}$ -derived states, related to the different valences of the two atoms, is one of the most spectacular realizations so far of qualitatively different effects of Hund's rule coupling, depending on the valence state of the atoms, in one single compound.

*Note:* Recently, we became aware of another paper which discusses an alternative antiferromagnetic order in FeSe monolayers and  $\text{LiFeO}_2\text{Fe}_2\text{Se}_2$  [197]. We note that the ordering pattern is consistent with the slight maximum along the X-M line in the full susceptibility in Fig. 7.5.

### **Acknowledgements:**

The authors would like to thank G. Giovannetti for useful discussion. Calculations have been done on the dcluster of TU Graz. L.B. acknowledges partial support through the DFG-SPP 1458 project, Grant No. Bo-3536/2. M.A. acknowledges support from the Austrian Science Fund (FWF) through the SFB VICOM, subproject F04103.

# Chapter 8.

## Conclusion

In this thesis, we have investigated the electronic properties of iron-based superconductors *ab initio*. In particular, we have calculated bare susceptibilities and studied their behavior with the application of pressure or doping in these materials. To do that, we developed a new implementation of the tetrahedron method that allowed us to calculate bare susceptibilities from full potential first-principles calculations very accurately. Our code was built on the foundations provided by MacDonald, Vosko and Coleridge [119] and uses an integration algorithm similar to the one described by Rath and Freeman [116]. Different to many other methods reported in literature, we rewrite the difference of Heaviside functions appearing in the nominator of the susceptibility formula as a product of these functions and reshape our tetrahedron mesh to occupy only the region of the first Brillouin zone that is physically relevant, thus avoiding the computation of many contributions that cancel each other. The benefit of this implementation lies in the fact that we already achieve a very high accuracy for a very small number of  $k$  points in the Brillouin zone. This in turn allows us to drop common approximations and evaluate the susceptibility from first-principles with properly included matrix elements and converge the results with respect to the number of bands. In addition, we are also able to compute dynamical bare susceptibilities without any approximations. A schematical description of the implementation and its application to chromium and FeSe as prime examples have been published in Ref. [80], which constitutes chapter 4 of this work, while a more detailed elaboration of the working principles is presented in chapter 3.

With this new algorithm at our disposal, we investigated several different members of the family of iron-based superconductors. This novel class of materials opened a new field of research for unconventional high- $T_c$  superconductivity. While they do share some features with other unconventional superconductors, such as the close proximity of antiferromagnetic order and superconductivity in the phase diagram or the emergence of a collective magnon mode, they also have unique properties [2]. One of these unique features is, for example, the low-energy bandstructure and in particular the characteristic Fermi surfaces. For many materials of the class of iron-based superconductors there is strong evidence that the appearance of the magnetic order is caused by the nesting of the Fermi surfaces and some theories explain the emergent superconductivity with a pairing induced by spin fluctuations [7].

Here, accurate susceptibility calculations can provide important insights, as the long range magnetic order should be visible as a strong response of the static susceptibility

function and spin excitations can be studied by examining the dynamical susceptibility.

In chapters 5 and 6 we presented results of bare susceptibility calculations for two prototypical examples of iron-based superconductors. In chapter 5 we considered LaFeAsO, the first iron-based superconductor [1], and investigated the effects of fluorine and hydrogen doping on the electronic structure. In accordance with other studies, we found a strong response of the static bare susceptibility at the nesting vector, indicating an instability of the system towards a single-stripe antiferromagnetic ordering. With increasing doping, this response becomes weaker due to the growing mismatch of the Fermi surfaces. We showed that the weight removed at the nesting wave vector is redistributed to other areas of the Brillouin zone. This may be connected to the experimentally observed phase diagram, where the superconducting phase grows at the cost of the antiferromagnetic phase. We also presented calculations of the dynamical bare susceptibilities, where we considered the undoped parent compound as well as various dopings. While the magnetic order of the undoped parent material could be determined correctly in our calculations, no connections of the bare susceptibility to experimentally observed spin waves and the evolution of  $T_c$  could be drawn due to the neglected interactions in our calculations.

Another interesting iron-based superconductor is FeSe, which becomes superconducting upon the application of pressure. Several experiments have been performed on this compound, which either apply pressure hydrostatically [161] or non-hydrostatically [138]. Intriguingly, the phase diagram looks very similar for both of these cases. To investigate this behavior theoretically, we have carried out static susceptibility calculations for a variety of different hydrostatic and non-hydrostatic pressures, simulated by a compression of the crystal structure. This work has been made available under Ref. [81] and is reproduced in chapter 6 of this thesis. Our calculations showed that the peak observed in the susceptibility curve of the untreated compound is again connected to a nesting of the Fermi surfaces and that hydrostatic pressure leaves the Fermi surface topology to great extent unchanged. For medium and high non-hydrostatic pressures, however, a reshaping of the Fermi surface occurs and the strong response seen in the susceptibility is lost. We have therefore concluded that superconductivity in this compound, which seems to be independent from the way the pressure is applied, cannot be explained by scrutinizing results obtained with bare susceptibility calculations.

After having presented results of bare susceptibility calculations for two prototypical examples of iron-based superconductors, we presented a more comprehensive study on a member of a new subclass of iron-based superconductors comprising magnetic atoms in the intercalated layers. So far, the only compounds of this family are  $\text{Sr}_2\text{VO}_3\text{FeAs}$  [186], rare-earth pnictides and  $\text{LiFeO}_2\text{Fe}_2\text{Se}_2$  [183]. Especially the latter is of great interest to the scientific community, as the magnetic atom is itself iron. In chapter 7 we present a study on the electronic and magnetic structure of  $\text{LiFeO}_2\text{Fe}_2\text{Se}_2$  that has been published in Ref. [95]. In order to present an extensive picture of the physical behavior of this material, we not only concentrated on bare susceptibility calculations, but also took into account interaction and correlation effects within the framework of LDA+U and DMFT. In particular, we investigated the effects of the different iron valences in the two types of layers that build up this superconductor. In the framework of density

---

functional theory, we showed that both irons -  $\text{Fe}_{\text{Se}}$  in the FeSe layer and  $\text{Fe}_{\text{Li}}$  in the  $\text{LiFeO}_2$  layer - have a strong tendency towards magnetism. We found the lowest energy for a state in which both layers are antiferromagnetically ordered and upon introducing a Hubbard-type interaction, both layers are either metallic or insulating at the same time. In addition, many metastable states with very low energy exist, thus hinting towards a paramagnetic behavior of  $\text{LiFeO}_2\text{Fe}_2\text{Se}_2$ . We simulated this situation with the dynamical mean field theory, which also takes correlations into account. In this framework, the different valences of the iron atoms have a great effect.  $\text{Fe}_{\text{Li}}$ , with a  $3d^5$  configuration, is an incipient Mott insulator, while  $\text{Fe}_{\text{Se}}$  has to be placed in the Hund's metal regime due to its  $3d^6$  configuration.  $\text{LiFeO}_2\text{Fe}_2\text{Se}_2$  therefore constitutes a highly intriguing example of a single compound where qualitatively different effects of Hund's rule coupling are observed.

With the highly efficient and accurate method, presented in this thesis, at our disposal, it would of course be interesting to consider continuative methods that are based on these non-interacting results and take into account interaction effects. One possible way has been presented in Sec. 2.4.3 along the lines of RPA. In order not to lose many advantages of our approach, it would be favorable to stay in a band basis instead of the orbital basis used in many model Hamiltonians. The interaction matrix in this picture, however, is a lot more complicated and while we described the theoretical line of approach, time has to be invested in the numerical implementation. Another highly interesting enhancement would be to stay in the framework of *ab initio* methods and to consider local field effects, as described in Sec. 2.4.2, and in this way avoid the need to introduce interaction parameters by hand. Work in this direction has already been presented by Essenberger *et al.* [52] and yields very promising results. By refining our method and going beyond bare susceptibilities, we would move the numerical results closer to the experimentally measured quantities and in turn widening the field of application of these calculations to many other materials.



# Appendix A.

## Integration Formulas

### Analytical Integration of $I = \int_V \frac{d^3k}{\epsilon_{\mathbf{k}+\mathbf{q}} - \epsilon_{\mathbf{k}}}$

We want to integrate the function  $f = (\epsilon_{\mathbf{k}+\mathbf{q}} - \epsilon_{\mathbf{k}})^{-1}$  over the volume of a small tetrahedron with corner coordinates  $\{\mathbf{k}_0, \mathbf{k}_1, \mathbf{k}_2, \mathbf{k}_3\}$ . The tetrahedron is spanned by the three basis vectors  $\mathbf{v}_i = \mathbf{k}_i - \mathbf{k}_0$ , as depicted in Fig. A, and each point inside the tetrahedron with coordinate  $\mathbf{k}$  can be expressed as

$$\mathbf{k} - \mathbf{k}_0 = \sum_{i=1}^3 p_i \mathbf{v}_i \quad \text{with} \quad 0 \leq p_i \leq 1 \quad \text{and} \quad \sum_{i=1}^3 p_i \leq 1 .$$

If we choose the tetrahedrons to be small enough, the energies can be considered to vary linearly within a tetrahedron and the energy denominator can be expanded about the vertex point  $\mathbf{k}_0$  in a similar way

$$\begin{aligned} \epsilon_{\mathbf{k}+\mathbf{q}} - \epsilon_{\mathbf{k}} &= \epsilon_{\mathbf{k}_0+\mathbf{q}} - \epsilon_{\mathbf{k}_0} + \mathbf{g} \cdot (\mathbf{k} - \mathbf{k}_0) \\ &= \epsilon_{\mathbf{k}_0} + \sum_{i=1}^3 p_i \mathbf{g} \cdot \mathbf{v}_i , \end{aligned} \quad (\text{A.1})$$

where  $\mathbf{g}$  is the vector of the energy gradient, i.e.  $g_i = \epsilon_{\mathbf{k}_i+\mathbf{q}} - \epsilon_{\mathbf{k}_i} - (\epsilon_{\mathbf{k}_0+\mathbf{q}} - \epsilon_{\mathbf{k}_0})$ . Hence the function to be integrated becomes

$$f(\mathbf{p}) = \frac{1}{\epsilon_0 + \sum_{i=1}^3 c_i p_i} \quad \text{with} \quad c_i = \mathbf{g} \cdot \mathbf{v}_i \quad \text{and} \quad \epsilon_0 = \epsilon_{\mathbf{k}_0} . \quad (\text{A.2})$$

The integral can be transformed into

$$\begin{aligned} \frac{1}{\det(\mathbf{v}_1, \mathbf{v}_2, \mathbf{v}_3)} I &= \int_0^1 dp_1 \int_0^{1-p_1} dp_2 \int_0^{1-p_1-p_2} dp_3 f(\mathbf{p}) \Theta(1 - (p_1 + p_2 + p_3)) \\ &= \int_0^1 dp_1 \int_0^{1-p_1} dp_2 \int_0^{1-p_1-p_2} dp_3 f(\mathbf{p}) , \end{aligned} \quad (\text{A.3})$$

where the first factor takes into account the transformation of the tetrahedron volume when going from  $\mathbf{k}_i$  to  $\mathbf{v}_i$ . The remaining integral  $I$  has the structure

$$\begin{aligned} I &= - \frac{\epsilon_0^2 \ln(\epsilon_0)}{2c_1 c_2 c_3} + \frac{(c_1 + \epsilon_0)^2 \ln(|c_1 + \epsilon_0|)}{2c_1(c_1 - c_2)(c_1 - c_3)} + \frac{(c_2 + \epsilon_0)^2 \ln(|c_2 + \epsilon_0|)}{2c_2(c_2 - c_1)(c_2 - c_3)} + \\ &+ \frac{(c_3 + \epsilon_0)^2 \ln(|c_3 + \epsilon_0|)}{2c_3(c_3 - c_1)(c_3 - c_2)} . \end{aligned} \quad (\text{A.4})$$

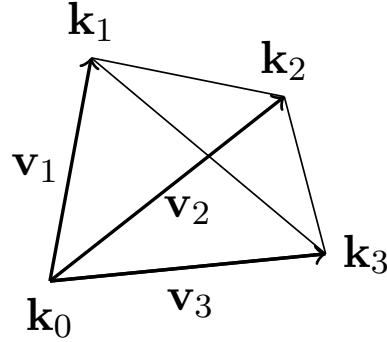


Figure A.1.: Schematic depiction of the corner coordinates  $\mathbf{k}_i$  and the vectors  $\mathbf{v}_i$  spanning the tetrahedron over which we have to integrate.

This sum of quotients has to be carefully analyzed to deal with the singularities of the quotients and the logarithms properly. For this, we consider all possible cases and perform the limits accordingly.

At first let us take a look at the expressions when  $\epsilon_0$  is equal to zero:

- $\epsilon_0 = 0$  &  $c_i \neq 0$

- **(0,abc)**: All  $c_i$  are different

$$I = \frac{c_1(c_2 - c_3) \ln(c_1) + c_2(c_3 - c_1) \ln(c_2) + c_3(c_1 - c_2) \ln(c_3)}{2(c_1 - c_2)(c_1 - c_3)(c_2 - c_3)}$$

- **(0,aab)**: 2  $c_i$  are equal but different from the third

$$I = \frac{c_1 - c_3 - c_3 \ln(c_1) + c_3 \ln(c_3)}{2(c_1 - c_3)^2}$$

- **(0,aaa)**: All  $c_i$  are equal

$$I = \frac{1}{4c_1}$$

- $\epsilon_0 = 0$  & one  $c_i = 0$ , the other  $c_i \neq 0$

- **(0,ab0)**: The two non-zero  $c_i$  are different

$$I = \frac{\ln(c_1) - \ln(c_2)}{2(c_1 - c_2)}$$

---

– **(0,aa0)**: The two non-zero  $c_i$  are equal

$$I = \frac{1}{2c_1}$$

•  $\epsilon_0 = 0$  & two  $c_i = 0$ , the other  $c_i \neq 0$ , i.e. **(0,a00)**

$$I = \frac{\infty}{c_1}$$

•  $\epsilon_0 = 0$  & all  $c_i = 0$ , i.e. **(0,000)**

This case leads to an undefined expression

It is checked in our numerical implementation that the last two expressions never appear. If  $\epsilon_0$  is non-vanishing, we get the following expressions for  $I$ :

•  $\epsilon_0 \neq 0$  &  $c_i \neq 0$

– **( $\epsilon$ ,abc)**: All  $c_i$  are different

$$I = -\frac{\epsilon_0^2 \ln(\epsilon_0)}{2c_1 c_2 c_3} + \frac{(c_1 + \epsilon_0)^2 \ln(|c_1 + \epsilon_0|)}{2c_1(c_1 - c_2)(c_1 - c_3)} + \frac{(c_2 + \epsilon_0)^2 \ln(|c_2 + \epsilon_0|)}{2c_2(c_2 - c_1)(c_2 - c_3)} + \frac{(c_3 + \epsilon_0)^2 \ln(|c_3 + \epsilon_0|)}{2c_3(c_3 - c_1)(c_3 - c_2)}$$

– **( $\epsilon$ ,aab)**: 2  $c_i$  are equal but different from the third  
if  $c_i \neq -\epsilon_0$

$$I = -\frac{1}{2c_1^2(c_1 - c_3)^2 c_3} ((c_1 - c_3)^2 \epsilon_0^2 \ln(\epsilon_0) + c_3(c_1 + \epsilon_0)(c_1(c_3 + 2\epsilon_0) - c_3\epsilon_0) \ln(c_1 + \epsilon_0) - c_1((c_3(c_1 - c_3)(c_1 + \epsilon_0) + c_1(c_3 + \epsilon_0)^2 \ln(c_3 + \epsilon_0))))$$

if  $c_i = -\epsilon_0$

$$I = -\frac{1}{2c_1^2(c_1 - c_3)^2 c_3} ((c_1 - c_3)^2 \epsilon_0^2 \ln(\epsilon_0) - c_1^2(c_3 + \epsilon_0)^2 \ln(c_3 + \epsilon_0))$$

– **( $\epsilon$ ,aaa)**: All  $c_i$  are equal

$$I = \frac{1}{4c_1^3} (c_1^2 - 2c_1\epsilon_0 - 2\epsilon_0^2 \ln(\epsilon_0) + 2\epsilon_0^2 \ln(c_1 + \epsilon_0))$$

•  $\epsilon_0 \neq 0$  & one  $c_i = 0$ , the other  $c_i \neq 0$

– ( $\epsilon, \mathbf{ab0}$ ): The two non-zero  $c_i$  are different

$$I = \frac{1}{2c_1^2 c_2^2 (c_1 - c_2)} (\epsilon_0 (c_1 - c_2) (c_2 \epsilon_0 + c_1 (2c_2 + \epsilon_0)) \ln(\epsilon_0) + c_2^2 (c_1 + \epsilon_0)^2 \ln(c_1 + \epsilon_0) - c_1 (c_2 \epsilon_0 (c_2 - c_1) + c_1 (c_2 + \epsilon_0)^2 \ln(c_2 + \epsilon_0)))$$

– ( $\epsilon, \mathbf{aa0}$ ): The two non-zero  $c_i$  are equal

$$I = \frac{1}{2c_1^3} (c_1 (c_1 + 2\epsilon_0) + 2\epsilon_0 (c_1 + \epsilon_0) \ln(\epsilon_0) - 2\epsilon_0 (c_1 + \epsilon_0) \ln(c_1 + \epsilon_0))$$

•  $\epsilon_0 \neq 0$  & two  $c_i = 0$ , the other  $c_i \neq 0$ , i.e. ( $\epsilon, \mathbf{a00}$ )

$$I = -\frac{1}{4c_1^3} (c_1 (3c_1 + 2\epsilon_0) + 2(c_1 + \epsilon_0)^2 \ln(\epsilon_0) - 2(c_1 + \epsilon_0)^2 \ln(c_1 + \epsilon_0))$$

•  $\epsilon_0 \neq 0$  & all  $c_i = 0$ , i.e. ( $\epsilon, \mathbf{000}$ )

$$I = \frac{1}{6\epsilon_0}$$

# Acknowledgements

First of all, I want to thank Prof. Wolfgang von der Linden for supervising me and for giving me the opportunity to work on many different interesting topics. He provided me with a perfect working environment and I'm deeply indebted for all the time he spent discussing and explaining all kinds of topics. While he was never short of new ideas for future projects, he allowed me the freedom of pursuing my own interests in research. He always had an open ear for all my problems related to research, teaching or of some other kind, and tried to resolve them to everyone's best interest. I really do count myself lucky for having had such an experienced, knowledgeable and kind supervisor.

Lilia Boeri joined our research group quite late, yet the amount of ideas and insights she gave me on various topics in physics can hardly be measured. I'm very grateful to her for taking me under her wing and I really enjoyed working with her on our projects. I'm sure to remember her warm and friendly nature and hope that we can keep working on some future projects together.

I'm also in great debt of gratitude towards Prof. Heinrich Sormann. He allowed me to use his susceptibility program as a basis for our new implementation and patiently guided me to a point at which I could implement my own ideas into our algorithms and successfully employ the method to projects of current interest to the scientific community. Even his retirement didn't stop him from supporting me in all my research projects, for which I'm very grateful.

Along similar lines I want to thank Markus Aichhorn, who has also been a great source of knowledge to me. He generously provided me with the TRIQS code and was extremely patient in explaining all the details I needed to know to get the calculations running. During all our coffee and lunch breaks he has also proven to be proficient in basically all important (and also not so important) aspects of life.

Staying within the Institute of Theoretical and Computational Physics, I want to thank my office colleagues Martin Nuss und Antonius Dorda for all the interesting discussions we had on physics and for enduring patiently my nagging, whenever I've encountered yet another problem with my programs. In this context, Andreas Hirczy has to be mentioned as well, who was always helpful with any problems I had with my workstation or the network of our institute. A big "thank you" also has to go to Brigitte Schwarz for helping me with all administrative and organizational problems.

I want to take the opportunity here and thank all the other people at the ITP<sup>CP</sup> not explicitly mentioned for the very warm welcome when I started my work, and the great atmosphere during the time of my Ph.D. project. I couldn't have wished for a nicer and more enjoyable community.

Gratitude is also owed to Prof. Enrico Arrigoni and Prof. Ewald Schachinger, here at the TU Graz, and Prof. Ilya Eremin, currently at the Ruhr-Universität Bochum, for

very fruitful discussions on various topics concerning iron-based superconductors and possible new ways to calculate susceptibilities within the random phase approximation. I also want to thank Prof. Gianaurelio Cuniberti and Rafael Gutiérrez at the institute of Materials Science and Nanotechnology at the Dresden University of Technology for letting me visit their group and sharing thoughts and insights on non-equilibrium Green's function techniques.

## Bibliography

- [1] Y. Kamihara *et al.*, *Iron-Based Layered Superconductor LaOFeAs*, Journal of the American Chemical Society **130**, 3296 (2008). doi:10.1021/ja800073m
- [2] J. Paglione and R. L. Greene, *High-temperature superconductivity in iron-based materials*, Nat Phys **6**, 645 (2010). doi:10.1038/nphys1759
- [3] Y. Kamihara *et al.*, *Iron-Based Layered Superconductor: LaOFeP*, J. Am. Chem. Soc. **128**, 10012 (2006). doi:10.1021/ja063355c
- [4] C. d. l. Cruz *et al.*, *Magnetic order close to superconductivity in the iron-based layered LaO<sub>1-x</sub>F<sub>x</sub>FeAs systems*, Nature **453**, 899 (2008). doi:10.1038/nature07057
- [5] M. H. Fang *et al.*, *Superconductivity close to magnetic instability in Fe(Se<sub>1-x</sub>Te<sub>x</sub>)<sub>0.82</sub>*, Physical Review B **78**, 224503 (2008). doi:10.1103/PhysRevB.78.224503
- [6] Q. Huang *et al.*, *Neutron-Diffraction Measurements of Magnetic Order and a Structural Transition in the Parent BaFe<sub>2</sub>As<sub>2</sub> Compound of FeAs-Based High-Temperature Superconductors*, Physical Review Letters **101**, 257003 (2008). doi:10.1103/PhysRevLett.101.257003
- [7] D. C. Johnston, *The puzzle of high temperature superconductivity in layered iron pnictides and chalcogenides*, Advances in Physics **59**, 803 (2010). doi:10.1080/00018732.2010.513480
- [8] E. C. Blomberg *et al.*, *Sign-reversal of the in-plane resistivity anisotropy in hole-doped iron pnictides*, Nat Commun **4**, 1914 (2013). doi:10.1038/ncomms2933
- [9] J. N. Millican *et al.*, *Pressure-induced effects on the structure of the FeSe superconductor*, Solid State Communications **149**, 707 (2009). doi:10.1016/j.ssc.2009.02.011
- [10] N. C. Gresty *et al.*, *Structural Phase Transitions and Superconductivity in Fe<sub>1+δ</sub>Se<sub>0.57</sub>Te<sub>0.43</sub> at Ambient and Elevated Pressures*, Journal of the American Chemical Society **131**, 16944 (2009). doi:10.1021/ja907345x
- [11] N. Ni *et al.*, *Temperature versus doping phase diagrams for BaFe<sub>2</sub>As<sub>2</sub> single crystals*, Physical Review B **82**, 024519 (2010). doi:10.1103/PhysRevB.82.024519
- [12] N. Colonna *et al.*, *Structural and magnetic properties of CaFe<sub>2</sub>As<sub>2</sub> and BaFe<sub>2</sub>As<sub>2</sub> from first-principles density functional theory*, Phys. Rev. B **83**, 094529 (2011). doi:10.1103/PhysRevB.83.094529

- [13] A. Sanna *et al.*, *First-principles study of rare-earth-doped superconducting  $\text{CaFe}_2\text{As}_2$* , Phys. Rev. B **86**, 014507 (2012). doi:10.1103/PhysRevB.86.014507
- [14] M. Tomić *et al.*, *Uniaxial versus hydrostatic pressure-induced phase transitions in  $\text{CaFe}_2\text{As}_2$  and  $\text{BaFe}_2\text{As}_2$* , Physical Review B **85**, 094105 (2012). doi:10.1103/PhysRevB.85.094105
- [15] M. Monni *et al.*, *Theoretical investigation of FeTe magnetic ordering under hydrostatic pressure*, Phys. Rev. B **87**, 094516 (2013). doi:10.1103/PhysRevB.87.094516
- [16] A. Subedi *et al.*, *Density functional study of FeS, FeSe, and FeTe: Electronic structure, magnetism, phonons, and superconductivity*, Physical Review B **78**, 134514 (2008). doi:10.1103/PhysRevB.78.134514
- [17] D. J. Singh and M.-H. Du, *Density Functional Study of  $\text{LaFeAsO}_{1-x}\text{F}_x$ : A Low Carrier Density Superconductor Near Itinerant Magnetism*, Phys. Rev. Lett. **100**, 237003 (2008). doi:10.1103/PhysRevLett.100.237003
- [18] A. V. Chubukov *et al.*, *Magnetism, superconductivity, and pairing symmetry in iron-based superconductors*, Phys. Rev. B **78**, 134512 (2008). doi:10.1103/PhysRevB.78.134512
- [19] J. Knolle *et al.*, *Theory of itinerant magnetic excitations in the spin-density-wave phase of iron-based superconductors*, Phys. Rev. B **81**, 140506 (2010). doi:10.1103/PhysRevB.81.140506
- [20] I. I. Mazin *et al.*, *Problems with reconciling density functional theory calculations with experiment in ferropnictides*, Physical Review B **78**, 085104 (2008). doi:10.1103/PhysRevB.78.085104
- [21] I. I. Mazin, *Superconductivity gets an iron boost*, Nature **464**, 183 (2010). doi:10.1038/nature08914
- [22] D. J. Singh, *Magnetism and Superconductivity in Iron Pnictides*, Acta Physica Polonica A **121**, 999 (2012).
- [23] C. Cao *et al.*, *Proximity of antiferromagnetism and superconductivity in  $\text{LaFeAsO}_{1-x}\text{F}_x$ : Effective Hamiltonian from *ab initio* studies*, Phys. Rev. B **77**, 220506 (2008). doi:10.1103/PhysRevB.77.220506
- [24] D. J. Singh, *Electronic structure of Fe-based superconductors*, Physica C: Superconductivity **469**, 418 (2009). doi:10.1016/j.physc.2009.03.035
- [25] M. D. Lumsden and A. D. Christianson, *Magnetism in Fe-based superconductors*, J. Phys.: Condens. Matter **22**, 203203 (2010). doi:10.1088/0953-8984/22/20/203203
- [26] M. Aichhorn *et al.*, *Dynamical mean-field theory within an augmented plane-wave framework: Assessing electronic correlations in the iron pnictide  $\text{LaFeAsO}$* , Phys. Rev. B **80**, 085101 (2009). doi:10.1103/PhysRevB.80.085101

- [27] Z. P. Yin *et al.*, *Magnetism and charge dynamics in iron pnictides*, Nat Phys **7**, 294 (2011). doi:10.1038/nphys1923
- [28] Z. P. Yin *et al.*, *Kinetic frustration and the nature of the magnetic and paramagnetic states in iron pnictides and iron chalcogenides*, Nature Materials **10**, 932 (2011). doi:10.1038/nmat3120
- [29] L. Boeri *et al.*, *Is LaFeAsO<sub>1-x</sub>F<sub>x</sub> an Electron-Phonon Superconductor?*, Phys. Rev. Lett. **101**, 026403 (2008). doi:10.1103/PhysRevLett.101.026403
- [30] L. Boeri *et al.*, *Effects of magnetism and doping on the electron-phonon coupling in BaFe<sub>2</sub>As<sub>2</sub>*, Phys. Rev. B **82**, 020506 (2010). doi:10.1103/PhysRevB.82.020506
- [31] R. H. Liu *et al.*, *A large iron isotope effect in SmFeAsO<sub>1-x</sub>F<sub>x</sub> and Ba<sub>1-x</sub>K<sub>x</sub>Fe<sub>2</sub>As<sub>2</sub>*, Nature **459**, 64 (2009). doi:10.1038/nature07981
- [32] P. J. Hirschfeld *et al.*, *Gap symmetry and structure of Fe-based superconductors*, Reports on Progress in Physics **74**, 124508 (2011). doi:10.1088/0034-4885/74/12/124508
- [33] I. I. Mazin *et al.*, *Unconventional Superconductivity with a Sign Reversal in the Order Parameter of LaFeAsO<sub>1-x</sub>F<sub>x</sub>*, Physical Review Letters **101**, 057003 (2008). doi:10.1103/PhysRevLett.101.057003
- [34] N. F. Berk and J. R. Schrieffer, *Effect of Ferromagnetic Spin Correlations on Superconductivity*, Phys. Rev. Lett. **17**, 433 (1966). doi:10.1103/PhysRevLett.17.433
- [35] D. J. Scalapino, *The case for d<sub>x<sup>2</sup>-y<sup>2</sup></sub> pairing in the cuprate superconductors*, Physics Reports **250**, 329 (1995). doi:10.1016/0370-1573(94)00086-I
- [36] T. Dahm *et al.*, *Strength of the spin-fluctuation-mediated pairing interaction in a high-temperature superconductor*, Nat Phys **5**, 217 (2009). doi:10.1038/nphys1180
- [37] D. J. Scalapino, *A common thread: The pairing interaction for unconventional superconductors*, Rev. Mod. Phys. **84**, 1383 (2012). doi:10.1103/RevModPhys.84.1383
- [38] J. W. Lynn and P. Dai, *Neutron studies of the iron-based family of high T<sub>c</sub> magnetic superconductors*, Physica C: Superconductivity **469**, 469 (2009). doi:10.1016/j.physc.2009.03.046
- [39] J. Zhao *et al.*, *Spin waves and magnetic exchange interactions in CaFe<sub>2</sub>As<sub>2</sub>*, Nat Phys **5**, 555 (2009). doi:10.1038/nphys1336
- [40] S. O. Diallo *et al.*, *Itinerant Magnetic Excitations in Antiferromagnetic CaFe<sub>2</sub>As<sub>2</sub>*, Phys. Rev. Lett. **102**, 187206 (2009). doi:10.1103/PhysRevLett.102.187206
- [41] J. T. Park *et al.*, *Symmetry of spin excitation spectra in the tetragonal paramagnetic and superconducting phases of 122-ferropnictides*, Phys. Rev. B **82**, 134503 (2010). doi:10.1103/PhysRevB.82.134503

- [42] R. A. Ewings *et al.*, *Itinerant spin excitations in SrFe<sub>2</sub>As<sub>2</sub> measured by inelastic neutron scattering*, Phys. Rev. B **83**, 214519 (2011). doi:10.1103/PhysRevB.83.214519
- [43] J. Dong *et al.*, *Competing orders and spin-density-wave instability in La(O<sub>1-x</sub>F<sub>x</sub>)FeAs*, EPL **83**, 27006 (2008). doi:10.1209/0295-5075/83/27006
- [44] M. J. Winiarski *et al.*, *Strain effects on the electronic structure of the iron selenide superconductor*, EPL **100**, 47005 (2012). doi:10.1209/0295-5075/100/47005
- [45] K. Kuroki *et al.*, *Unconventional Pairing Originating from the Disconnected Fermi Surfaces of Superconducting LaFeAsO<sub>1-x</sub>F<sub>x</sub>*, Physical Review Letters **101**, 087004 (2008). doi:10.1103/PhysRevLett.101.087004
- [46] S. Graser *et al.*, *Near-degeneracy of several pairing channels in multiorbital models for the Fe pnictides*, New J. Phys. **11**, 025016 (2009). doi:10.1088/1367-2630/11/2/025016
- [47] L. Ke *et al.*, *Low-energy coherent Stoner-like excitations in CaFe<sub>2</sub>As<sub>2</sub>*, Phys. Rev. B **83**, 060404 (2011). doi:10.1103/PhysRevB.83.060404
- [48] A. Kreisel *et al.*, *Spin fluctuations and superconductivity in K<sub>x</sub>Fe<sub>2-y</sub>Se<sub>2</sub>*, Phys. Rev. B **88**, 094522 (2013). doi:10.1103/PhysRevB.88.094522
- [49] F. Wang *et al.*, *Functional Renormalization-Group Study of the Pairing Symmetry and Pairing Mechanism of the FeAs-Based High-Temperature Superconductor*, Phys. Rev. Lett. **102**, 047005 (2009). doi:10.1103/PhysRevLett.102.047005
- [50] Z.-J. Yao *et al.*, *Spin fluctuations, interband coupling and unconventional pairing in iron-based superconductors*, New J. Phys. **11**, 025009 (2009). doi:10.1088/1367-2630/11/2/025009
- [51] J. Zhang *et al.*, *Orbital coupling and superconductivity in the iron pnictides*, Phys. Rev. B **79**, 220502 (2009). doi:10.1103/PhysRevB.79.220502
- [52] F. Essenberg *et al.*, *Paramagnons in FeSe close to a magnetic quantum phase transition: Ab initio study*, Phys. Rev. B **86**, 060412 (2012). doi:10.1103/PhysRevB.86.060412
- [53] F. Essenberg *et al.*, *Superconducting pairing mediated by spin fluctuations from first principles*, Phys. Rev. B **90**, 214504 (2014). doi:10.1103/PhysRevB.90.214504
- [54] L. Zhao *et al.*, *Common Fermi-surface topology and nodeless superconducting gap of K<sub>0.68</sub>Fe<sub>1.79</sub>Se<sub>2</sub> and (Tl<sub>0.45</sub>K<sub>0.34</sub>)Fe<sub>1.84</sub>Se<sub>2</sub> superconductors revealed via angle-resolved photoemission*, Phys. Rev. B **83**, 140508 (2011). doi:10.1103/PhysRevB.83.140508
- [55] Y. Zhou *et al.*, *Theory for superconductivity in (Tl,K)Fe<sub>x</sub>Se<sub>2</sub> as a doped Mott insulator*, EPL **95**, (2011). doi:10.1209/0295-5075/95/17003

- [56] F. Wang *et al.*, *The electron pairing of  $K_xFe_{2-x}Se_2$* , EPL **93**, (2011). [doi:10.1209/0295-5075/93/57003](https://doi.org/10.1209/0295-5075/93/57003)
- [57] T. Qian *et al.*, *Absence of a Holelike Fermi Surface for the Iron-Based  $K_{0.8}Fe_{1.7}Se_2$  Superconductor Revealed by Angle-Resolved Photoemission Spectroscopy*, Phys. Rev. Lett. **106**, 187001 (2011). [doi:10.1103/PhysRevLett.106.187001](https://doi.org/10.1103/PhysRevLett.106.187001)
- [58] K. Kuroki *et al.*, *Pnictogen height as a possible switch between high- $T_c$  nodeless and low- $T_c$  nodal pairings in the iron-based superconductors*, Phys. Rev. B **79**, 224511 (2009). [doi:10.1103/PhysRevB.79.224511](https://doi.org/10.1103/PhysRevB.79.224511)
- [59] H. Kontani and S. Onari, *Orbital-Fluctuation-Mediated Superconductivity in Iron Pnictides: Analysis of the Five-Orbital Hubbard-Holstein Model*, Phys. Rev. Lett. **104**, 157001 (2010). [doi:10.1103/PhysRevLett.104.157001](https://doi.org/10.1103/PhysRevLett.104.157001)
- [60] Y. Yanagi *et al.*, *Orbital Order, Structural Transition, and Superconductivity in Iron Pnictides*, J. Phys. Soc. Jpn. **79**, 123707 (2010). [doi:10.1143/JPSJ.79.123707](https://doi.org/10.1143/JPSJ.79.123707)
- [61] H. Kontani *et al.*, *Origin of orthorhombic transition, magnetic transition, and shear-modulus softening in iron pnictide superconductors: Analysis based on the orbital fluctuations theory*, Phys. Rev. B **84**, 024528 (2011). [doi:10.1103/PhysRevB.84.024528](https://doi.org/10.1103/PhysRevB.84.024528)
- [62] A. Chubukov, *Pairing Mechanism in Fe-Based Superconductors*, Annual Review of Condensed Matter Physics **3**, 57 (2012). [doi:10.1146/annurev-conmatphys-020911-125055](https://doi.org/10.1146/annurev-conmatphys-020911-125055)
- [63] A. A. Kordyuk, *Iron-based superconductors: Magnetism, superconductivity, and electronic structure (Review Article)*, Low Temperature Physics **38**, 888 (2012). [doi:10.1063/1.4752092](https://doi.org/10.1063/1.4752092)
- [64] A. D. Christianson *et al.*, *Unconventional superconductivity in  $Ba_{0.6}K_{0.4}Fe_2As_2$  from inelastic neutron scattering*, Nature **456**, 930 (2008). [doi:10.1038/nature07625](https://doi.org/10.1038/nature07625)
- [65] S. Chi *et al.*, *Inelastic Neutron-Scattering Measurements of a Three-Dimensional Spin Resonance in the FeAs-Based  $BaFe_{1.9}Ni_{0.1}As_2$  Superconductor*, Phys. Rev. Lett. **102**, 107006 (2009). [doi:10.1103/PhysRevLett.102.107006](https://doi.org/10.1103/PhysRevLett.102.107006)
- [66] M. D. Lumsden *et al.*, *Two-dimensional resonant magnetic excitation in  $BaFe_{1.84}Co_{0.16}As_2$* , Phys. Rev. Lett. **102**, 107005 (2009). [doi:10.1103/PhysRevLett.102.107005](https://doi.org/10.1103/PhysRevLett.102.107005)
- [67] Y. Qiu *et al.*, *Spin Gap and Resonance at the Nesting Wave Vector in Superconducting  $FeSe_{0.4}Te_{0.6}$* , Phys. Rev. Lett. **103**, 067008 (2009). [doi:10.1103/PhysRevLett.103.067008](https://doi.org/10.1103/PhysRevLett.103.067008)

- [68] S.-i. Shamoto *et al.*, *Inelastic neutron scattering study of the resonance mode in the optimally doped pnictide superconductor  $\text{LaFeAsO}_{0.92}\text{F}_{0.08}$* , Phys. Rev. B **82**, 172508 (2010). doi:10.1103/PhysRevB.82.172508
- [69] M. Wang *et al.*, *Electron-doping evolution of the low-energy spin excitations in the iron arsenide superconductor  $\text{BaFe}_{2-x}\text{Ni}_x\text{As}_2$* , Phys. Rev. B **81**, 174524 (2010). doi:10.1103/PhysRevB.81.174524
- [70] J. Wen *et al.*, *Effect of magnetic field on the spin resonance in  $\text{FeTe}_{0.5}\text{Se}_{0.5}$  as seen via inelastic neutron scattering*, Phys. Rev. B **81**, 100513 (2010). doi:10.1103/PhysRevB.81.100513
- [71] G. Yu *et al.*, *A universal relationship between magnetic resonance and superconducting gap in unconventional superconductors*, Nat Phys **5**, 873 (2009). doi:10.1038/nphys1426
- [72] T. A. Maier *et al.*, *Neutron scattering resonance and the iron-pnictide superconducting gap*, Phys. Rev. B **79**, 134520 (2009). doi:10.1103/PhysRevB.79.134520
- [73] D. S. Inosov *et al.*, *Normal-state spin dynamics and temperature-dependent spin-resonance energy in optimally doped  $\text{BaFe}_{1.85}\text{Co}_{0.15}\text{As}_2$* , Nat Phys **6**, 178 (2010). doi:10.1038/nphys1483
- [74] J.-P. Castellan *et al.*, *Effect of Fermi Surface Nesting on Resonant Spin Excitations in  $\text{Ba}_{1-x}\text{K}_x\text{Fe}_2\text{As}_2$* , Phys. Rev. Lett. **107**, 177003 (2011). doi:10.1103/PhysRevLett.107.177003
- [75] T. Yildirim, *Frustrated magnetic interactions, giant magnetoelastic coupling, and magnetic phonons in ironpnictides*, Physica C: Superconductivity **469**, 425 (2009). doi:10.1016/j.physc.2009.03.038
- [76] E. Kaneshita and T. Tohyama, *Spin and charge dynamics ruled by antiferromagnetic order in iron pnictide superconductors*, Phys. Rev. B **82**, 094441 (2010). doi:10.1103/PhysRevB.82.094441
- [77] J. Knolle *et al.*, *Multiorbital spin susceptibility in a magnetically ordered state: Orbital versus excitonic spin density wave scenario*, Phys. Rev. B **83**, 224503 (2011). doi:10.1103/PhysRevB.83.224503
- [78] W. Rowe *et al.*, *Spin excitations in layered antiferromagnetic metals and superconductors*, Phys. Rev. B **86**, 134513 (2012). doi:10.1103/PhysRevB.86.134513
- [79] M. Monni *et al.*, *Static and dynamical susceptibility of  $\text{LaO}_{1-x}\text{F}_x\text{FeAs}$* , Physical Review B **81**, 104503 (2010). doi:10.1103/PhysRevB.81.104503
- [80] C. Heil *et al.*, *Accurate bare susceptibilities from full-potential *ab initio* calculations*, Phys. Rev. B **90**, 115143 (2014). doi:10.1103/PhysRevB.90.115143

- [81] C. Heil *et al.*, *Indirect evidence for strong coupling superconductivity in FeSe under pressure from first-principle calculations*, arXiv:1210.2593 [cond-mat] (2012).
- [82] A. H. MacDonald *et al.*, *Extensions of the tetrahedron method for evaluating spectral properties of solids*, J. Phys. C: Solid State Phys. **12**, 2991 (1979). doi:10.1088/0022-3719/12/15/008
- [83] J. Rath and A. J. Freeman, *Generalized magnetic susceptibilities in metals: Application of the analytic tetrahedron linear energy method to Sc*, Phys. Rev. B **11**, 2109 (1975). doi:10.1103/PhysRevB.11.2109
- [84] P. Dai *et al.*, *Magnetism and its microscopic origin in iron-based high-temperature superconductors*, Nat Phys **8**, 709 (2012). doi:10.1038/nphys2438
- [85] L. de Medici *et al.*, *Janus-Faced Influence of Hund's Rule Coupling in Strongly Correlated Materials*, Phys. Rev. Lett. **107**, 256401 (2011). doi:10.1103/PhysRevLett.107.256401
- [86] A. Georges *et al.*, *Strong Correlations from Hund's Coupling*, Annual Review of Condensed Matter Physics **4**, 137 (2013). doi:10.1146/annurev-conmatphys-020911-125045
- [87] M. Aichhorn *et al.*, *Theoretical evidence for strong correlations and incoherent metallic state in FeSe*, Physical Review B **82**, 064504 (2010). doi:10.1103/PhysRevB.82.064504
- [88] L. de Medici *et al.*, *Orbital-Selective Mott Transition out of Band Degeneracy Lifting*, Phys. Rev. Lett. **102**, 126401 (2009). doi:10.1103/PhysRevLett.102.126401
- [89] L. de Medici *et al.*, *Selective Mott Physics as a Key to Iron Superconductors*, Phys. Rev. Lett. **112**, 177001 (2014). doi:10.1103/PhysRevLett.112.177001
- [90] Z. P. Yin *et al.*, *Spin dynamics and orbital-antiphase pairing symmetry in iron-based superconductors*, Nat Phys **10**, 845 (2014). doi:10.1038/nphys3116
- [91] E. K. U. Gross and E. Runge, *Vielteilchentheorie* (Teubner, 1986). ISBN:9783519030867
- [92] A. L. Fetter *et al.*, *Quantum Theory of Many-Particle Systems* (Dover Publications, 2003). ISBN:9780486428277
- [93] W. Nolting, *Grundkurs Theoretische Physik 7* (Springer, 2005). ISBN:9783540241171
- [94] K. Haule and G. Kotliar, *Coherenceincoherence crossover in the normal state of iron oxypnictides and importance of Hund's rule coupling*, New J. Phys. **11**, 025021 (2009). doi:10.1088/1367-2630/11/2/025021

- [95] C. Heil *et al.*, *Effect of the iron valence in the two types of layers in  $\text{LiFeO}_2\text{Fe}_2\text{Se}_2$* , Phys. Rev. B **90**, 165122 (2014). doi:[10.1103/PhysRevB.90.165122](https://doi.org/10.1103/PhysRevB.90.165122)
- [96] R. E. Walstedt, *The NMR Probe of High-Tc Materials* (Springer Science & Business Media, 2008). ISBN:[9783540755647](https://www.isbn-international.org/product/9783540755647)
- [97] J. F. Cooke, *Neutron Scattering from Itinerant-Electron Ferromagnets*, Phys. Rev. B **7**, 1108 (1973). doi:[10.1103/PhysRevB.7.1108](https://doi.org/10.1103/PhysRevB.7.1108)
- [98] A. G. Eguiluz *et al.*, *On the ab initio evaluation of dynamical electronic response in metals and its comparison with experiment*, Nuclear Instruments and Methods in Physics Research Section B: Beam Interactions with Materials and Atoms **96**, 550 (1995). doi:[10.1016/0168-583X\(95\)00313-4](https://doi.org/10.1016/0168-583X(95)00313-4)
- [99] D. Chandler, *Introduction to Modern Statistical Mechanics*, 1 edition ed. (Oxford University Press, 1987). ISBN:[9780195042771](https://www.isbn-international.org/product/9780195042771)
- [100] R. D. Mattuck, *A Guide to Feynman Diagrams in the Many-body Problem* (Courier Dover Publications, 1976). ISBN:[9780486670478](https://www.isbn-international.org/product/9780486670478)
- [101] E. N. Economou, *Green's Functions in Quantum Physics*, softcover reprint of hardcover 3rd ed. 2006 edition ed. (Springer, 2010). ISBN:[9783642066917](https://www.isbn-international.org/product/9783642066917)
- [102] J. D. Walecka, *Advanced Modern Physics: Theoretical Foundations* (World Scientific, 2010). ISBN:[9789814291514](https://www.isbn-international.org/product/9789814291514)
- [103] H. Sormann, *Elektronentheorie des Festkörpers*, Vorlesungsunterlagen, 2010.
- [104] T. Moriya, *Spin Fluctuations in Itinerant Electron Magnetism* (Springer-Verlag, 1985). ISBN:[9780387154220](https://www.isbn-international.org/product/9780387154220)
- [105] T. Giamarchi *et al.*, *Introduction to Many Body Physics*, Lecture Notes, 2008.
- [106] J. Hubbard, *The Description of Collective Motions in Terms of Many-Body Perturbation Theory*, Proc. R. Soc. Lond. A **240**, 539 (1957). doi:[10.1098/rspa.1957.0106](https://doi.org/10.1098/rspa.1957.0106)
- [107] J. Hubbard, *The Description of Collective Motions in Terms of Many-Body Perturbation Theory. II. The Correlation Energy of a Free-Electron Gas*, Proc. R. Soc. Lond. A **243**, 336 (1958). doi:[10.1098/rspa.1958.0003](https://doi.org/10.1098/rspa.1958.0003)
- [108] J. J. Deisz *et al.*, *Quasiparticle theory versus density-functional theory at a metal surface*, Phys. Rev. Lett. **71**, 2793 (1993). doi:[10.1103/PhysRevLett.71.2793](https://doi.org/10.1103/PhysRevLett.71.2793)
- [109] A. G. Eguiluz *et al.*, *Dynamical response of correlated electrons in solids probed by inelastic scattering experiments: an ab initio theoretical perspective*, Journal of Physics and Chemistry of Solids **61**, 383 (2000). doi:[10.1016/S0022-3697\(99\)00322-4](https://doi.org/10.1016/S0022-3697(99)00322-4)

- [110] S. Graser *et al.*, *Spin fluctuations and superconductivity in a three-dimensional tight-binding model for BaFe<sub>2</sub>As<sub>2</sub>*, Phys. Rev. B **81**, 214503 (2010). [doi:10.1103/PhysRevB.81.214503](https://doi.org/10.1103/PhysRevB.81.214503)
- [111] A. Baldereschi, *Mean-Value Point in the Brillouin Zone*, Phys. Rev. B **7**, 5212 (1973). [doi:10.1103/PhysRevB.7.5212](https://doi.org/10.1103/PhysRevB.7.5212)
- [112] D. J. Chadi and M. L. Cohen, *Electronic Structure of Hg<sub>1-x</sub>Cd<sub>x</sub>Te Alloys and Charge-Density Calculations Using Representative k Points*, Phys. Rev. B **7**, 692 (1973). [doi:10.1103/PhysRevB.7.692](https://doi.org/10.1103/PhysRevB.7.692)
- [113] O. Jepsen and O. K. Anderson, *The electronic structure of h.c.p. Ytterbium*, Solid State Communications **9**, 1763 (1971). [doi:10.1016/0038-1098\(71\)90313-9](https://doi.org/10.1016/0038-1098(71)90313-9)
- [114] G. Lehmann and M. Taut, *On the Numerical Calculation of the Density of States and Related Properties*, phys. stat. sol. (b) **54**, 469 (1972). [doi:10.1002/pssb.2220540211](https://doi.org/10.1002/pssb.2220540211)
- [115] H. J. Monkhorst and J. D. Pack, *Special points for Brillouin-zone integrations*, Phys. Rev. B **13**, 5188 (1976). [doi:10.1103/PhysRevB.13.5188](https://doi.org/10.1103/PhysRevB.13.5188)
- [116] J. Rath and A. J. Freeman, *Generalized magnetic susceptibilities in metals: Application of the analytic tetrahedron linear energy method to Sc*, Phys. Rev. B **11**, 2109 (1975). [doi:10.1103/PhysRevB.11.2109](https://doi.org/10.1103/PhysRevB.11.2109)
- [117] J. P. A. Charlesworth and W. Yeung, *An algebraic representation of the linear-analytic tetrahedron method*, Computer Physics Communications **88**, 186 (1995). [doi:10.1016/0010-4655\(95\)00022-8](https://doi.org/10.1016/0010-4655(95)00022-8)
- [118] P. E. Blchl *et al.*, *Improved tetrahedron method for Brillouin-zone integrations*, Phys. Rev. B **49**, 16223 (1994). [doi:10.1103/PhysRevB.49.16223](https://doi.org/10.1103/PhysRevB.49.16223)
- [119] A. H. MacDonald *et al.*, *Extensions of the tetrahedron method for evaluating spectral properties of solids*, J. Phys. C: Solid State Phys. **12**, 2991 (1979). [doi:10.1088/0022-3719/12/15/008](https://doi.org/10.1088/0022-3719/12/15/008)
- [120] A. N. Yaresko *et al.*, *Interplay between magnetic properties and Fermi surface nesting in iron pnictides*, Physical Review B **79**, 144421 (2009). [doi:10.1103/PhysRevB.79.144421](https://doi.org/10.1103/PhysRevB.79.144421)
- [121] P. Blaha *et al.*, *WIEN2K, An Augmented Plane Wave + Local Orbitals Program for Calculating Crystal Properties* (Karlheinz Schwarz, Techn. Universitt Wien, Austria, 2001).
- [122] O. K. Andersen, *Linear methods in band theory*, Phys. Rev. B **12**, 3060 (1975). [doi:10.1103/PhysRevB.12.3060](https://doi.org/10.1103/PhysRevB.12.3060)
- [123] G. Gilat and N. R. Bharatiya, *Tetrahedron method of zone integration: Inclusion of matrix elements*, Phys. Rev. B **12**, 3479 (1975). [doi:10.1103/PhysRevB.12.3479](https://doi.org/10.1103/PhysRevB.12.3479)

- [124] E. Fawcett, *Spin-density-wave antiferromagnetism in chromium*, Rev. Mod. Phys. **60**, 209 (1988). doi:10.1103/RevModPhys.60.209
- [125] C. G. Shull and M. K. Wilkinson, *Neutron Diffraction Studies of Various Transition Elements*, Rev. Mod. Phys. **25**, 100 (1953). doi:10.1103/RevModPhys.25.100
- [126] C. G. Windsor, *Interband contributions to the generalized spin susceptibility of chromium*, Journal of Physics F: Metal Physics **2**, 742 (1972). doi:10.1088/0305-4608/2/4/018
- [127] K. Schwartzman *et al.*, *Concentration dependence of the wave vector of the spin-density wave of chromium alloys*, Phys. Rev. B **40**, 454 (1989). doi:10.1103/PhysRevB.40.454
- [128] J. Callaway and C. S. Wang, *Transverse magnetic susceptibility in the local exchange approximation*, J. Phys. F: Met. Phys. **5**, 2119 (1975). doi:10.1088/0305-4608/5/11/024
- [129] J. P. A. Charlesworth and W. Yeung, *Susceptibilities using first principles band structures II*, Physica B: Condensed Matter **210**, 131 (1995). doi:10.1016/0921-4526(94)01106-B
- [130] I. I. Mazin and J. Schmalian, *Pairing symmetry and pairing state in ferropnictides: Theoretical overview*, Physica C: Superconductivity **469**, 614 (2009). doi:10.1016/j.physc.2009.03.019
- [131] H. Ikeda *et al.*, *Phase diagram and gap anisotropy in iron-pnictide superconductors*, Phys. Rev. B **81**, 054502 (2010). doi:10.1103/PhysRevB.81.054502
- [132] R. Thomale *et al.*, *Mechanism for Explaining Differences in the Order Parameters of FeAs-Based and FeP-Based Pnictide Superconductors*, Phys. Rev. Lett. **106**, 187003 (2011). doi:10.1103/PhysRevLett.106.187003
- [133] G. D. Samolyuk and V. P. Antropov, *Character of magnetic instabilities in  $\text{CaFe}_2\text{As}_2$* , Physical Review B **79**, 052505 (2009). doi:10.1103/PhysRevB.79.052505
- [134] S. V. Borisenko *et al.*, *Two Energy Gaps and Fermi-Surface 'Arcs' in  $\text{NbSe}_2$* , Phys. Rev. Lett. **102**, 166402 (2009). doi:10.1103/PhysRevLett.102.166402
- [135] A. F. Kemper *et al.*, *Sensitivity of the superconducting state and magnetic susceptibility to key aspects of electronic structure in ferropnictides*, New Journal of Physics **12**, 073030 (2010). doi:10.1088/1367-2630/12/7/073030
- [136] R. P. Gupta and S. K. Sinha, *Wave-Number-Dependent Susceptibility Function for Paramagnetic Chromium*, Phys. Rev. B **3**, 2401 (1971). doi:10.1103/PhysRevB.3.2401

- [137] R. P. Gupta and A. J. Freeman, *Role of matrix elements in the theoretical determination of generalized susceptibilities in metals*, Phys. Rev. B **13**, 4376 (1976). [doi:10.1103/PhysRevB.13.4376](https://doi.org/10.1103/PhysRevB.13.4376)
- [138] R. S. Kumar *et al.*, *Crystal and Electronic Structure of FeSe at High Pressure and Low Temperature*, The Journal of Physical Chemistry B **114**, 12597 (2010). [doi:10.1021/jp1060446](https://doi.org/10.1021/jp1060446)
- [139] O. Andersen and L. Boeri, *On the multi-orbital band structure and itinerant magnetism of iron-based superconductors*, Annalen der Physik **523**, 8 (2011). [doi:10.1002/andp.201000149](https://doi.org/10.1002/andp.201000149)
- [140] Y.-Z. Zhang *et al.*, *Itinerant nature of magnetism in iron pnictides: A first-principles study*, Phys. Rev. B **81**, 094505 (2010). [doi:10.1103/PhysRevB.81.094505](https://doi.org/10.1103/PhysRevB.81.094505)
- [141] C. Hess *et al.*, *The intrinsic electronic phase diagram of iron-oxypnictide superconductors*, EPL **87**, 17005 (2009). [doi:10.1209/0295-5075/87/17005](https://doi.org/10.1209/0295-5075/87/17005)
- [142] S. Iimura *et al.*, *Two-dome structure in electron-doped iron arsenide superconductors*, Nature Communications **3**, 943 (2012). [doi:10.1038/ncomms1913](https://doi.org/10.1038/ncomms1913)
- [143] S. Matsuishi *et al.*, *Structural analysis and superconductivity of CeFeAsO*, Physical Review B **85**, 014514 (2012). [doi:10.1103/PhysRevB.85.014514](https://doi.org/10.1103/PhysRevB.85.014514)
- [144] K. Miyazawa *et al.*, *Possible hydrogen doping and enhancement of  $T_c$  in a LaFeAsO-based superconductor*, Applied Physics Letters **96**, 072514 (2010). [doi:doi:10.1063/1.3319508](https://doi.org/10.1063/1.3319508)
- [145] T. Hanna *et al.*, *Hydrogen in layered iron arsenides: Indirect electron doping to induce superconductivity*, Physical Review B **84**, 024521 (2011). [doi:10.1103/PhysRevB.84.024521](https://doi.org/10.1103/PhysRevB.84.024521)
- [146] J. M. Schoen, *Augmented-Plane-Wave Virtual-Crystal Approximation*, Phys. Rev. **184**, 858 (1969). [doi:10.1103/PhysRev.184.858](https://doi.org/10.1103/PhysRev.184.858)
- [147] J. P. Perdew *et al.*, *Generalized Gradient Approximation Made Simple*, Phys. Rev. Lett. **77**, 3865 (1996). [doi:10.1103/PhysRevLett.77.3865](https://doi.org/10.1103/PhysRevLett.77.3865)
- [148] Y. Yamakawa *et al.*, *Phase diagram and superconducting states in LaFeAsO<sub>1-x</sub>H<sub>x</sub> based on the multiorbital extended Hubbard model*, Phys. Rev. B **88**, 041106 (2013). [doi:10.1103/PhysRevB.88.041106](https://doi.org/10.1103/PhysRevB.88.041106)
- [149] D. J. Singh, *Electronic structure and doping in BaFe<sub>2</sub>As<sub>2</sub> and LiFeAs: Density functional calculations*, Physical Review B **78**, 094511 (2008). [doi:10.1103/PhysRevB.78.094511](https://doi.org/10.1103/PhysRevB.78.094511)

- [150] N. Fujiwara *et al.*, *Detection of Antiferromagnetic Ordering in Heavily Doped LaFeAsO<sub>1-x</sub>H<sub>x</sub> Pnictide Superconductors Using Nuclear-Magnetic-Resonance Techniques*, Phys. Rev. Lett. **111**, 097002 (2013). doi:10.1103/PhysRevLett.111.097002
- [151] K. Suzuki *et al.*, *Model of the Electronic Structure of Electron-Doped Iron-Based Superconductors: Evidence for Enhanced Spin Fluctuations by Diagonal Electron Hopping*, Phys. Rev. Lett. **113**, 027002 (2014). doi:10.1103/PhysRevLett.113.027002
- [152] J. Zhao *et al.*, *Structural and magnetic phase diagram of CeFeAsO<sub>1-x</sub>F<sub>x</sub> and its relation to high-temperature superconductivity*, Nature Materials **7**, 953 (2008). doi:10.1038/nmat2315
- [153] A. J. Drew *et al.*, *Coexistence of static magnetism and superconductivity in SmFeAsO<sub>1-x</sub>F<sub>x</sub> as revealed by muon spin rotation*, Nature Materials **8**, 310 (2009). doi:10.1038/nmat2396
- [154] J. Zhao *et al.*, *Spin and lattice structures of single-crystalline SrFe<sub>2</sub>As<sub>2</sub>*, Physical Review B **78**, 140504 (2008). doi:10.1103/PhysRevB.78.140504
- [155] T. Goko *et al.*, *Superconducting state coexisting with a phase-separated static magnetic order in (Ba,K)Fe<sub>2</sub>As<sub>2</sub>, (Sr,Na)Fe<sub>2</sub>As<sub>2</sub>, and CaFe<sub>2</sub>As<sub>2</sub>*, Physical Review B **80**, 024508 (2009). doi:10.1103/PhysRevB.80.024508
- [156] J. H. Tapp *et al.*, *LiFeAs: An intrinsic FeAs-based superconductor with T<sub>c</sub>=18 K*, Physical Review B **78**, 060505 (2008). doi:10.1103/PhysRevB.78.060505
- [157] C. Chu *et al.*, *The synthesis and characterization of LiFeAs and NaFeAs*, Physica C: Superconductivity **469**, 326 (2009). doi:10.1016/j.physc.2009.03.016
- [158] F.-C. Hsu *et al.*, *Superconductivity in the PbO-type structure -FeSe*, PNAS **105**, 14262 (2008). doi:10.1073/pnas.0807325105
- [159] K.-W. Yeh *et al.*, *Tellurium substitution effect on superconductivity of the -phase iron selenide*, EPL (Europhysics Letters) **84**, 37002 (2008). doi:10.1209/0295-5075/84/37002
- [160] T. M. McQueen *et al.*, *Extreme sensitivity of superconductivity to stoichiometry in Fe<sub>1+δ</sub>Se*, Physical Review B **79**, 014522 (2009). doi:10.1103/PhysRevB.79.014522
- [161] S. Margadonna *et al.*, *Pressure evolution of the low-temperature crystal structure and bonding of the superconductor FeSe*, Physical Review B **80**, 064506 (2009). doi:10.1103/PhysRevB.80.064506
- [162] T. Miyake *et al.*, *Comparison of Ab initio Low-Energy Models for LaFePO, LaFeAsO, BaFe<sub>2</sub>As<sub>2</sub>, LiFeAs, FeSe, and FeTe: Electron Correlation and Covalency*, Journal of the Physical Society of Japan **79**, 044705 (2010). doi:10.1143/JPSJ.79.044705

- [163] A. Liebsch and H. Ishida, *Correlation-induced spin freezing transition in FeSe: A dynamical mean field study*, Physical Review B **82**, 155106 (2010). doi:10.1103/PhysRevB.82.155106
- [164] Y. Mizuguchi *et al.*, *Substitution Effects on FeSe Superconductor*, Journal of the Physical Society of Japan **78**, 074712 (2009). doi:10.1143/JPSJ.78.074712
- [165] S. Medvedev *et al.*, *Electronic and magnetic phase diagram of FeSe*, Nature Materials **8**, 630 (2009). doi:10.1038/nmat2491
- [166] A. Ciechan *et al.*, *The Pressure Effects on Electronic Structure of Iron Chalcogenide Superconductors FeSe<sub>1-x</sub>Te<sub>x</sub>*, Acta Physica Polonica A **820** (2012).
- [167] M. Pan *et al.*, *Distorted magnetic orders and electronic structures for FeSe under pressure*, Physica C: Superconductivity **471**, 603 (2011). doi:10.1016/j.physc.2011.05.006
- [168] M. Bendele *et al.*, *Pressure Induced Static Magnetic Order in Superconducting FeSe<sub>1-x</sub>*, Physical Review Letters **104**, 087003 (2010). doi:10.1103/PhysRevLett.104.087003
- [169] H. Okabe *et al.*, *Pressure-induced high- $T_c$  superconducting phase in FeSe: Correlation between anion height and  $T_c$* , Physical Review B **81**, 205119 (2010). doi:10.1103/PhysRevB.81.205119
- [170] K. Miyoshi *et al.*, *Magnetic measurements of FeSe superconductor under high pressure*, Journal of Physics: Conference Series **200**, 012126 (2010). doi:10.1088/1742-6596/200/1/012126
- [171] W. Uhoja *et al.*, *Simultaneous measurement of pressure evolution of crystal structure and superconductivity in FeSe<sub>0.92</sub> using designer diamonds*, EPL (Europhysics Letters) **99**, 26002 (2012). doi:10.1209/0295-5075/99/26002
- [172] P. Monthoux and G. G. Lonzarich, *Magnetically mediated superconductivity in quasi-two and three dimensions*, Physical Review B **63**, 054529 (2001). doi:10.1103/PhysRevB.63.054529
- [173] T. r. Moriya and K. Ueda, *Antiferromagnetic spin fluctuation and superconductivity*, Reports on Progress in Physics **66**, 1299 (2003). doi:10.1088/0034-4885/66/8/202
- [174] V. Ksenofontov *et al.*, *Density of phonon states in superconducting FeSe as a function of temperature and pressure*, Physical Review B **81**, 184510 (2010). doi:10.1103/PhysRevB.81.184510
- [175] C. W. Luo *et al.*, *Quasiparticle Dynamics and Phonon Softening in FeSe Superconductors*, Physical Review Letters **108**, 257006 (2012). doi:10.1103/PhysRevLett.108.257006

- [176] W. Wang *et al.*, *Electronic structure and phonon spectrum of binary iron-based superconductor FeSe in both nonmagnetic and striped antiferromagnetic phases*, *Physica C: Superconductivity* **472**, 29 (2012). doi:10.1016/j.physc.2011.10.004
- [177] W. Bao *et al.*, *Tunable  $(\delta\pi, \delta\pi)$ -Type Antiferromagnetic Order in  $\alpha$ -Fe(Te,Se) Superconductors*, *Physical Review Letters* **102**, 247001 (2009). doi:10.1103/PhysRevLett.102.247001
- [178] R. S. Kumar *et al.*, *Pressure induced high spin-low spin transition in FeSe superconductor studied by x-ray emission spectroscopy and ab initio calculations*, *Applied Physics Letters* **99**, 061913 (2011). doi:doi:10.1063/1.3621859
- [179] D. Liu *et al.*, *Electronic origin of high-temperature superconductivity in single-layer FeSe superconductor*, *Nature Communications* **3**, 931 (2012). doi:10.1038/ncomms1946
- [180] A. Jesche *et al.*, *Strong coupling between magnetic and structural order parameters in SrFe<sub>2</sub>As<sub>2</sub>*, *Physical Review B* **78**, 180504 (2008). doi:10.1103/PhysRevB.78.180504
- [181] J. P. Carlo *et al.*, *Static Magnetic Order and Superfluid Density of RFeAs(O,F) (R=La,Nd,Ce) and LaFePO Studied by Muon Spin Relaxation: Unusual Similarities with the Behavior of Cuprate Superconductors*, *Physical Review Letters* **102**, 087001 (2009). doi:10.1103/PhysRevLett.102.087001
- [182] E. Dagotto, *Colloquium: The unexpected properties of alkali metal iron selenide superconductors*, *Rev. Mod. Phys.* **85**, 849 (2013). doi:10.1103/RevModPhys.85.849
- [183] X. F. Lu *et al.*, *Superconductivity in LiFeO<sub>2</sub>Fe<sub>2</sub>Se<sub>2</sub> with anti-PbO-type spacer layers*, *Phys. Rev. B* **89**, 020507 (2014). doi:10.1103/PhysRevB.89.020507
- [184] M. Rotter *et al.*, *Superconductivity at 38K in the Iron Arsenide (Ba<sub>1-x</sub>K<sub>x</sub>)Fe<sub>2</sub>As<sub>2</sub>*, *Phys. Rev. Lett.* **101**, 107006 (2008). doi:10.1103/PhysRevLett.101.107006
- [185] M. Burrard-Lucas *et al.*, *Enhancement of the superconducting transition temperature of FeSe by intercalation of a molecular spacer layer*, *Nat Mater* **12**, 15 (2013). doi:10.1038/nmat3464
- [186] X. Zhu *et al.*, *Transition of stoichiometric Sr<sub>2</sub>VO<sub>3</sub>FeAs to a superconducting state at 37.2 K*, *Phys. Rev. B* **79**, 220512 (2009). doi:10.1103/PhysRevB.79.220512
- [187] D.-Y. Liu *et al.*, *Coexistence of localized and itinerant magnetism in newly discovered iron-selenide superconductor LiFeO<sub>2</sub>Fe<sub>2</sub>Se<sub>2</sub>*, arXiv:1402.4711 [cond-mat] (2014).
- [188] V. I. Anisimov *et al.*, *Band theory and Mott insulators: Hubbard U instead of Stoner I*, *Phys. Rev. B* **44**, 943 (1991). doi:10.1103/PhysRevB.44.943

- [189] M. Ferrero and O. Parcollet, TRIQS: a Toolbox for Research in Interacting Quantum Systems, <http://ipht.cea.fr/triqs>.
- [190] M. Aichhorn *et al.*, *Importance of electronic correlations for structural and magnetic properties of the iron pnictide superconductor LaFeAsO*, Phys. Rev. B **84**, 054529 (2011). [doi:10.1103/PhysRevB.84.054529](https://doi.org/10.1103/PhysRevB.84.054529)
- [191] P. Werner *et al.*, *Continuous-Time Solver for Quantum Impurity Models*, Phys. Rev. Lett. **97**, 076405 (2006). [doi:10.1103/PhysRevLett.97.076405](https://doi.org/10.1103/PhysRevLett.97.076405)
- [192] P. Werner and A. J. Millis, *Hybridization expansion impurity solver: General formulation and application to Kondo lattice and two-orbital models*, Phys. Rev. B **74**, 155107 (2006). [doi:10.1103/PhysRevB.74.155107](https://doi.org/10.1103/PhysRevB.74.155107)
- [193] L. Boehnke *et al.*, *Orthogonal polynomial representation of imaginary-time Greens functions*, Phys. Rev. B **84**, 075145 (2011). [doi:10.1103/PhysRevB.84.075145](https://doi.org/10.1103/PhysRevB.84.075145)
- [194] J. Ferber *et al.*, *Analysis of spin-density wave conductivity spectra of iron pnictides in the framework of density functional theory*, Phys. Rev. B **82**, 165102 (2010). [doi:10.1103/PhysRevB.82.165102](https://doi.org/10.1103/PhysRevB.82.165102)
- [195] N. Parragh *et al.*, *Conserved quantities of SU(2)-invariant interactions for correlated fermions and the advantages for quantum Monte Carlo simulations*, Phys. Rev. B **86**, 155158 (2012). [doi:10.1103/PhysRevB.86.155158](https://doi.org/10.1103/PhysRevB.86.155158)
- [196] N. Lanat *et al.*, *Orbital selectivity in Hund's metals: The iron chalcogenides*, Phys. Rev. B **87**, 045122 (2013). [doi:10.1103/PhysRevB.87.045122](https://doi.org/10.1103/PhysRevB.87.045122)
- [197] H.-Y. Cao *et al.*, *Antiferromagnetic ground state with pair-checkboard order in FeSe*, arXiv:1407.7145 [cond-mat] (2014).



# List of Publications and Preprints

Listed below are the publications and preprints written during the time of this Ph.D. project.

- **C. Heil** and W. von der Linden  
J. Phys. Condens. Matter **24**, 295601 (2012)  
Strong coupling expansion for the Bose-Hubbard and Jaynes-Cummings lattice models
- **C. Heil**, M. Aichhorn, H. Sormann, E. Schachinger, and W. von der Linden  
Preprint: arXiv:1210.2593 (2012)  
Static susceptibility and Fermi surface nesting in FeSe under pressure from first-principle calculations
- M. Nuss, **C. Heil**, M. Ganahl, M. Knap, H. G. Evertz, E. Arrigoni, and W. von der Linden  
Phys. Rev. B **86**, 245119, (2012)  
Steady-state spectra, current, and stability diagram of a quantum dot: A nonequilibrium variational cluster approach
- **C. Heil**, H. Sormann, L. Boeri, M. Aichhorn, and W. von der Linden  
Phys. Rev. B **90**, 115143 (2014)  
Accurate bare susceptibilities from full-potential *ab initio* calculations
- **C. Heil**, L. Boeri, H. Sormann, W. von der Linden, and M. Aichhorn  
Phys. Rev. B **90**, 165122 (2014)  
Effect of the iron valence in the two types of layers in  $\text{LiFeO}_2\text{Fe}_2\text{Se}_2$



# List of Abbreviations and Symbols

AFM	antiferromagnetic
BZ (1BZ)	(first) Brillouin zone
CMA	constant matrix element approximation
DFT	density functional theory
DMFT	dynamical mean field theory
DOS	density of states
FeSC	iron-based superconductor
FN	Fermi surface nesting
FP-LAPW	full-potential linearised augmented-planewave
high- $T_c$	high-temperature
INS	inelastic neutron scattering
IW	irreducible wedge
MVC	MacDonald, Vosko, Coleridge
RPA	random phase approximation
SDW	spin density wave
$T_c$	critical superconducting temperature
VCA	virtual crystal approximation
$\frac{d^2\sigma}{d\Omega d\omega}$	differential cross section
$\epsilon_F, E_F$	Fermi energy
$g_N$	gyromagnetic ratio of a neutron
$G (G^0)$	full interacting (non-interacting) Green's function
$G^H$	Hubbard local field factor
$\hbar$	reduced Planck's constant
$k_B$	Boltzmann's constant
$\mu_B$	Bohr magneton
$N(E_F)$	density of states at the Fermi energy
$r_0$	classical electron radius
$S(\mathbf{q}, \omega) (S_{\pm}(\mathbf{q}, \omega))$	dynamical (spin-flip) structure factor
$U^s (U^c)$	spin (charge) Hubbard interaction matrix
$V_{xc}$	exchange-correlation potential
$W$	effective electronic potential
$\chi_c (\chi_{\pm})$	fully interacting charge (spin) susceptibility
$\chi_c^{\text{ir}} (\chi_{\pm}^{\text{ir}})$	irreducible charge (spin) susceptibility function
$\chi_c^0 (\chi_{\pm}^0)$	non-interacting <i>bare</i> charge (spin) susceptibility



# List of Figures

1.1. Schematic phase diagram of a typical pnictide high- $T_c$ superconductor, reprinted with permission from Macmillan Publishers Ltd: Nature Communications 4, 1914, Blomberg <i>et al.</i> , copyright 2013. . . . .	2
2.1. Graphical representation of Eq. (2.10) to calculate the effective interaction potential $W$ . . . . .	14
2.2. Graphical representation of Eq. (2.14) to approximately calculate the effective interaction potential $W$ . . . . .	15
2.3. Single particle-hole polarization insertion $\chi_c^0$ , which is identical to $\chi_{\pm}^0$ . . . . .	16
2.4. Simplified picture of the Fermi surface of a two-band iron-based superconductor. . . . .	21
2.5. Graphical representation of the terms considered in an RPA formulation of $W$ . . . . .	23
2.6. Graphical representation of the <i>vertex correction</i> to $\chi^0$ . . . . .	24
2.7. Diagrammatic depiction of the terms considered in $U$ . . . . .	27
3.1. Details of the integration over $k$ -space for a homogeneous electron gas in a 2D square lattice according to (a): Eq. (3.1) and (b): Eq. (3.2). . . . .	31
3.2. Tetrahedron tessellation of the IW of a simple tetragonal lattice. . . . .	33
3.3. Panel (a): Tetrahedron tessellation of the IW. The red area indicates where the product of Heaviside functions equals unity while the green shading represents the area, where only $\Theta(\epsilon_F - \epsilon_{\mathbf{k}}^m)$ equals unity. Panel (b): First step of the tetrahedron reshaping to get fully occupied tetrahedrons where $\epsilon_{\mathbf{k}}^m < \epsilon_F$ . Panel (c): Second step of the tetrahedron reshaping to represent only the area where Eq. (3.3) is fulfilled. . . . .	35
3.4. Comparison of results obtained with the MVC code and our newly developed algorithm for 506 $k$ points in the IW. . . . .	36
3.5. Comparison of results obtained with the MVC code and our newly developed algorithm for 1015 $k$ points in the IW. . . . .	37
3.6. Comparison of results obtained in the CMA with our newly developed algorithm with 506 $k$ points in the IW and the MVC code for 506 and 1015 $k$ points. . . . .	38
3.7. Schematic drawing of a single tetrahedron with its corner coordinates $\mathbf{k}_i$ to illustrate the integration of Eq. (3.13). . . . .	40

4.1. (a) Tetrahedral mesh of the irreducible wedge of an fcc lattice. The other panels show the mesh after the first (b) and after the second (c) cut with the Fermi surface. . . . .	46
4.2. LDA bandstructure of Cr, decorated with partial characters. . . . .	48
4.3. FS of Cr in the $k_z=0$ plane. The different colors indicate different orbital character as described in Fig. 4.2. . . . .	49
4.4. Static bare susceptibility $\chi^0$ for Cr. CMA results are compared with the exact results. The upper panel (a) shows the converged results, while in the lower panel (b) only the contributions of the bands at the Fermi level have been included in the susceptibility. . . . .	51
4.5. LDA bandstructure for FeSe at ambient pressure with the bands labeled according to their dominant orbital character. . . . .	52
4.6. Static bare susceptibility in CMA $\chi_{\text{CMA}}^0$ for FeSe calculated by including different sets of bands, as shown in Fig. 4.5. . . . .	53
4.7. Static bare susceptibility $\chi^0$ for FeSe at ambient pressure calculated by including different sets of bands, as explained in Fig. 4.6. . . . .	54
4.8. Contributions of the band transitions to $\chi^0$ for FeSe at ambient pressure at the M point. . . . .	55
4.9. Imaginary part of the dynamic bare susceptibility $\chi^0$ for FeSe halfway between $\Gamma$ and M. The black line represents the result obtained with exact matrix elements and the red line depicts the CMA result. . . . .	56
4.10. Imaginary part of the dynamic bare susceptibility for FeSe at ambient pressure. The left panel (a) shows $\text{Im}\chi^0$ whereas the right panel (a) contains the results for $\text{Im}\chi_{\text{CMA}}^0$ . . . . .	57
5.1. Electronic phase diagram for $\text{LaFeAsO}_{1-x}\text{H}_x$ and $\text{LaFeAsO}_{1-x}\text{F}_x$ (Ref. [141]). Reprinted by permission from Macmillan Publishers Ltd: Nature Communications 3, Article number: 943, Iimura <i>et al.</i> , copyright 2012. . . . .	62
5.2. Crystal structure of LaFeAsO with the unit cell indicated by the solid black lines. The Fe plane is indicated by the red shading. . . . .	63
5.3. DFT bandstructure for LaFeAsO showing the Fe $d$ and As $p$ bands. . . . .	64
5.4. Fermi surface of LaFeAsO . . . . .	65
5.5. DOS of $\text{LaFeAsO}_{1-x}\text{F}_x$ near the Fermi energy at $\epsilon_F = 0$ as a function of doping. . . . .	67
5.6. DFT bandstructure for $\text{LaFeAsO}_{1-x}\text{F}_x$ as a function of doping. . . . .	68
5.7. Static bare susceptibility $\chi^0$ for LaFeAsO, $\text{LaFeAsO}_{0.9}\text{F}_{0.1}$ , $\text{LaFeAsO}_{0.8}\text{F}_{0.2}$ and $\text{LaFeAsO}_{0.7}\text{F}_{0.3}$ . . . . .	69
5.8. Top view of the Fermi surface at $k_z = 0$ of LaFeAsO (left) and $\text{LaFeAsO}_{0.8}\text{F}_{0.2}$ (right). Different colours indicate different bands. . . . .	70
5.9. $\chi^0(\mathbf{q})$ as a function of $\mathbf{q} = (q_x, q_y, 0)$ for undoped LaFeAsO (left) and $\text{LaFeAsO}_{0.8}\text{F}_{0.2}$ (right). . . . .	70
5.10. $\text{Im}\chi^0(\mathbf{q}, \omega)$ along high symmetry lines for undoped LaFeAsO (left) and $\text{LaFeAsO}_{0.8}\text{F}_{0.2}$ (middle) and $\text{LaFeAsO}_{0.7}\text{F}_{0.3}$ (right). . . . .	72

5.11. $\text{Im}\chi^0(\mathbf{q}, \omega)$ at X (upper panel) and M (lower panel) for undoped LaFeAsO and Land LaFeAsO <sub>0.7</sub> F <sub>0.3</sub> . . . . .	73
6.1. Static susceptibility $\chi^0$ in the $(q_x, q_y, 0)$ -plane of FeSe at a hydrostatic pressure of 2.8 GPa. . . . .	78
6.2. Static susceptibility $\chi^0$ in the $(q_x, 0, 0)$ direction of FeSe for different hydrostatic pressures. . . . .	78
6.3. Static susceptibility $\chi^0$ in the $(q_x, q_y, 0)$ -plane for FeSe at a non-hydrostatic pressure of 4 GPa. . . . .	79
6.4. Static susceptibility $\chi^0$ in the $(q_x, q_y, 0)$ -plane for FeSe at a non-hydrostatic pressure of 12.9 GPa. . . . .	80
6.5. Static susceptibility $\chi^0$ in the $(q_x, 0, 0)$ direction for FeSe for different non-hydrostatic pressures. . . . .	81
6.6. Fermi surface $k_z = 0$ cut for FeSe at a non-hydrostatic pressure of 4 GPa. . . . .	82
6.7. Fermi surface $k_z = 0$ cut for FeSe at a non-hydrostatic pressure of 12.9 GPa. . . . .	82
7.1. Nonmagnetic unit cell of LiFeO <sub>2</sub> Fe <sub>2</sub> Se <sub>2</sub> . . . . .	87
7.2. Left: DFT band structure of nonmagnetic LiFeO <sub>2</sub> Fe <sub>2</sub> Se <sub>2</sub> , isolated LiFeO <sub>2</sub> , and isolated FeSe. Right: (p)DOS of nonmagnetic LiFeO <sub>2</sub> Fe <sub>2</sub> Se <sub>2</sub> . . . . .	88
7.3. Left: Zoom of Fig. 7.2 with the bands of LiFeO <sub>2</sub> Fe <sub>2</sub> Se <sub>2</sub> in solid black. Right: Band structure of bulk FeSe calculated for the experimental crystal structure at ambient pressure from Ref. [161]. . . . .	89
7.4. Top view of the Fermi surface at $k_z = 0$ (left) and $k_z = \pi/c$ (right) of non-magnetic LiFeO <sub>2</sub> Fe <sub>2</sub> Se <sub>2</sub> . . . . .	90
7.5. Static bare susceptibility $\chi^0$ for isolated FeSe, isolated LiFeO <sub>2</sub> , and the full LiFeO <sub>2</sub> Fe <sub>2</sub> Se <sub>2</sub> compound. . . . .	91
7.6. Top view of the Fe lattices in LiFeO <sub>2</sub> Fe <sub>2</sub> Se <sub>2</sub> for the three most preferable magnetic configurations in terms of energy. . . . .	92
7.7. (a) (p)DOS of non-magnetic LiFeO <sub>2</sub> Fe <sub>2</sub> Se <sub>2</sub> , (b) (p)DOS of cb-ss LiFeO <sub>2</sub> Fe <sub>2</sub> Se <sub>2</sub> , and (c): (p)DOS of cb-ss LiFeO <sub>2</sub> Fe <sub>2</sub> Se <sub>2</sub> and $U = 2.7$ eV. . . . .	94
7.8. Magnetic moment of Fe in ss isolated FeSe, cb isolated LiFeO <sub>2</sub> and of Fe <sub>Li</sub> and Fe <sub>Se</sub> in cb-ss LiFeO <sub>2</sub> Fe <sub>2</sub> Se <sub>2</sub> . . . . .	95
7.9. Left: DFT+DMFT spectral function of paramagnetic LiFeO <sub>2</sub> Fe <sub>2</sub> Se <sub>2</sub> for $U = 4$ eV and $J = 0.9$ eV. Right: DFT+DMFT DOS of paramagnetic LiFeO <sub>2</sub> Fe <sub>2</sub> Se <sub>2</sub> for the same $U$ and $J$ parameters. . . . .	96
7.10. DFT+DMFT spectral function of paramagnetic LiFeO <sub>2</sub> Fe <sub>2</sub> Se <sub>2</sub> for $U = 4$ eV and $J = 0.9$ eV with the DFT band structure overlaid. . . . .	97
7.11. Contributions of Fe <sub>Se</sub> to the spectral function of paramagnetic LiFeO <sub>2</sub> Fe <sub>2</sub> Se <sub>2</sub> for $U = 4$ eV and $J = 0.9$ eV separated into orbital contributions. Top left: Fe <sub>Se</sub> $3d_{z^2}$ orbital, top right: Fe <sub>Se</sub> $3d_{x^2+y^2}$ , bottom left: Fe <sub>Se</sub> $3d_{xy}$ , bottom right: Fe <sub>Se</sub> $3d_{xz+yz}$ . . . . .	98
A.1. Schematic depiction of the corner coordinates $\mathbf{k}_i$ and the vectors $\mathbf{v}_i$ spanning the tetrahedron over which we have to integrate. . . . .	106



# List of Tables

5.1. Experimentally determined As positions $z_{As}$ for various dopings (see Ref. [142]). The dopings not coinciding with the exact experimental values were calculated using a linear fit. Additionally, the Fermi energies $\epsilon_F$ in eV and the DOS at $\epsilon_F$ are given. . . . .	66
7.1. Energies (with respect to the non-magnetic configuration) and magnetic moments of isolated $\text{LiFeO}_2$ $m(\text{Fe}_{\text{Li}})$ and isolated $\text{FeSe}$ $m(\text{Fe}_{\text{Se}})$ for ferromagnetic (fm), checker-board (cb), single stripe (ss), and double stripe (ds) magnetic configurations. . . . .	92
7.2. Energies (with respect to the nonmagnetic configuration) and magnetic moments of $\text{LiFeO}_2\text{Fe}_2\text{Se}_2$ in different magnetic configurations (compare with Fig. 7.6). . . . .	93